Plasma Ion Dynamics in Large-Amplitude Drift Waves: Stochasticity, Collisions, Orbit Loss, and Recycling

Thesis by

Steven Jay Sanders

In Partial Fulfillment of the Requirements
for the Degree of
Doctor of Philosophy

California Institute of Technology
Pasadena, California

1998
(Submitted July 24, 1997)

Acknowledgements

I wish to thank my advisor, Professor Paul Bellan, for his support and careful guidance during this thesis work. I learned a great deal of plasma physics from him, and benefitted from his friendship. I would also like to thank Professor Raul Stern of the University of Colorado. Dr. Stern taught me the craft of laser-induced fluorescence and shared with me his valuable laboratory experience and his wry sense of humor. I am truly fortunate to have worked with these two excellent physicists. Sincere thanks go to Mr. Frank Cosso for his invaluable assistance with the (ornery) experimental apparatus. I wish also to thank my friend and coworker Jimmy Yee for proofreading this thesis and for being ever-willing to discuss plasma physics. I thank my family for their constant encouragement during the difficult moments of graduate school. And I thank my lovely wife Illiana for being so very understanding of many long nights spent in the laboratory. We finally made it, darlin'! This work was supported by NSF Grant No. PHY-9413046.

Abstract

The dynamics of plasma ions in the presence of large-amplitude electrostatic waves are investigated experimentally. The work was conducted in Caltech's Encore research tokamak. The toroidal plasma current excites coherent, poloidally propagating drift waves which stochastically heat ions in the poloidal plane. Ion distribution functions $f(\mathbf{x}, \mathbf{v}, t)$ are probed via Laser-Induced Fluorescence along three orthogonal velocity directions. Wave phase resolution is provided by the narrow laser pulse width and by a novel data-acquisition system which ensures synchronization between laser trigger and drift wave.

Time-resolved measurements show a multi-step heating process during each wave period: (i) The wave electric field excites stochastic ion orbits in the poloidal ($\perp$) plane, resulting in $\perp$ heating. (ii) ion-ion collisions impart energy to the toroidal ($\|$) direction, raising $T_\|$ to relax the $\perp$-$\|$ temperature anisotropy. (iii) Hot ions with large gyroradius escape confinement, reaching the chamber wall and cooling the distribution. (iv) Cold ions from the plasma edge are convected back into the plasma (recycled), significantly replenishing the density depleted by orbit losses.

The ion-ion collision period $\tau(t) \sim T(t)^{3/2}/n(t)$ is highly time-dependent due to intense ($\approx$50%) fluctuations in both n and T. The anisotropic temperature relaxation rate is found to be consistent with Fokker-Planck theory when the time-dependence of the collision period is properly taken into account. Thus, classical Fokker-Planck correctly describes the evolution of $f(v_\|)$, despite the intrinsic single-particle stochasticity in the $\perp$ direction.

Evidence for ion recycling is given by observations of significantly non-Maxwellian (NM) ion velocity distributions near the plasma edge. These appear periodically, synchronous with the drift wave phase at which, simultaneously, ion fluid flow from the wall toward the plasma center peaks, ion density is a local minimum, and ion temperature is high. The appearance of NM features at this phase is consistent with

the intantaneously low ion collision rate which allows non-equilibrium features to be long-lived. The observed NM distributions are bimodal and indicate the presence of a group of cold ions (0.4 eV) superimposed on a hot background plasma (8 eV) of roughly equal density.

Contents

List of Figures

List of Tables

Chapter 1 Introduction

This thesis describes experimental studies of plasma ion dynamics in the presence of large-amplitude electrostatic plasma waves. The work was conducted in Caltech's Encore tokamak, which has strong drift wave fluctuations naturally excited by the toroidal plasma current. Ions in these plasmas are rapidly heated by nonlinear interaction with the drift waves, resulting in stochastic ion orbits. In recent years, a number of authors have studied stochastic plasma heating by electrostatic waves [1], but all of those experiments involved 'ideal' plasmas in some sense, i.e., collisionless, well-confined plasmas. In contrast, Encore plasma dynamics are strongly influenced by not only ion stochasticity, but also collisions, orbit loss, and particle recycling. The present work is an investigation of plasma dynamics when many of these processes are simultaneously important.

Chapter 2 introduces the plasma device used for this work – the Encore tokamak – and the experimental parameters prevailing in Encore plasmas. Encore produces inductively-coupled plasmas at a repetition rate of 15 Hz, each discharge having a duration of about 1 millisecond. Electrons are heated rapidly to 5-15 eV by the Ohmic heating transformer. The plasma density is typically $\sim 10^{12}$ cm^{-3} singly ionized Argon. Ion temperature is 1-10 eV. The magnetic field for these experiments was 300 Gauss, giving good electron confinement. The issue of ion confinement is more complicated and will be discussed in Chapter 4.

An important feature of Encore plasmas is that the toroidal plasma current I_p excites a drift-Alfvén wave instability [2]. The drift waves propagate poloidally (i.e., the short way around the torus cross-section), and have frequency about 1/2 the ion cyclotron frequency. The wave amplitude is proportional to I_p, and very strong coherent waves are excited for $I_p \approx 1-1.5$ kA. Previous work in Encore by McChesney *et al.* showed that ion orbits become stochastic when the drift wave amplitude exceeds a well-defined threshold and that this stochasticity leads to anomalously fast ion

heating [3]. Chapter 2.2 gives a brief outline of fundamental drift wave properties and displays measurements of several plasma parameters fluctuating in the drift wave. The chapter also discusses at length the nonlinear mechanism by which these waves cause ion dynamical stochasticity.

The principal diagnostic tool for this thesis work was laser-induced fluorescence (LIF) [4]. The LIF method uses a narrow-band, tunable laser to scan the absorption spectrum of plasma ions. For the Ar II plasmas in Encore, the ion absorption spectrum is primarily Doppler broadened and is therefore a direct map of the ion velocity distribution. Thus, time- and space-resolved LIF measurements give the complete ion kinetic distribution function $f(\mathbf{x}, \mathbf{v}, t)$. The Encore LIF system consisted of YAG-pumped dye lasers with trigger timing variable in 50-nsec increments, so that f could be sampled throughout the entire drift waveform with high resolution of the drift wave phase. The two dye laser beams were typically split and directed across the plasma at right angles to each other to measure simultaneously two orthogonal components of $f(\mathbf{v})$. Chapter 2.3 discusses the fundamentals of LIF. This section also presents measured induced-fluorescence signal levels for four LIF schemes in Ar II [5]. At least two of these schemes have not previously been employed, to the author's knowledge. One scheme, based on a 664-nm pump laser and a 435-nm observation line, offered a significant signal increase over the standard scheme (pump 611 nm, observe 461 nm) popular among plasma experimentalists. Finally, the chapter describes the experimental layout and control system used to interrogate ion distribution functions in the presence of drift waves.

The LIF system used with Encore required data from several thousand discharges to determine the velocity dependence of a single distribution $f(\mathbf{x}, \mathbf{v}, t)$ at fixed $\mathbf{x}$ and t. This is because the dye laser wavelength had to be scanned to sample the entire ion Doppler spectrum and because the fluorescence signal at each wavelength was averaged over 30 shots to increase the signal-to-noise ratio. This need for ensemble averaging was facilitated by Encore's high repetition rate, but it also placed stringent demands on the reproducibility of the drift waveform from discharge to discharge. Any shot-to-shot jitter in the drift wave phase, for example, would mean that an

LIF measurement was an average over $f(\mathbf{v},t)$ sampled at a variety of wave phases, obscuring any phase-dependent physics. Unfortunately, after a great deal of effort was devoted to optimizing Encore operation, the drift wave phase jitter was still roughly $\pm 90°$.

To ameliorate this phase jitter problem, a novel data acquisition system was developed to ensure synchronization between the wave phase and measurements made by LIF or any other Encore diagnostic. This wave-selective data acquisition system (WDAS) monitored the drift waveform in real time and compared it to a predefined 'nominal' waveform. If a discharge waveform was found to be quantitatively similar to the nominal waveform, then LIF data from that shot were used to deduce $f(\mathbf{v},t)$. Conversely, shots whose waveforms differed excessively from the nominal waveform were rejected and LIF data from those shots ignored. Chapter 3 presents the details of the WDAS and illustrates its efficacy in reducing the phase jitter problem in Encore plasmas. The WDAS essentially solved the wave jitter problem, and enabled measurements with an order of magnitude better wave phase resolution than previously possible. The basic principles of this system should prove useful in other repetitively pulsed experiments.

Chapter 4 presents the primary experimental results of this thesis work. By means of LIF and using several orthogonally-directed beams, the ion distribution function $f(\mathbf{x},\mathbf{v},t)$ was measured along all three velocity dimensions and with high wave phase and spatial resolution. The measurements were performed when the drift wave amplitude was far above the threshold for stochastic ion heating. These data allowed detailed examination of the evolution of ion temperature both along ($\parallel$) and perpendicular to ($\perp$) the toroidal magnetic field when ion dynamics were stochastic. It was found that ion heating in the perpendicular plane was extremely rapid and isotropic, as expected for a stochastic heating mechanism. The parallel heating was found to be about a factor 3 slower than the perpendicular heating and to follow the latter after a finite time lag suggestive of a collision period. By comparison of the measured ion temperatures and densities to a Fokker-Planck model, it was shown that the parallel heating rate was explained by collisional energy transfer from the

perpendicular to parallel degrees of ion freedom. Although the collisional relaxation of temperature anisotropies has previously been investigated in quiescent non-neutral plasmas [6], the present work represents the first detailed relaxation measurements in a neutral plasma and the first in a plasma having significant wave activity. It was discovered that in Encore the ion-ion collision rate fluctuated strongly with the drift wave phase, a phenomenon which, to our knowledge, has not been observed before. These oscillations of collision rate result from ion density and temperature fluctuations induced by the drift wave and therefore challenge the commonly-used notion of wave propagation in an ideal, collisionless plasma. Finally, the agreement between the measured parallel heating rate and the Fokker-Planck theory indicate that the latter is applicable even when ion dynamics are stochastic. The theory has not previously been applied to plasmas undergoing strong external heating.

Chapter 4 also presents observations of ion cooling: the ions are observed to heat and cool cyclically, in alternate drift wave phases. This cooling is probably the result of ion orbit loss to the cold tokamak wall. When ions heat due to stochasticity, they rapidly attain energies beyond the confinement capacity of the modest magnetic field of Encore. The hot ions reach the chamber wall, where they may recombine, adsorb, or reflect back into the plasma, losing the bulk of their kinetic energies in the wall interaction [7]. The stochastic heating and subsequent cooling due to orbit loss may together comprise a kind of self-consistent limit cycle for the ion temperature oscillations. Chapter 4.4 outlines quantitative predictions for cooling due to orbit loss. However, it is shown that elementary consideration of ion trajectories and classical orbit losses cannot describe the observed ion cooling rate. This discrepancy, no doubt, results from lack of an adequate analytical description of stochastic ion orbits in Encore. The chapter concludes by arguing that these newly observed phenomena, collisionality oscillations and periodic cooling via orbit loss, should be important in other strongly fluctuating plasmas.

Chapter 5 presents observations of convective ion "recycling" from the Encore wall. The term recycling refers in plasma physics to the return of particles to the plasma bulk after interacting with the confining chamber wall. Particle recycling

cools and otherwise perturbs the bulk plasma, and these perturbations turn out to carry profound implications in, for example, fusion tokamak plasmas [8]. Although investigation of recycling was not a primary goal of this thesis work, it was eventually recognized that recycling may play a significant role in the drift wave heating and cooling cycle. Evidence is presented that recycled ions are periodically convected inward by the Encore drift waves: highly non-Maxwellian (NM) distribution functions are observed near the chamber wall during the wave phase at which, simultaneously, ion fluid flow from the wall toward the plasma center peaks, ion density is a local minimum, and ion temperature is high. The instantaneously low density and high temperature produce a long ion-ion collision time ($\tau \sim T^{3/2}/n$), meaning that such non-equilibrium features can be long-lived at this wave phase. The observed NM distributions are bimodal and indicate the presence of a group of cold ions (0.4 eV) superimposed on a hot background plasma (8 eV). NM features are observed along all three ion velocity components and are highly localized near the plasma edge. These observations strongly suggest a recycling interpretation. It may be speculated that recycling is an important refuelling mechanism for the drift wave immediately after the cooling phase in which particles are lost to the chamber wall.

Chapter 6 presents experimental results obtained from optical tagging, a two-laser extension of the basic LIF technique [9]. Tagging allows direct observation of particle orbits by optically pumping ions into a long-lived quantum state. The pumping is followed by a search laser which probes for the presence of these tagged ions at selected positions in phase space. The tagging technique is discussed and data obtained through its use are employed to explain some previously puzzling observations about ion heating very early in the discharge. Tagging was also used to check the prediction by Bailey *et al.* that ions in stochastic motion should have very unusual distribution functions [10]. The theoretical basis for the prediction is sketched, and tagging measurements, which did not reveal the effects predicted by Bailey *et al.* are discussed.

Finally, Appendix A contains an elementary discussion of transition-line broadening mechanisms. This subject pertains to the interpretation of absorption spec-

tra obtained by LIF. The three most important broadening mechanisms in Encore, namely Doppler, power, and Zeeman broadening, are discussed.

Bibliography

[1] For example, F. Doveil, *Phys. Rev. Lett.*, **46**, 532 (1981); F. Skiff, F. Anderegg, and M.Q. Tran, *Phys. Rev. Lett.*, **58**, 1430 (1987); F. Skiff *et al.*, *Phys. Rev. Lett.*, **61**, 2034 (1988); A. Fasoli *et al., Phys. Rev. Lett.,* **70**, 303 (1993).

[2] E.D. Fredrickson and P.M. Bellan, "Investigation of finite beta modified drift wave in a tokamak plasma," *Phys. Fluids* **28**, 1866 (1985).

[3] J.M. McChesney, R.A. Stern, and P.M. Bellan, "Observations of fast stochastic ion heating by drift waves," *Phys. Rev. Lett.,* **59**, 1436 (1987).

[4] R.A. Stern and J.A. Johnson III, " Plasma ion diagnostics using resonant fluorescence," *Phys. Rev. Lett.*, **34**, 1548, (1975).

[5] J.M. McChesney, "A laser-induced fluorescence diagnostic for divertors," Final Report, DOE Grant No. DE-FG03-92ER54150.

[6] A.W. Hyatt, C. F. Driscoll, and J. H. Malmberg, "Measurement of anisotropic temperature relaxation rate in a pure electron plasma," *Phys. Rev. Lett.* **59**, 2975 (1987); B. R. Beck, J. Fajans, and J. H. Malmberg, "Measurement of collisional anisotropic temperature relaxation in a strongly magnetized pure electron plasma," *Phys. Rev. Lett.* **68**, 317 (1992).

[7] J.N. Brooks, "Analysis of noble gas recycling at a fusion plasma divertor," Phys. Plasmas **3**, 2286 (1996).

[8] P.C. Stangeby and G.M. McCracken, "Plasma boundary phenomena in tokamaks," *Nucl. Fusion* **30**, 1271 (1990).

[9] R.A. Stern, D.N. Hill, and N. Rynn, "Direct ion-transport measurement by optical tagging," *Phys. Lett. A* **93**, 127 (1983).

[10] A.D. Bailey III, P.M. Bellan, and R.A. Stern, "Poincaré maps define topography of Vlasov distribution functions consistent with stochastic dynamics," Phys. Plasmas **2**, 1, (1995).

Chapter 2 Encore Tokamak, Drift Waves, and Laser Induced Fluorescence

2.1 Apparatus

The experimental work for this thesis was performed in the Caltech Encore Tokamak. A diagram of the geometry is given in Fig. 2.1. Encore is a small device (minor radius $a = 12.7$ cm and major radius $r = 38$) with relatively low toroidal magnetic field ($B_\varphi \lesssim 1200$ G) and high repetition rate (15 Hz). Encore does not produce fusion-relevant plasmas, but is used rather to study basic plasma physics in toroidal geometry. Encore's high repetition rate and generous optical access make it well-suited for laser-induced fluorescence (LIF) measurements of ion kinetics. Argon was used as the working gas because there are many convenient LIF schemes available in Ar II.

The toroidal field for these experiments was $B_\varphi = 300$ G, giving ion and electron cyclotron frequencies of $\Omega_i/2\pi = 1.2 \times 10^4$ s^{-1} and $\Omega_e/2\pi = 5 \times 10^9$ s^{-1}. Other typical running parameters were plasma current $I_p = 1 - 1.5$ kA, density $n = 1 - 5 \times 10^{12}$ cm^{-3} fully ionized Ar II, and ion and electron temperatures $T_i = 1 - 10$ eV and $T_e = 5 - 15$ eV. The toroidal magnetic field was generated in steady state by a 50-kWatt DC power supply (Siliconel Model 805), and the Ohmic heating (OH) current was generated by a high-power shaker amplifier (MB model T666).

In addition to LIF, Langmuir probes were used extensively for this thesis work. The plasma was sufficiently cool to allow safe probe insertion without causing probe damage. Probes were available at an array of toroidal locations and could be positioned within a poloidal cross section by computer-controlled stepping motors. Measurement of the probe current-voltage characteristic allowed determination of n, T_e, the plasma potential ϕ_p, and the floating potential ϕ_f. Unmagnetized probe theory

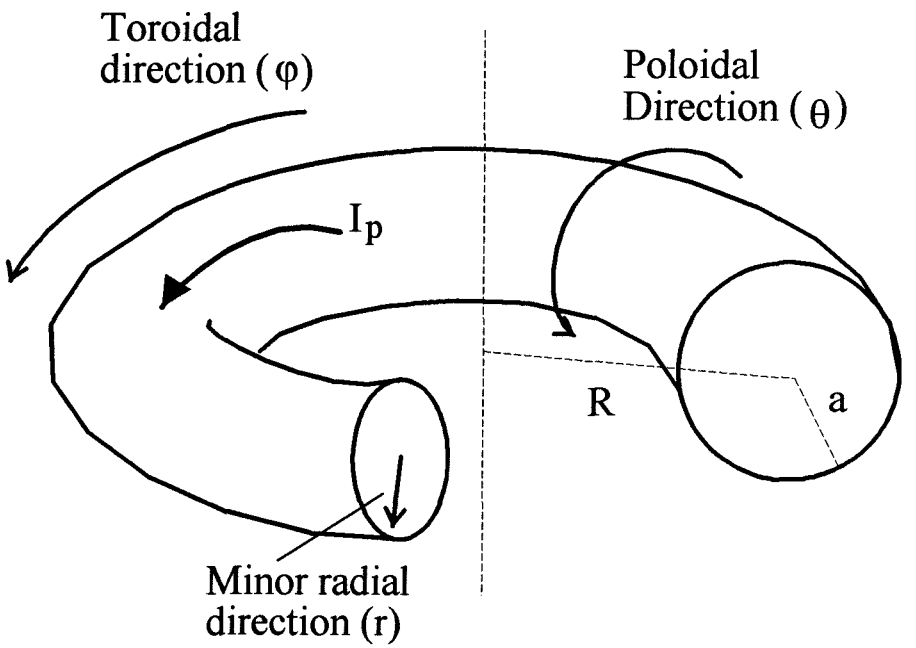

Figure 2.1: Sketch of Encore torus. The major radius $R = 38$ cm and the minor radius $a = 12.7$ cm. The toroidal, poloidal, and minor radial directions are as indicated.

[1] was used because $r_c \gg \lambda_D$ for both ions and electrons. Here r_c is the cyclotron radius and λ_D is the Debye shielding length.

Plasma parameters for a typical discharge are plotted in Fig. 2.2. Trace (a) shows the computer-generated voltage waveform amplified and applied across the primary windings of the OH transformer. The applied OH pulse induces a toroidal loop voltage, V_{loop}, across the gas, which acts as the single-turn secondary of the transformer. Trace (b) shows V_{loop} and trace (c) the resulting plasma current I_p for a typical shot. Trace (d) displays the ion saturation current collected by a Langmuir probe immersed in the plasma near the edge.

2.2 Drift Waves

2.2.1 Introduction

The fluctuations ($\omega/2\pi = 2.7 \times 10^4$ s^{-1}) evident in the saturation current of Fig. 2.2(d) result from the presence of large-amplitude drift-Alfvén waves, as shown by Fredrickson and Bellan [2]. All other macroscopic plasma parameters also oscillate coherently with the wave. For example, Fig. 2.3 shows T_e and ϕ_p in the presence of the drift wave; fluctuations in T_e and ϕ_p follow the density fluctuations by $\sim 90°$ and $\sim 180°$, respectively.

Drift waves are normal modes of inhomogeneous plasmas. Drift wave amplitude grows at the expense of free energy stored in plasma pressure and temperature gradients [?]. Since all terrestrial plasmas are finite in extent, drift waves are ubiquitous in laboratory plasma devices and have been dubbed "the universal instability." [3] Indeed, the model of Fredrickson and Bellan was later used to identify drift waves in many other small plasma devices, including the SHEILA Heliac at Australian National University [4] and the HIEI tandem mirror at Kyoto University [5].

The drift wave propagates nearly perpendicular to both ∇n and $\mathbf{B}$, i.e., $\mathbf{k} \sim \nabla n \times \mathbf{B}$. Thus the wave spatial structure has the form

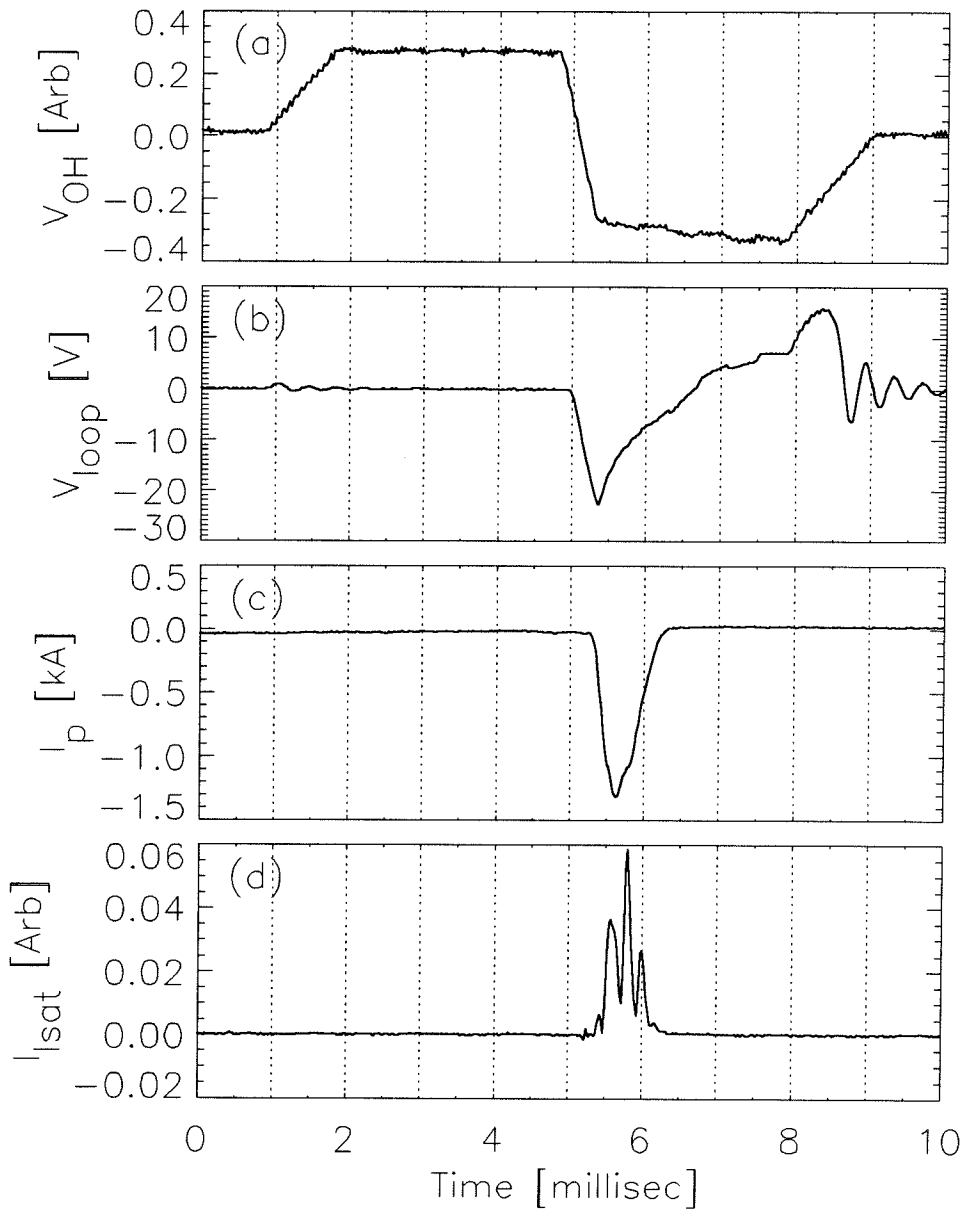

Figure 2.2: Typical shot parameters: (a) Waveform applied to OH transformer. (b) Toroidal loop voltage. (c) Plasma current, measured by Rogowski coil. (d) Ion saturation current to Langmuir probe.

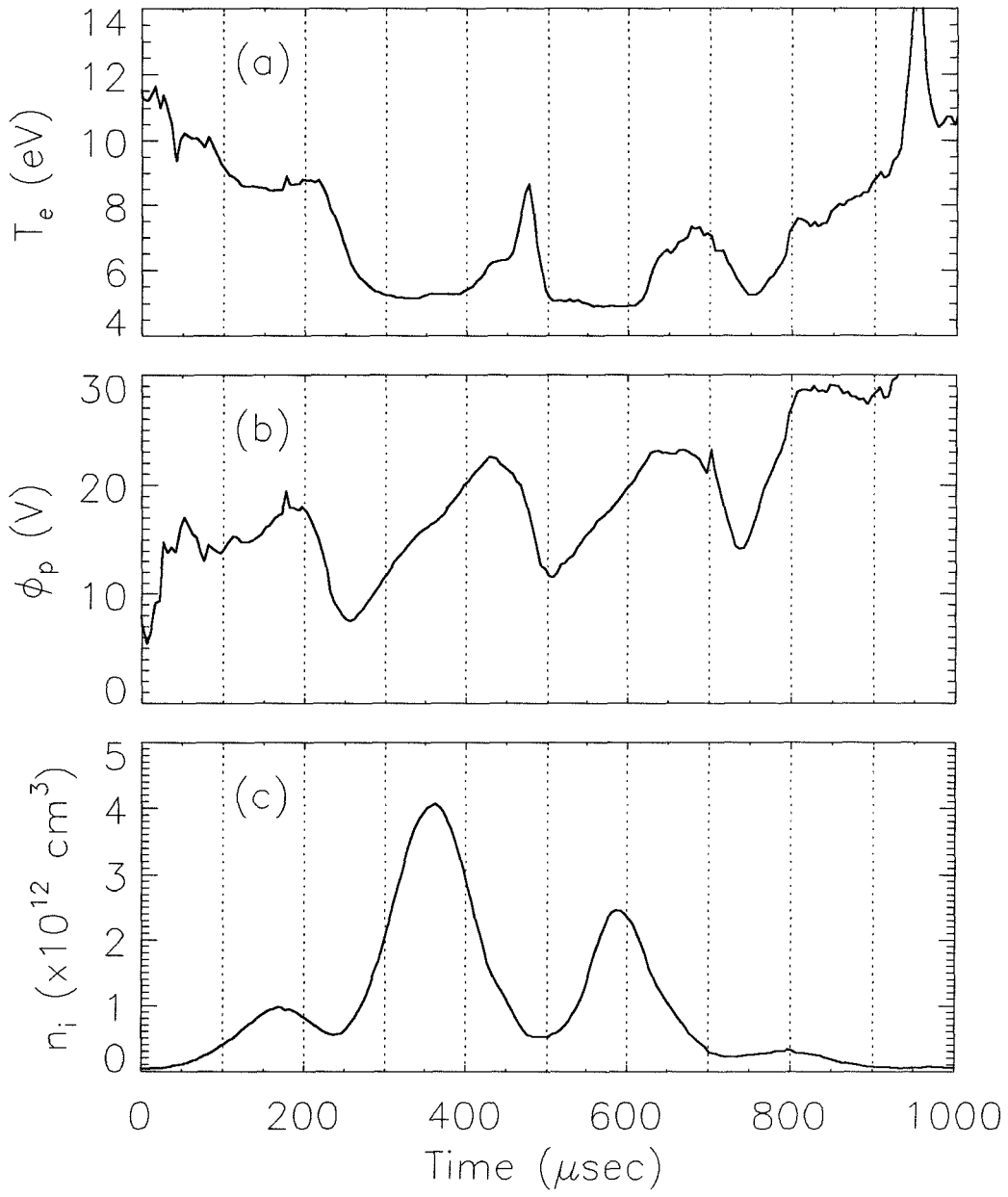

Figure 2.3: Measured evolution of (a) electron temperature, (b) plasma potential, and (c) ion density in the presence of large-amplitude drift waves. These parameters were measured by Langmuir probe 4 cm from the plasma edge.

$$\phi(r,\theta,z,t) = \tilde{\phi} f(r) e^{i(k_\theta r\theta + k_\varphi R\varphi - \omega t)},$$

where $k_\theta \gg k_\varphi$ and (r,θ,φ) are the minor radial, poloidal, and toroidal directions, respectively (c.f. Fig. 2.1). The toroidal mode number is 1 and the poloidal is 2, giving $k_\varphi = 1/R = 2.6$ m^{-1} and $k_\theta = 2/r_0 = 30$ m^{-1}, where r_0 is the radius of maximum wave amplitude. Figure 2.4 shows the wave density profile in the poloidal plane. The peaks of the $m = 2$ mode are clearly visible near 12 and 6 o'clock.

Derivations of the drift-Alfvén wave dispersion relation may be found in the literature [6], [2], and will not be repeated here. The real part of the wave frequency is given by

$$\omega_r = \frac{\omega_{e*}}{1+b}\left[1 - \left(\frac{\omega_{e*}}{k_\varphi v_A}\right)^2 \frac{b}{(1+b)^3}\right]. \tag{2.1}$$

Here $\omega_{e*} = k_\theta \kappa_B T_e (\partial n/\partial r)\,[m_e \Omega_e n]^{-1}$ is the electron diamagnetic drift frequency, $v_A = B_\varphi (m_i \mu_0 n)^{-1/2}$ is the Alfvén speed, $b \equiv k_\theta^2 \kappa_B T_e (m_i \Omega_i^2)^{-1}$, m_i and m_e are the ion and electron masses, κ_B is Boltzmann's constant, and μ_0 is the permeability of free space. The bracketed term in Eq. 2.1 is a correction due to the magnetic character of the wave. For Encore parameters, the magnetic correction is roughly 1%, and will be ignored for the rest of this thesis; the electric field will be assumed to be electrostatic, $\mathbf{E} = -\nabla\phi$.

The wave growth rate ω_i results from axial electron drift [7], Landau damping [8], and electron-ion collisions [2] and has the form

$$\omega_i = \frac{\omega_*^2}{k_\varphi v_{Te}} \frac{1}{(1+b)^3}\left[\frac{\pi^{1/2} k_\varphi u_{\varphi e}}{\omega_r} + \pi^{1/2} b + \frac{\nu_{ei} b}{k_\varphi v_{Te}}\right]. \tag{2.2}$$

Here $u_{\varphi e}$ is the electron toroidal drift velocity, ν_{ei} is the electron-ion collision rate, and $v_{Te} = (\kappa_B T_e/m_e)^{1/2}$ is the electron thermal velocity. The middle term represents the Landau damping contribution. In Encore, where $\nu_{ei} \lesssim 2 \times 10^6$ s^{-1} and $u_{\varphi e} \sim 10^5$ m/s, the relative size of these terms is roughly 1.0 : 0.15 : 0.08, so that the growth

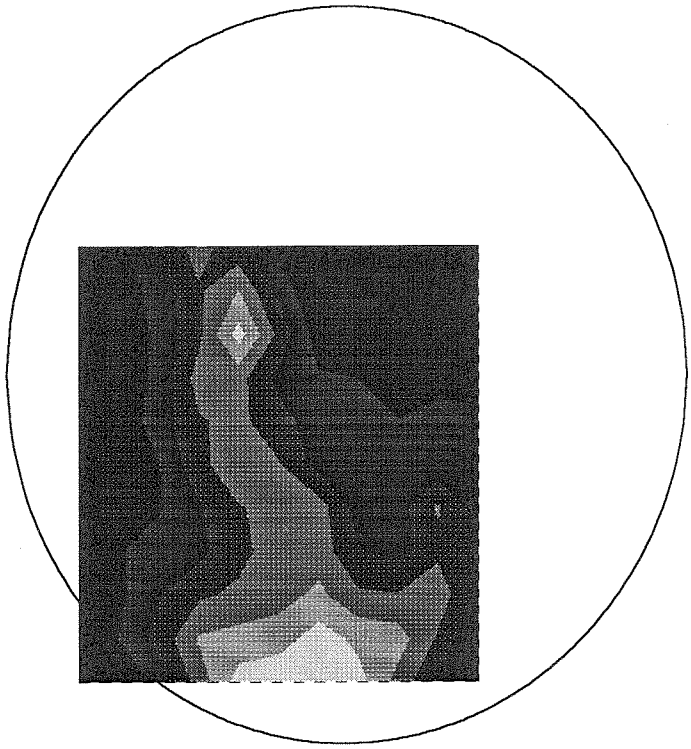

Figure 2.4: Contour plot of ion density in poloidal cross section, as measured by XY-scanning Langmuir probe. Peak level (white) is 4×10^{12} cm^{-3} and contour interval is 6×10^{11}. The toroidal axis is to the right and **B** points into the page. The wave rotates clockwise, in the electron diamagnetic drift direction.

rate is strongly determined by $u_{\varphi e}$. The electron drift is related to the plasma current through $u_{\varphi e} = I_p/nq$, so the wave amplitude $\tilde{\phi}$ can be controlled by varying the OH voltage which drives I_p. Large-amplitude, coherent waves can be excited. Ion dynamics in the presence of these waves is the subject of the next section.

2.2.2 Wave-Induced Stochasticity

McChesney, Stern, and Bellan used LIF to measure ion distribution functions in the presence of the drift waves [9]. They showed that for large $\tilde{\phi}$, Encore ions heat at a rate 40 times too fast to be explained by classical Ohmic heating. (Classical OH consists of rapid acceleration of electrons by the OH field, followed by collisional transfer of energy from electrons to ions.) They attributed the rapid heating to stochastic ion orbits induced by the wave electric field propagating normally to **B**. A brief outline of stochastic heating follows.

Consider a slab model of the microscopic ion motion in Encore drift waves. In rectangular coordinates, i.e., $(r,\theta) \rightarrow (x,y)$ and $\varphi \rightarrow z$, the magnetic and electric fields may be written $\mathbf{B} = B_0\hat{z}$ and $\mathbf{E} = -\nabla\phi$, with $\phi(x,y,z,t) = \phi_0 \cos(k_y y - \omega t)$. For Encore drift waves, the parallel wave number k_z is small compared to k_y ($k_z \approx k_y/10$) and may therefore be neglected. The ion equations of motion are

$$\begin{aligned} \dot{v}_x &= \Omega_i v_y \\ \dot{v}_y &= -\Omega_i v_x + \frac{q\tilde{\phi}}{m_i} k_y \sin(k_y y - \omega t). \end{aligned} \tag{2.3}$$

Integrating the top equation and combining with the bottom yields $\dot{v}_y = -\Omega_i^2(y - y_0 + v_{x0}/\Omega_i) + (q\tilde{\phi}k_y/m_i)\sin(k_y y - \omega t)$. The integration constants y_0 and v_{x0} may be eliminated by redefining the y and t origins, and can therefore be neglected. It is useful to rewrite this equation in dimensionless form, by normalizing times to the cyclotron period and distances to the wavelength. Defining $\tau \equiv \Omega_i t$ and $\xi \equiv k_y y$, we have

$$\frac{d^2\xi}{d\tau^2} = -\xi + \alpha \sin(\xi - \nu\tau), \tag{2.4}$$

where $\alpha \equiv q\phi_0 k_y^2/m\Omega_i^2$ and $\nu \equiv \omega/\Omega_i$. This equation describes a harmonic oscillator driven non-linearly by a wave with amplitude α. For $\alpha = 0$, ion trajectories reduce to simple cyclotron motion, i.e., $d^2\xi/d\tau^2 = -\xi$ for each degree of freedom. For $\alpha > 0$, the cyclotron orbits are perturbed, and the motion can become quite complicated. Karney and Bers studied this situation for $\nu \sim 30$ and demonstrated that ion trajectories become stochastic for large α [10]. Smith and Kaufman studied the case in which the wave propagates obliquely relative to **B** [11]. Chernikov *et al.* [12] have studied Eqs. 2.3 and similar systems in great detail. McChesney, Stern, and Bellan first analyzed the case of ions in drift waves.

Equation 2.4 cannot be solved analytically, but numerical solutions for the orbits may be obtained. Figure 2.5 shows representative phase trajectories, in un-normalized units, for a range of perturbation amplitudes α. The plots are Poincaré sections of the motion, i.e., two-dimensional cuts through the five-dimensional ion phase space (x, y, v_x, v_y, t): Each time an ion passes through some specified phase plane, say $v_x = 0$, the coordinates of the 'puncture' event are recorded. A Poincaré section is a scatter plot of coordinate pairs of such puncture events. For example, Fig. 2.5(a) is a scatter plot of v_y vs. t for punctures of the plane $v_x = 0$.

The Poincaré plots in Fig. 2.5 may be understood as follows. For $\alpha = 0$, cyclotron motion, the orbits would appear as straight vertical lines. For $\alpha = 0.2$ the orbits are only slightly perturbed, except near $v = 0$; this is because the magnetic force on a fast ion dominates over the electric force. At 'medium' α, i.e., $\alpha \approx 0.6$, the orbits are very strongly perturbed. Orbits near $v = 0$ no longer resemble cyclotron motion, but are evidently still integrable. Finally, for $\alpha \gtrsim 0.7$, the phase plots change dramatically. The orbits of ions with initial conditions near $v = 0$ are no longer confined to smooth, well-defined curves. Rather, ions rapidly traverse large regions of phase space, and two ions with nearby initial conditions can have exponentially diverging trajectories; the orbits are chaotic, or *stochastic*.

As is common in chaotic systems, stochastic orbits appear abruptly when α surpasses a 'stochastic threshold.' Numerical simulations show that Eq. 2.4 yields stochastic orbits above $\alpha_{threshold} \approx 0.7$. Note that orbits at large v are still integrable, but the stochastic region widens with increasing α. One other important point, evident in Figs. 2.5(c) and (f), is that the stochasticity acts in *both the* v_x *and* v_y *planes*, although the electric field is polarized along $\hat{y}$.

Stochastic *heating* results from the fact that ions which originate near $v = 0$ have access to phase regions of high velocity: note that the stochastic region in Figs. 2.5(c) and (e) extends to at least $v \gtrsim 2\Omega_i/k_y$. Ions acquire energy from the wave electric field, and the energy is randomized by the stochasticity, even in the absence of collisions. This randomization is physically due to ions being (a) temporarily trapped in a potential well of the drift wave and (b) subsequently un-trapped by the pull of the magnetic field [7]. In escaping a wave trough, an ion can cross many wave phases and quickly 'forget its past.' The onset of stochasticity also correlates with a breakdown in the guiding center drift approximations for ion motion.

McChesney, Stern, and Bellan gave the following experimental evidence for drift-wave stochastic heating:

(1) Measurements of T_i showed the expected rapid increase in peak ion temperatures when the wave amplitude was raised above the stochastic threshold, $\alpha \sim 0.6 - 0.8$.

(2) Ion heating was shown to be strongest near the plasma edge, at the location of maximum drift wave amplitude.

(3) High ion temperatures were shown to correlate well with enhanced Landau damping of ion acoustic waves at large α. This observation showed that the measured ion energy spread was truly thermalized, and not simply misinterpreted fluid motion [7].

(4) Numerical simulations of ion motion in measured wave fields showed heating rates in good agreement with experiment.

Bailey, Stern, and Bellan used a planar laser-induced fluorescence (PLIF) imaging system to measure the ion flow pattern when ion dynamics were stochastic [13].

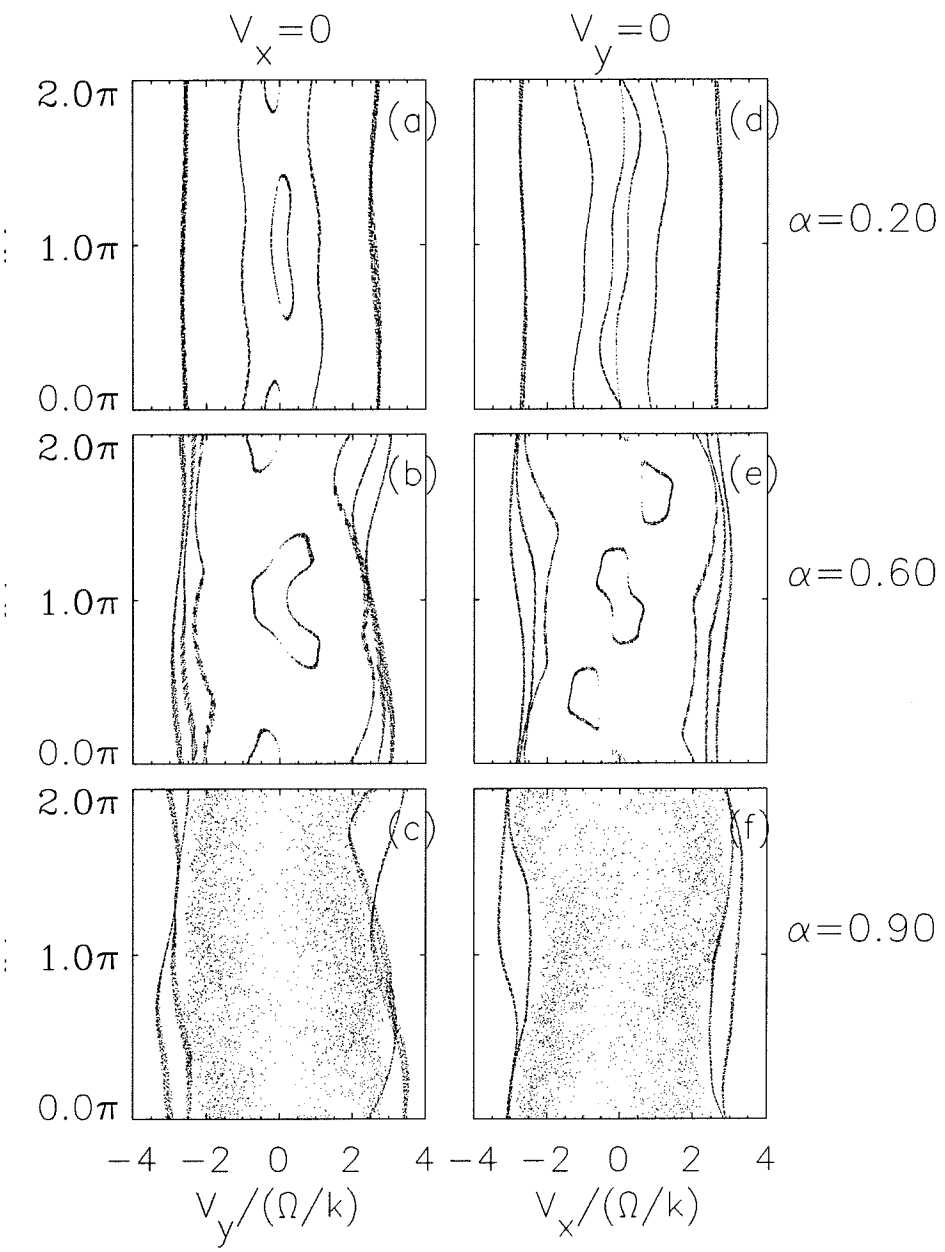

Figure 2.5: Poincaré sections for ion orbits in the drift wave fields. The phase planes are (a,b,c) $v_x = 0$ and (d,e,f) $v_y = 0$. Each curve corresponds to a unique ion initial condition. The plots are generated by 4 ions making roughly 5000 punctures.

They found that while the ion flow pattern qualitatively matched the predictions of simple fluid drift theory, the measured flow velocities were about an order of magnitude lower than the quantitative drift theory prediction. Bailey *et al.* also predicted the ions to have exotic (e.g., flat-topped) velocity distributions when the dynamics are stochastic [14]. This prediction, based on an interpretation of the relation between Poincaré plots and the Vlasov equation, will be discussed and compared with measurements of $f(\mathbf{v})$ in Chapter 6.

It should be emphasized that all of the above arguments regarding stochasticity apply only in the plane perpendicular to $\mathbf{B}$. The approximation that $k_z \approx 0$ renders the z coordinate cyclic, and obviously momentum along z must then be conserved in the model (c.f. Eq. 2.3). Thus, stochastic heating is expected along only the r and θ directions in the poloidal cross section. However, even for $k_z \neq 0$, the heating remains anisotropic. This is because the particle *de*trapping due to $\mathbf{B}$ is an essential ingredient in producing stochastic dynamics. Thus a single electrostatic wave cannot give stochasticity along $\mathbf{B}$. (This case contrasts with that in which *multiple* wave modes propagate along $\mathbf{B}$. With multiple modes, stochasticity along $\mathbf{B}$ is theoretically expected [15] and has been experimentally verified [16].)

Prior to the experiments reported in this thesis, no *multidimensional* velocity-space measurements of the ion distribution function $f(\mathbf{v})$ have been made in the presence of large-amplitude drift waves. Thus, the anisotropic nature of drift-wave stochastic heating has not been observed experimentally, and moreover the distribution of velocities in the toroidal direction has not been examined. In Chapter 4 it will be shown that the toroidal ion heating involves some very interesting physics. The toroidal heating was observed using laser-induced fluorescence to measure ion distribution functions $f(\mathbf{v}, t)$, with high wave-phase resolution and along all three velocity components. The next section discusses the LIF diagnostic.

2.3 Laser-Induced Fluorescence Diagnostics

2.3.1 Introduction

LIF is a highly sensitive, non-perturbing, *in-situ* diagnostic for probing ion distribution functions. Stern and Johnson first demonstrated the technique in a plasma, showing its high sensitivity to ion density and excellent spatial resolution [17]. LIF also offers high time resolution and ease-of-interpretation. Today, LIF is finding broad application in the study of plasmas, combustion and flames [18], and in atmospheric chemistry [19].

The basic LIF procedure is to measure the absorption spectrum $\dot{N}(\lambda)$ of an ionic, atomic, or molecular species with a tunable laser. The absorption spectrum is then used to deduce properties of the absorbing species. For example, (i) When the spectrum is dominated by Doppler broadening, $\dot{N}(\lambda)$ gives information about the distribution of velocities along the laser beam direction (c.f. Appendix A.1). This is the case in Encore. (ii) For spectra which are Stark-broadened or Stark-mixed, $\dot{N}(\lambda)$ can be used to determine local plasma electric fields [20]. (iii) Optical tagging [21], an extension of LIF, allows direct observation of particle transport in both configuration space [22] and velocity space [23]. (iv) An LIF-based diagnostic has also been proposed as an ultra-sensitive measure of local electromagnetic fields by means of the Lamb-shift quenching effect [24].

A schematic of the basic LIF procedure is shown in Fig. 2.6(a). The levels I, E, and F represent internal energy levels of the species considered; they may be states of differing electronic radial quantum number, spin [25], or rotational-vibrational excitation [26]. A 'pump' laser tuned to the resonant wavelength λ_{IE} excites transitions from the initial state I to an excited state E. Subsequently, the state E decays spontaneously to a host of final states, including I as well as others. A detector tuned to the transition wavelength λ_{EF} senses the fluorescence emitted in transitions terminating at a particular final state F; the fluorescence signal quantifies absorption of the laser by state E. Because the fluorescence λ_{EF} is emitted isotropically, it may be collected at right angles to the laser wave vector $\mathbf{k}$. The plasma volume diagnosed

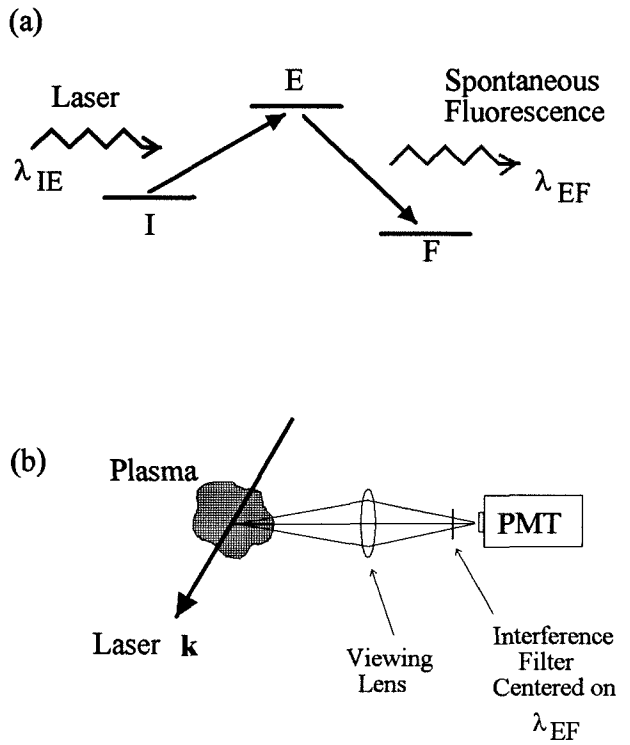

Figure 2.6: (a) Schematic of internal energy levels used for LIF. (b) Basic LIF geometry.

is localized by the intersection of **k** and the viewing optics field (c.f. Fig. 2.6(b)), a significant advantage over chord-averaged passive spectroscopy. Furthermore, the state F can often be chosen so that λ_{EF} is in the range of high detector efficiencies, and $\lambda_{EF} \neq \lambda_{IE}$ allows scattered laser light to be removed from the fluorescence signal with a simple interference filter.

Table 2.1 shows several possible LIF schemes in Ar II. These schemes have relatively high transition probabilities and the initial states are well-populated in Encore plasmas. Note that the initial states used are metastable because transitions from

#	I	E	F	λ_{IE} (nm)	A_{IE} (MHz)	λ_{EF} (nm)	A_{EF} (MHz)
1.	$3d^4F_{9/2}$	$4p^4D_{7/2}$	$4s^4P_{5/2}$	664.48	18.3	434.8	137.0
2.	$3d^4D_{7/2}$	$4p^4D_{7/2}$	$4s^4P_{5/2}$	401.38	11.9	434.8	137.0
3.	$3d^4D_{7/2}$	$4p^4P_{5/2}$	$4s^4P_{5/2}$	440.09	35.7	480.6	87.2
4	$3d^2G_{9/2}$	$4p^2F_{7/2}$	$4s^2D_{5/2}$	611.49	21.2	461.0	75.9

Table 2.1: Ionic energy levels for 4 LIF schemes in Ar II. Also shown are the transition wavelengths and Einstein A coefficients for both the pump transition $I \longrightarrow E$ and fluorescence transition $E \longrightarrow F$.

the Ar II ground state have wavelengths in the 40-90 nm range, inaccessible to most lasers.

All four schemes were experimentally tested [27] to determine which provided the best LIF signal in Encore plasmas. The peak LIF signal was measured as a function of pump laser energy and is plotted in Fig. 2.7. Scheme (1) clearly provided the strongest LIF signal at all laser energies, and was consequently chosen for much of the experimental work in this thesis. Scheme (4), which is undoubtedly the most widely-used Ar II scheme among LIF experimenters [28], gives strong signal in the linear (i.e., low laser energy) regime, although the plot range obscures this fact. Scheme (4) was also extensively used in this work.

2.3.2 Experimental Setup

The LIF laser system consisted of a Lambda Physik FL2001E dye laser pumped by a frequency-doubled or -tripled ND:Yag (Laser Photonics MY-32). The dye laser grating and intracavity etalon were indexed by computer-controlled stepping motors, allowing λ_L to be tuned with < 0.5 pm resolution. The laser pulse length was 10 ns. Since the fluorescence lifetimes of typical excited states used were very short (≈ 10 ns), the resulting narrow LIF pulse was readily distinguished from the plasma's steady-state background emission with a boxcar integrator. Our spatial resolution of 1 cm^3 was also good in comparison with the poloidal drift wavelength of 20 cm.

The chief line-broadening mechanism in Encore plasmas is Doppler broadening. Pressure, Stark, and Zeeman broadening are negligible compared to the ion Doppler width. Thus the resonant wavelength of ions with velocity $\mathbf{v}$ in the laboratory frame

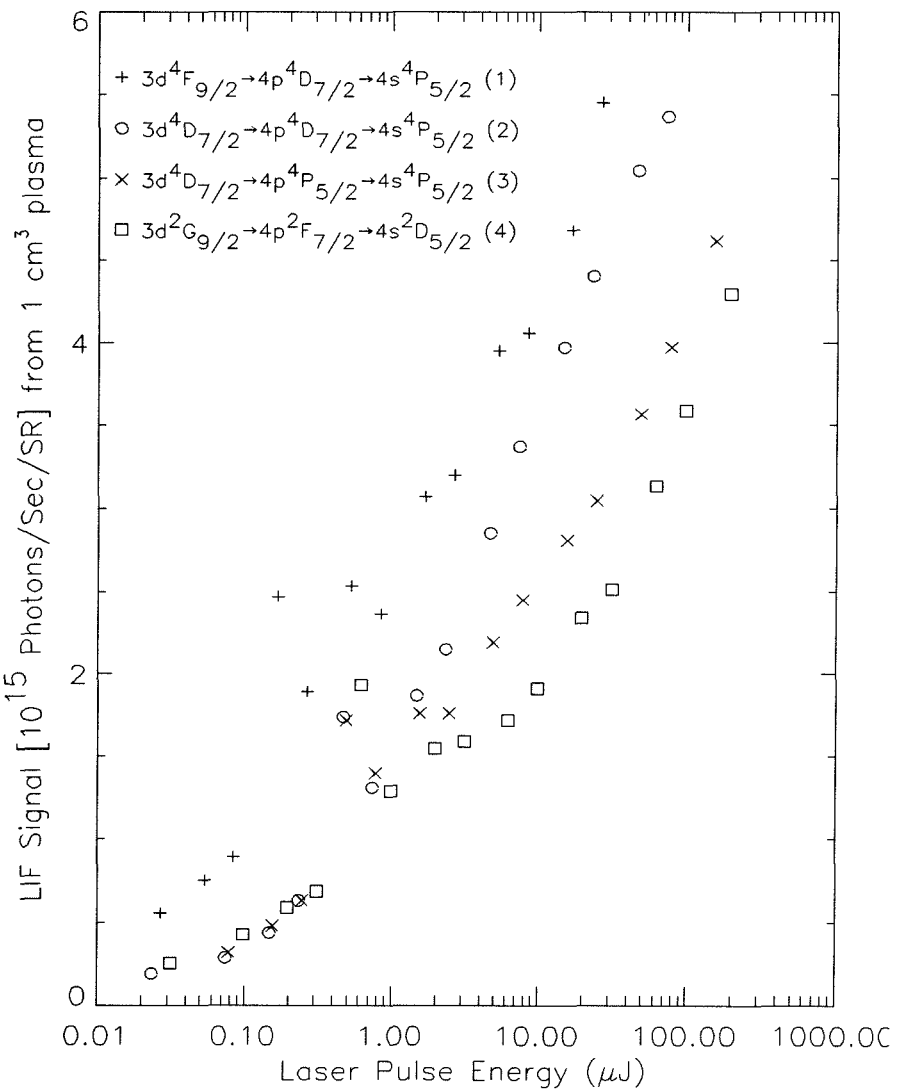

Figure 2.7: Relative LIF signal levels in Encore for 4 good Ar II schemes. Numbering in parentheses corresponds to that in Table 2.1.

is given by the Doppler shift formula $\lambda_{lab} = \lambda_{IE}(1 - v_{\|}/c)$, where $v_{\|} = \mathbf{v} \cdot \mathbf{k}$ and c is the speed of light. Here λ_{lab} is the ion resonance as seen in the lab frame. As shown in Appendix A, the LIF signal Λ at laser frequency λ_L is proportional to the density of ions satisfying $\lambda_{lab} = \lambda_L$:

$$\Lambda(\lambda_L; \lambda_{IE}) \propto f\left(v_{\|} = c\frac{\lambda_L - \lambda_{IE}}{\lambda_{IE}}\right).$$

We obtain $f(v_{\|})$ by scanning λ_L across the resonance λ_{IE} on successive plasma shots. Λ was usually sampled in 0.5-pm intervals over a 60-pm scan range, corresponding to at least 3 or 4 Doppler full-widths. Ion temperature and fluid velocity were then obtained from least-squares fits of $\Lambda(\lambda_L; \lambda_{IE})$ to shifted Maxwellian distribution functions. Examples of measured distribution functions are given in Fig. 2.8.

The Maxwellian fits here are quite good. (See Ch. 5 for counter-examples). Also, the distribution in Fig. 2.8(a), measured very early in the discharge, before significant ion heating occurs, indicates that our experimental temperature resolution exceeds $\Delta T_i \sim 0.27$ eV. This resolution is a function of the dye laser spectral width $\Delta\nu_{laser}$, which is, in principle, determined by the finesse of the intracavity etalon. In practice it was found that $\Delta\nu_{laser}$ was also a function of the dye solution recipe[1]. Note that $\Delta T_i = 0.27$ eV is a significant improvement over the resolution reported by Bailey [29] and is more than adequate to study the dynamics of the hot ions in Encore ($T_i = 1 - 10$ eV).

A schematic of the experimental layout and control system is shown in Fig 2.9. During each discharge the LIF intensity, the background plasma emission (measured 100 ns before the LIF pulse), and the laser pulse energy were digitized. The ion saturation current drawn by a static Langmuir probe was also digitized, to monitor drift wave phase; this will be discussed in detail in Chapter 3. Trigger timing for these digitizer gates, as well as for the laser flashlamps and Q-switch, was referenced to the 15 Hz OH pulse trigger. The OH trigger was in turn phase locked to the 60 Hz

[1]To pump the 611 nm line, the best solution was found to be 0.3 g Rhodamine 640/liter methanol. McChesney and Bailey used combinations of R640 and Kiton Red. The latter may have been better suited for pumping by Cu vapor laser.

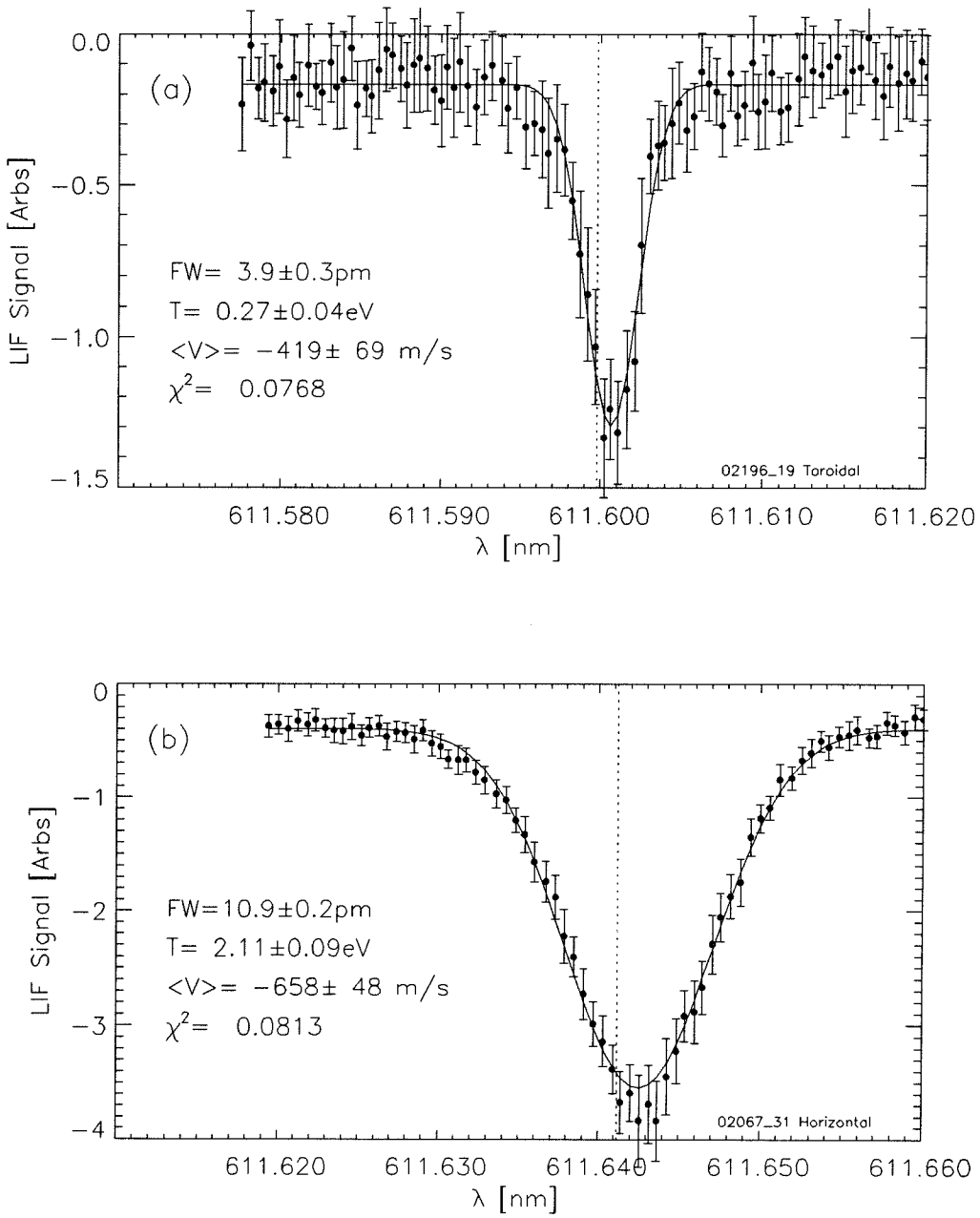

Figure 2.8: Doppler-broadened ion absorption spectra corresponding to (a) toroidal and (b) poloidal velocity distributions. Solid lines are best-fit Maxwellian curves, and dotted lines indicate 0 ion velocity.

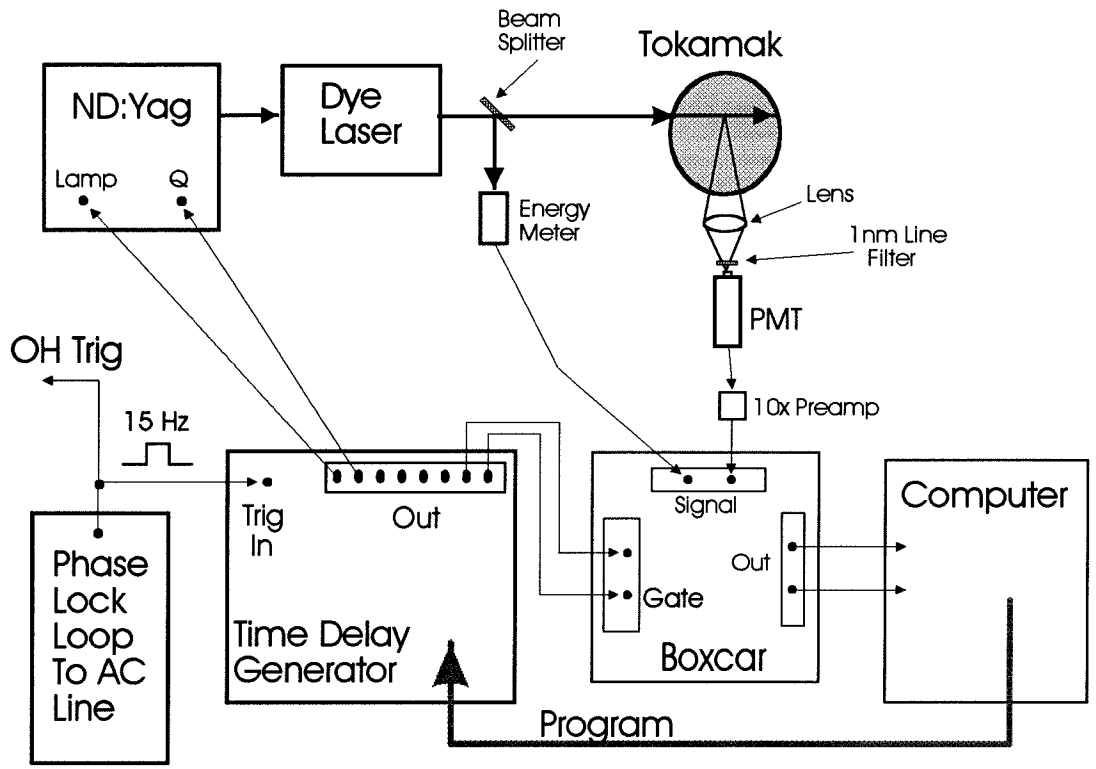

Figure 2.9: Schematic of experimental control system.

line. A programmable 8-channel time delay generator (CAMAC module designed and built by Frank Cosso) provided independent, 50 ns time resolution for each trigger. The laser Q-switch and lamp triggers were transmitted via optical fiber, to prevent substantial electrical Q-switch noise from returning to the data acquisition electronics.

A 90 MHz Pentium computer (PC) controlled the laser wavelength and programmed the CAMAC timing module. The PC also derived $\Lambda(\lambda_L)$ from the raw PMT signal on a shot-by-shot basis. This calculation consisted of background subtraction and laser energy normalization in real time, followed by averaging over 30-100 shots to reduce noise from laser energy jitter and fluctuations in plasma breakdown.

This need for averaging, coupled with the necessity to vary λ_L between discharges, means that some 3000 plasma shots were used to measure the velocity-dependence of a single distribution $f(\mathbf{x}, \mathbf{v}, t)$ at fixed $\mathbf{x}$ and t. The drift waveform had to be extremely reproducible from shot to shot because any jitter in the phase of the drift wave would smear out phase-sensitive details. To ensure low phase jitter, we built a new data acquisition system which examined the wave pattern in real time and rejected data from discharges with excessive phase jitter. The details of this 'wave-selective' data acquisition system are the subject of the next chapter.

Bibliography

[1] I.H. Hutchinson, *Principles of Plasma Diagnostics* (Cambridge University Press, New York, 1987).

[2] E.D. Fredrickson and P.M. Bellan, "Investigation of finite beta modified drift wave in a tokamak plasma," *Phys. Fluids* **28**, 1866 (1985).

[3] G. Schmidt, *Physics of High Temperature Plasmas* (Academic Press, New York, 1979).

[4] X.H. Shi, B.D. Blackwell, and S.M. Hamberger, "Studies of drift waves in a toroidal heliac," *Plasma Phys. Contr. Fusion* **31**, 2011 (1989).

[5] O. Sakai and Y. Yasaka, "Bifurcated transition of radial transport in the HIEI tandem mirror," *Phys. Plasmas* **2**, 3249 (1995).

[6] B.B. Kadomtsev, *Plasma Turbulence* (Academic Press, London, 1965).

[7] J.M. McChesney, P.M. Bellan, and R.A. Stern, "Observation of fast stochastic ion heating by drift waves," *Phys. Fluids B* **3** 3363 (1991).

[8] A.B. Mikhailovskii, *Theory of Plasma Instabilities* (Consultants Bureau, New York, 1974).

[9] J.M. McChesney, R.A. Stern, and P.M. Bellan, "Observations of fast stochastic ion heating by drift waves," *Phys. Rev. Lett.*, **59**, 1436 (1987).

[10] C.F.F. Karney and A. Bers, "Stochastic ion heating by a perpendicularly propagating electrostatic wave," *Phys. Rev. Lett.*, **39**, 550 (1977).

[11] G.R. Smith and A.N. Kaufman, "Stochastic acceleration by a single wave in a magnetic field," *Phys. Rev. Lett.*, **34**, 1613 (1975).

[12] A.A. Chernikov et al., *Nature* **326**, 559, 1987; A.A. Chernikov, R.Z. Sagdeev, and G.M. Zaslavsky, *Physics Today* (November, 1988).

[13] A.D. Bailey III, R.A. Stern, and P.M. Bellan, "Measurement of coherent drift-wave ion-fluid velocity field when ion dynamics are stochastic," *Phys. Rev. Lett.*, **71**, 3123 (1993).

[14] A.D. Bailey III, P.M. Bellan, and R.A. Stern, "Poincare maps define topography of Vlasov distribution functions consistent with stochastic dynamics," *Phys. Plasmas* **2**, 2963 (1995).

[15] D.F. Escande, "Stochasticity in classical Hamiltonian systems - universal aspects," *Phys. Rep.*, **121**, 165 (1985).

[16] A. Fasoli et al., "Dynamical chaos of plasma ions in electrostatic waves," *Phys. Rev. Lett.*, **70,** 303 (1993).

[17] R.A. Stern and J.A. Johnson III, " Plasma ion diagnostics using resonant fluorescence," *Phys. Rev. Lett.*, **34**, 1548, (1975).

[18] M. Yorozu, Y. Okada, and A. Endo, "Two-dimensional rotational temperature measurement by multiline laser induced fluorescence in nitric oxide of combustion flame," *Optical Review* **3**, 293 (1996); M. Kollner and P. Monkhouse, "Time-resolved LIF of OH in the flame front of premixed and diffusion flames at atmospheric pressure," *Appl. Phys. B* **61**, (1995).

[19] J.J. Mather, P.S. Stevens, and W.H. Brune, "OH and $H0_2$ measurements using laser-induced fluorescence," *J. Geophys. Res.*, **102**, 6427 (1997); C.E. Canosa-Mas et al., "Is the reaction between $CH_3C(O)O_2$ and NO_3 important in the night-time troposphere?" *J. Chem. Soc., Faraday Trans.*, **92**, 2211 (1996).

[20] C.A Moore, G.P. Davis, and R.A. Gottscho, "Sensitive, nonintrusive, *in-situ* measurements of temporally and spatially resolved plasma electric fields," *Phys. Rev. Lett.*, **52**, 538 (1984).

[21] R.A. Stern, D.N. Hill, and N. Rynn, "Direct ion transport measurement by optical tagging," *Phys. Lett. A* **93**, 127 (1983).

[22] A. Fasoli et al., "Cross-field diffusion quenching by neutral gas injection in a magnetized plasma," *Phys. Rev. Lett.*, **68**, 2925 (1992).

[23] J. Bowles, R. McWilliams, and N. Rynn, "Direct measurement of velocity space transport in a fully ionized plasma," *Phys. Rev. Lett.*, **68**, 1144 (1992).

[24] R.A. Stern and J.F. Benage, Jr., "Lamb shift quench radiation in plasmas," *Bull, Am. Phys. Soc.*, **36**, 2487 (1991).

[25] F. Skiff et al., "Plasma diagnostics with spin-polarized ions," *Phys. Lett. A* **137**, 57 (1989).

[26] J.P. Booth et al., "Quantitative laser-induced fluorescence spectroscopy of the CF $A^2\sum^+ - X^2\Pi$ transition: Electronic transition dipole moment function and predissociation," *J. Phys. Chem.*, **47** (1996).

[27] J.M. McChesney, "A laser-induced fluorescence diagnostic for divertors," Final Report, DOE Grant No. DE-FG03-92ER54150.

[28] M.J Goeckner, J. Goree, and T.E. Sheridan, "Saturation broadening of laser-induced fluorescence from plasma ions," *Rev. Sci. Instrum.*, **64**, 996 (1993).

[29] A.D. Bailey III, "Drift Wave Ion Fluid Velocity Field Measured by Planar Laser Induced Fluorescence." Ph.D. Dissertation, California Institute of Technology, 47 (1993). Bailey saw no temperatures below 1 eV.

Chapter 3 Real-Time Wave Discrimination to Alleviate Phase Jitter

3.1 Introduction

The investigation of wave phenomena in short-lived physical systems, such as pulsed plasma discharges, poses unique experimental challenges. The difficulty lies in synchronizing measurements to the wave phase: measurement timing is easily referenced to the pulse initiation, whereas the relevant wave phase may fluctuate substantially from pulse to pulse due to sensitive dependence on microscopic initial conditions. This situation applies to Encore plasmas, which have large fluctuations in both drift wave phase and amplitude on successive shots. These fluctuations adversely affect the use of any diagnostic requiring data from multiple discharges to form a complete measurement. In particular, two of the most widely-used plasma diagnostics, laser-induced fluorescence (LIF) and Langmuir probes, require multiple plasma shots for each data point. With LIF, a probing laser must be scanned across a plasma absorption line to deduce an ion velocity distribution. Langmuir probe measurements of plasma potential and electron temperature require the probe bias be scanned to obtain the plasma current-voltage characteristic. Since these were the two principal diagnostics used for this thesis work, alleviating the phase jitter problem was crucial.

This chapter describes a new data-acquisition system which was developed to ensure synchronization between the phase-jittering drift waves and measurements made by any of the Encore diagnostics. Although the method was designed specifically for Encore plasmas, it should be well-suited for other repetitive experiments with wave phase jitter. Section 3.2 discusses the wave jitter and experimental parameters in the Encore device. Section 3.3 presents the details of the new acquisition system. Section 3.4 shows the reduction in phase jitter provided by the new data acquisition system.

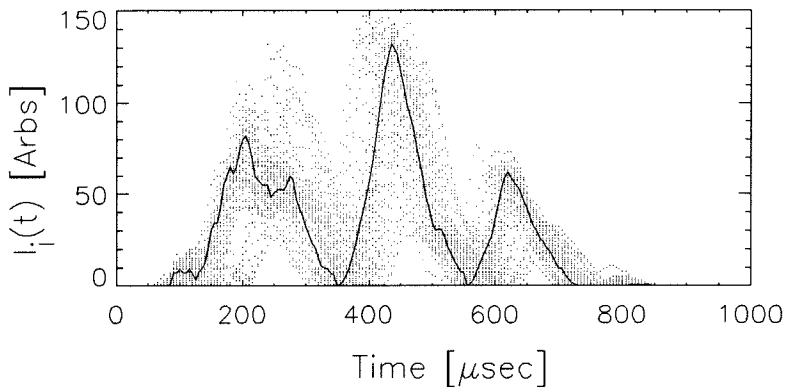

Figure 3.1: 50 ion saturation current traces, showing shot-to-shot jitter in the drift wave phase and amplitude. The time origin is fixed relative to the trigger time of the Ohmic heating pulse.

3.2 Wave Jitter in Encore Plasmas

The dominant source of experimental noise in Encore discharges was shot-to-shot jitter in the drift wave pattern. Examples of the shot-to-shot variations are displayed in Fig. 3.1. The solid curve shows the ion saturation current measured by a Langmuir probe during one representative shot. The dotted traces are the current waveforms from the next 50 shots. As can be seen, consecutive shots routinely vary by $\pm 90°$ in wave phase and by as much as $\pm 15\%$ in amplitude.

To see the problem imposed by this wave phase jitter, consider the experimental timing for an LIF experiment, as shown schematically in Fig. 3.2. An individual discharge is initiated by the Ohmic heating pulse at time t_{OH}, and the plasma lifetime is $\tau_{plasma} \approx 1$ msec. The discharge repetition rate, $f_{rep} = 15$ Hz, is determined by the Ohmic heating power supply. The figure shows two successive discharges with drift waves out of phase by 180°, corresponding to the extreme limit of the phase fluctuation mentioned above. The wave amplitudes also differ slightly.

Now consider an LIF measurement performed at time t_L. The laser trigger t_L is generated by a programmable delay δt referenced to t_{OH}. The laser pulse width is much shorter than the wave period, so that the LIF signal is a measure of the ion

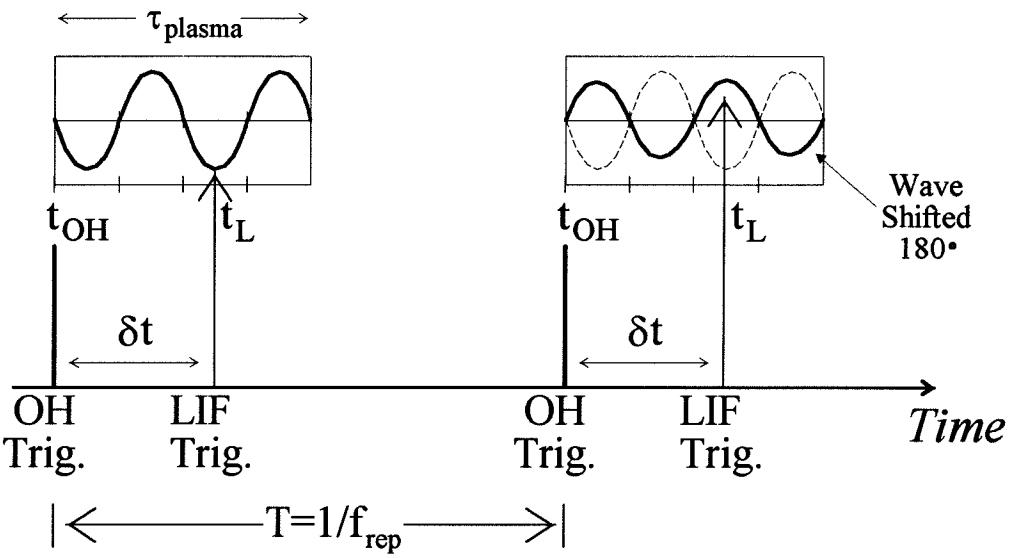

Figure 3.2: Layout of experimental timing for LIF measurement in pulsed plasma discharge.

absorption $A_1(t_L)$, where the subscript 1 denotes measurement of discharge 1. During discharge 2 the laser is fired at the *same* delay δt but the wave phase has shifted 180°, meaning that the two successive measurements interrogate exactly opposite wave phases. Clearly if the wave phase continues to fluctuate by exactly 180° from shot to shot, then an ensemble average over many measured samples will 'smear' the phases together and destroy the experimental phase resolution. Note that fluctuating wave phase is very different from the case of fluctuating wave amplitude. For fixed phase, random amplitude fluctuations are eliminated by simple averaging, i.e., the ensemble average $\overline{A}(t_L) = N^{-1} \sum A_i(t_L)$ converges to the 'true' value of $A(t_L)$, and the r.m.s. deviation $\left[(N-1)^{-1} \sum (\overline{A} - A_{true})^2\right]^{1/2}$ decreases like $N^{-1/2}$, where N is the number of measured samples. This example demonstrates that averaging over fluctuating wave amplitude is permissible but averaging over fluctuating wave phase is not. In the language of statistics, $\overline{A}$ is not an unbiased estimator of A_{true} if the wave phase fluctuates.

A common approach to ameliorate the phase jitter problem is to trigger the

laser directly on the wave phase by continuously monitoring the phase using a second diagnostic, for example a Langmuir probe: when the measured wave signal surpasses some predefined threshold, t_L is triggered. However, this method works only if the laser can be triggered in a time short compared to τ_{plasma}. The YAG-based LIF system used for this thesis work required a 760 μsec delay between the flashlamp and Q-switch triggers, whereas the plasma lifetime was only about 1000 μsec. Thus a phase-triggered flashlamp could easily delay the Q-switch trigger until after the discharge terminated and moreover would not allow for interrogation of early wave phases. Also, the observed drift wave jitter of $\pm$100 μsec was greater than the $\pm$40 μsec tolerance in the flashlamp-Q-switch delay, meaning that the Q-switch trigger could not be directly referenced to wave phase.

Numerous attempts were made to eliminate the phase jitter directly by improving the maintenance of the Ohmic heating power supply (the MB amplifier) or the electron source used to assist with plasma breakdown, but these were only partially successful. For example, a new set of rectifiers installed in the amplifier improved repeatability by 20-30%, but this was still not satisfactory. New electron source filaments also provided some improvement, but the improvement decayed after of a few days of running time. Thus, a more permanent and effective method of reducing the shot-to-shot phase jitter was needed.

3.3 Waveform Discrimination Technique

To reduce the experimental uncertainty in drift wave phase and amplitude, we assembled a new, wave-selective data acquisition system (WDAS) which selected plasma discharges with low wave phase and amplitude deviation from a predefined 'nominal' waveform. Discharges with deviation greater than a pre-established threshold were rejected and LIF data from those shots were ignored. Conversely, shots with deviation lower than the threshold were accepted, and LIF data from those shots were used to measure $f(\mathbf{v}, t)$. This method ensured that the waves used for averaging purposes were selected from a *subset* of discharges having low phase and amplitude scatter.

The WDAS used the ion saturation current $I_i^{ref}(t)$ collected by a 'reference' Langmuir probe as a measure of the drift wave pattern. Prior to beginning an experiment, a set of 100 such $I_i^{ref}(t)$ were digitized at a 200 kHz sampling rate (Transiac Model 2008 transient digitizer), and a nominal drift waveform $I_i^{nom}(t)$ was chosen from among this set, based on its statistical representation within the set; this waveform was stored for comparison to $I_i^{ref}(t)$ obtained in later shots.

For each shot during an experiment, $I_i^{ref}(t)$ was digitized, and the data from any other diagnostic, such as the LIF system, were separately digitized (Kinetic Systems ADC 3553) and temporarily stored. The digitized samples of each $I_i^{ref}(t_k)$ were compared in real time to the stored $I_i^{nom}(t_k)$ by means of a linear Pearson correlation function [1]; here t_k refers to the time of the k^{th} digitized sample. With the notation

$$\left\{ \begin{array}{l} R_k = I_i^{ref}(t_k) \\ N_k = I_i^{nom}(t_k) \end{array} \right\},$$

the Pearson correlation may be written

$$C(N,R) = \frac{\sum_k (N_k - \overline{N})(R_k - \overline{R})}{\sqrt{\sum_k (N_k - \overline{N})^2}\sqrt{\sum_k (R_k - \overline{R})^2}},$$

where $\overline{N}$ and $\overline{R}$ are the averages of the sequences N_k and R_k. Note that $C = 1$ if $N_k = R_k$ for all k, and $C = -1$ if $N_k = -R_k$. For uncorrelated sequences, $C = 0$. Thus a value of $C(I_i^{ref}, I_i^{nom}) \approx 1$ indicates good phase and amplitude agreement between a given shot and the nominal waveform. Figure 3.3 shows a schematic representation of the WDAS setup.

The correlation $C(I_i^{ref}, I_i^{nom})$ was computed in real time for every discharge by a 100-MHz Pentium computer. For discharges with C exceeding the predefined threshold C_t, the stored LIF data were used to compute $f(\mathbf{v}, t)$. For discharges with $C < C_t$, the LIF data were discarded. Typically, $C_t = 0.92 - 0.96$ was used. The 67 milliseconds between discharges was ample time to calculate $C(I_i^{ref}, I_i^{nom})$ and also perform other simple calculations on the LIF data.

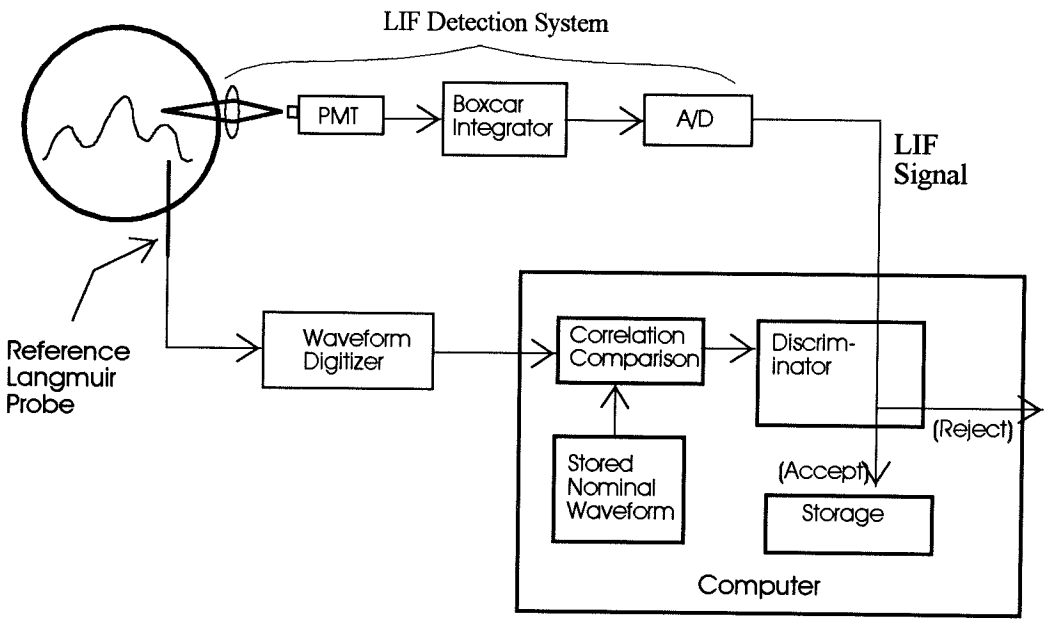

Figure 3.3: Schematic of real-time data acquisition system used to select plasmas with low phase jitter.

3.4 Improvement in Wave Jitter

Typical sets of waveforms selected by this correlation method are shown in Fig. 3.4, for various thresholds C_t. The nominal waveform $I_i^{nom}(t)$ is the solid curve in each plot. The data in Fig. 3.4(a) include all shots for which the correlations exceed only $C_t = 0.31$, a very minimal threshold. These data show large phase fluctuations, implying that LIF measurements referenced to t_{OH} sample a wide range of wave phases on successive shots. One expects this phase uncertainty to smear the measured wave structure, as described above. The data in 3.4(c) include only those shots with $C \geqslant C_t = 0.93$; here the phase uncertainty is markedly reduced. In each case, 20 shots are shown. To obtain a set of 20 shots satisfying $C \geq C_t$ for each C_t shown in (a) through (c), respectively, the WDAS sifted through 23, 27, and 47 total plasma shots.

Figure 3.5(a) shows a scatter plot of measured correlations for 200 consecutive shots. These data indicate that the wave phase fluctuates essentially randomly on a shot-by-shot basis; discharges with similar wave patterns do not occur in bunches. Figure 3.5(b) shows the probability distribution $f(C)$ of shots with correlation C. The pronounced peak near $C \approx 1$ indicates that the chosen nominal waveform is indeed representative of the most probable waveform. Figure 3.5(c) shows the fraction of discharges with $C \geqslant C_t$, i.e., $F(C_t) = \int_{C_t}^{1} f(C)\, dC$. This last plot illustrates the obvious disadvantage of the correlation selection scheme: increasing C_t rapidly decreases the frequency of acceptable shots. For example, 77% of typical shots have $C \geqslant 0.6$, while only 27% have $C \geqslant 0.95$.

The efficacy of the WDAS in reducing experimental noise can be quantified by tabulating the phase φ of each wave, relative to a fixed time origin. We define $\varphi_i = (t_i^{peak} - t_{OH})/\tau_{wave}$, where τ_{wave} is the wave period and t_i^{peak} is the time at which $I_i(t)$ achieves its absolute maximum. Typically, $t_{peak} \approx 430$ μsec (c.f. Fig. 3.4). Figure 3.6(a) shows the variance $\Delta\varphi = \left[(N-1)^{-1} \sum (\varphi_i^2 - \overline{\varphi})^2\right]^{1/2}$, obtained from an ensemble of $N = 80$ wave patterns and acquired using five different values of C_t. Clearly the correlation threshold is a sensitive control of $\Delta\varphi$: by increasing C_t from

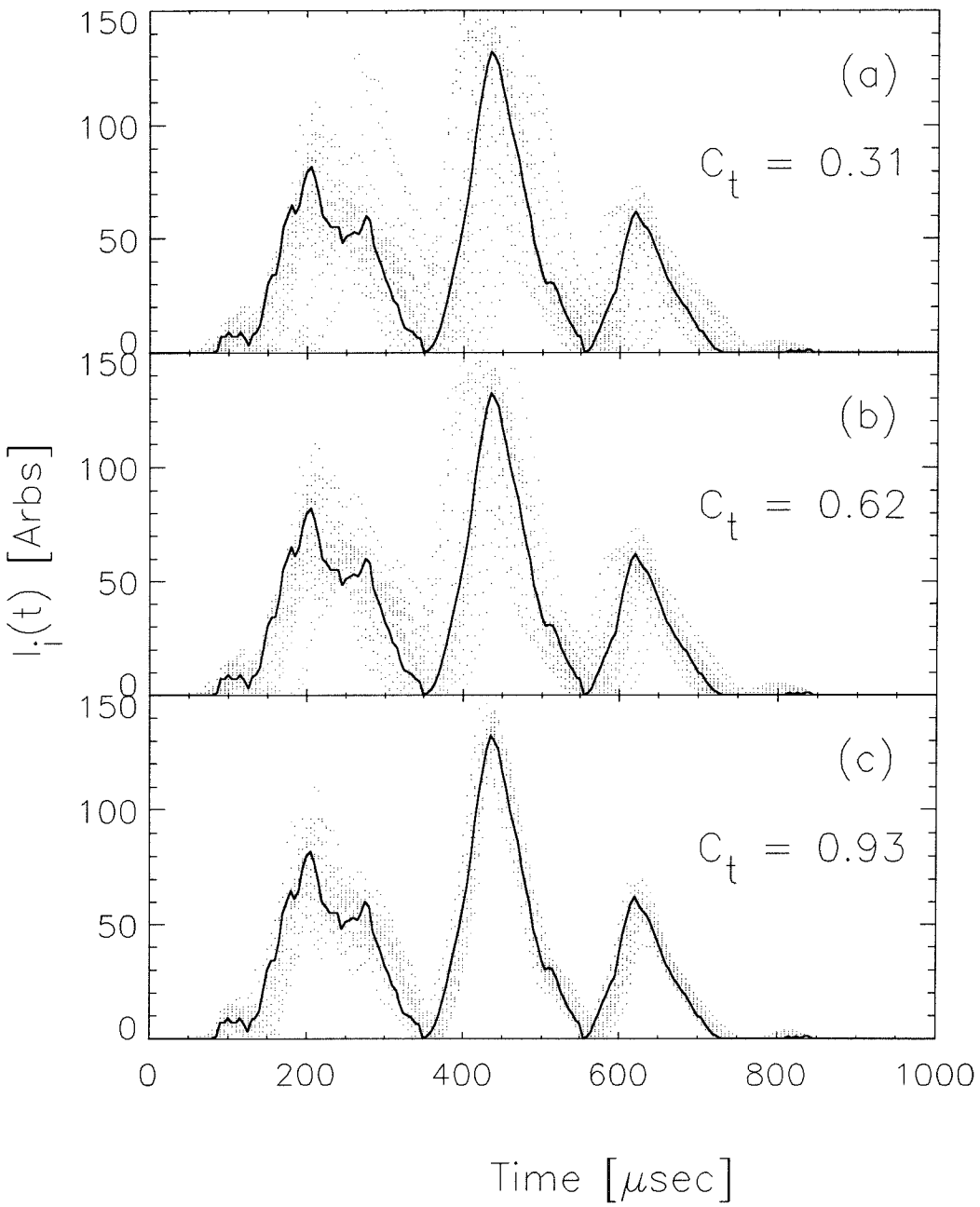

Figure 3.4: Sets of ion saturation current waveforms $I_i(t)$ with minimum correlation thresholds shown. The fraction of shots typically exceeding these minimum thresholds is (a) 89%, (b) 76%, and (c) 42%.

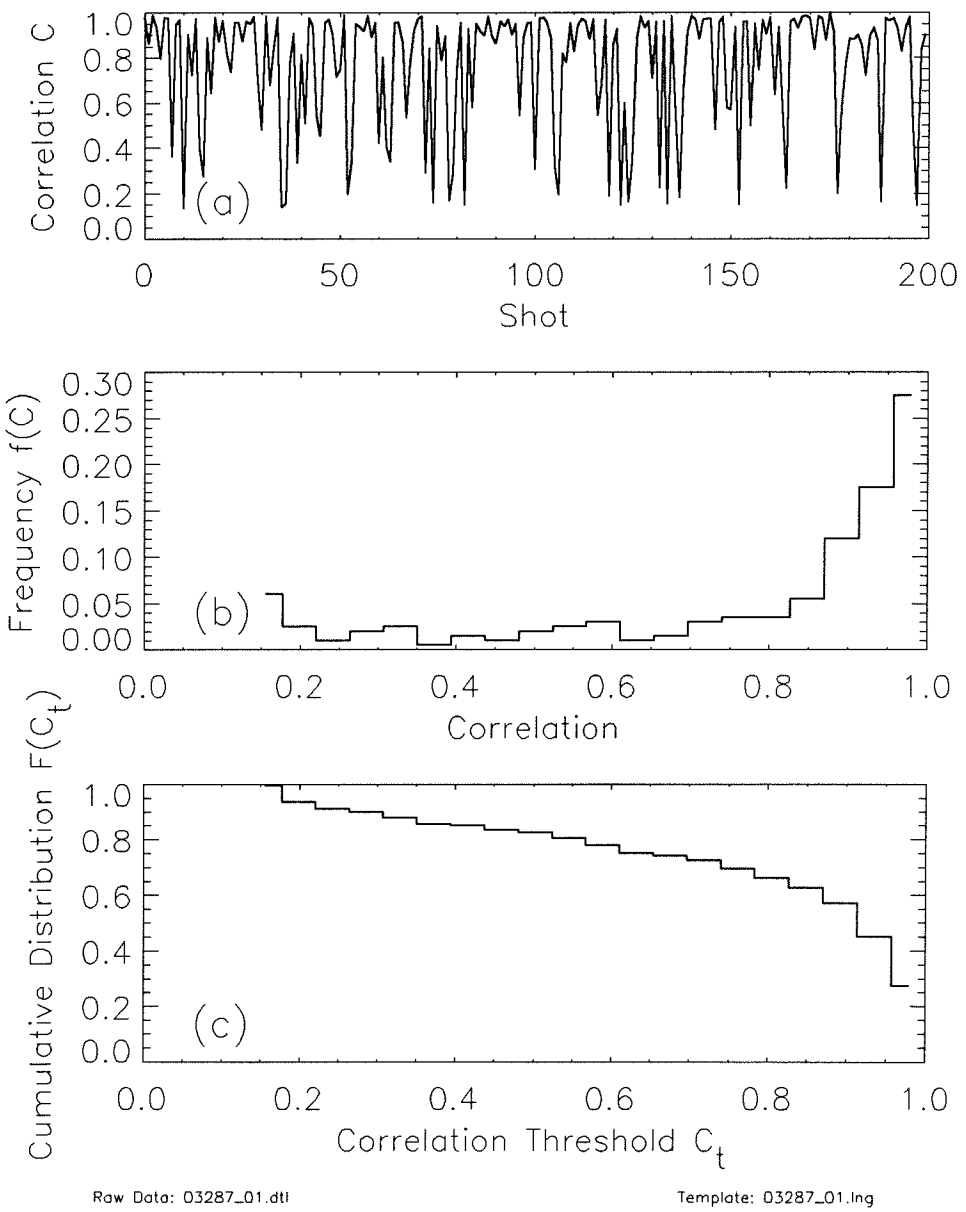

Figure 3.5: (a) Scatter plot of measured correlations for 200 consecutive shots. (b) Relative frequency of shots with correlation C. (c) Fraction of discharges with $C \geqslant C_t$.

0.30 to 0.93, $\Delta\varphi$ decreases from 76° to 14°.

This reduction in phase jitter has a profound effect on measurements made by any of the other Encore diagnostics. As an example, Fig. 3.7 shows ion density $n(t)$ and plasma potential $\phi_p(t)$, for several values of the acquisition threshold C_t. These data were obtained from a second Langmuir probe located near the LIF ports. One sees that for low C_t, the data are strongly smeared by the effect of averaging over the jittering wave phases, as expected. For instance, use of $C_t = 0$ leads one to conclude that the amplitude of the density fluctuations $\tilde{n}/n$ is almost 50% below its 'true' value; similarly, the inferred $\tilde{\phi}_p/\phi_p$ is reduced by 20% from its true value. Using $C_t \approx 0.93$ dramatically reduces the smearing effect.

For all of the data in this thesis, the threshold was set at $C_t \approx 0.93$. This value of C_t was felt to yield a good compromise between phase noise reduction (a factor of 6 improvement) and increased data acquisition time (a factor of 2.5 longer).

3.5 Conclusion

The WDAS vastly improved our experimental wave phase resolution, and thus our ability to observe ion dynamics in concert with the drift waves. As a result, we have observed several phenomena not previously seen in Encore. These include:

- oscillations of collisionality and rapid collisional relaxation of ion temperature anisotropies (Ch. 4)
- observations of thermalized-ion wall recycling (Ch. 5)
- clear observations of ion transport during drift wave formation (Ch. 6)

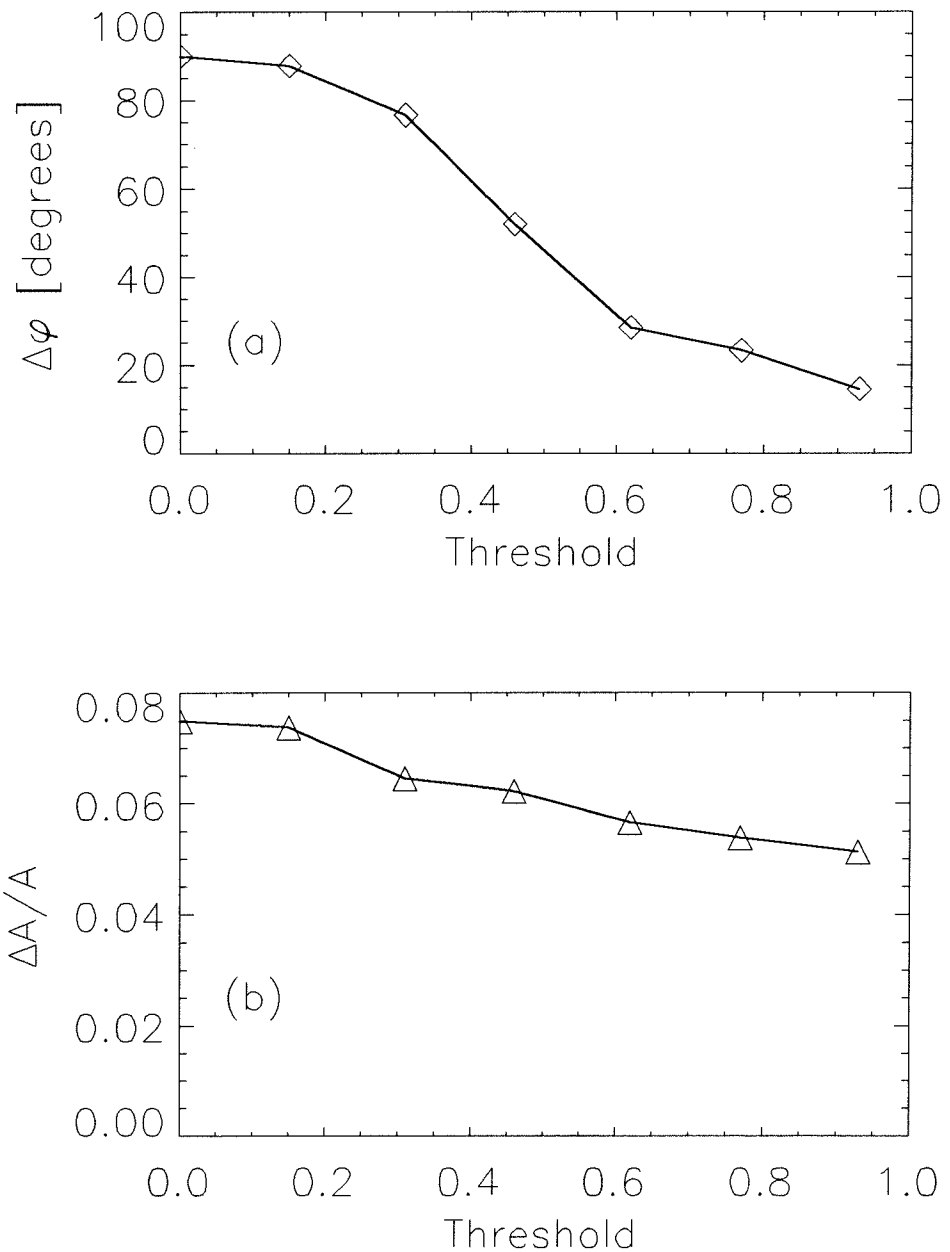

Figure 3.6: (a) Measured uncertainty in the drift wave phase (relative to a fixed time origin) as a function of C_t. (b) Relative uncertainty in wave amplitude.

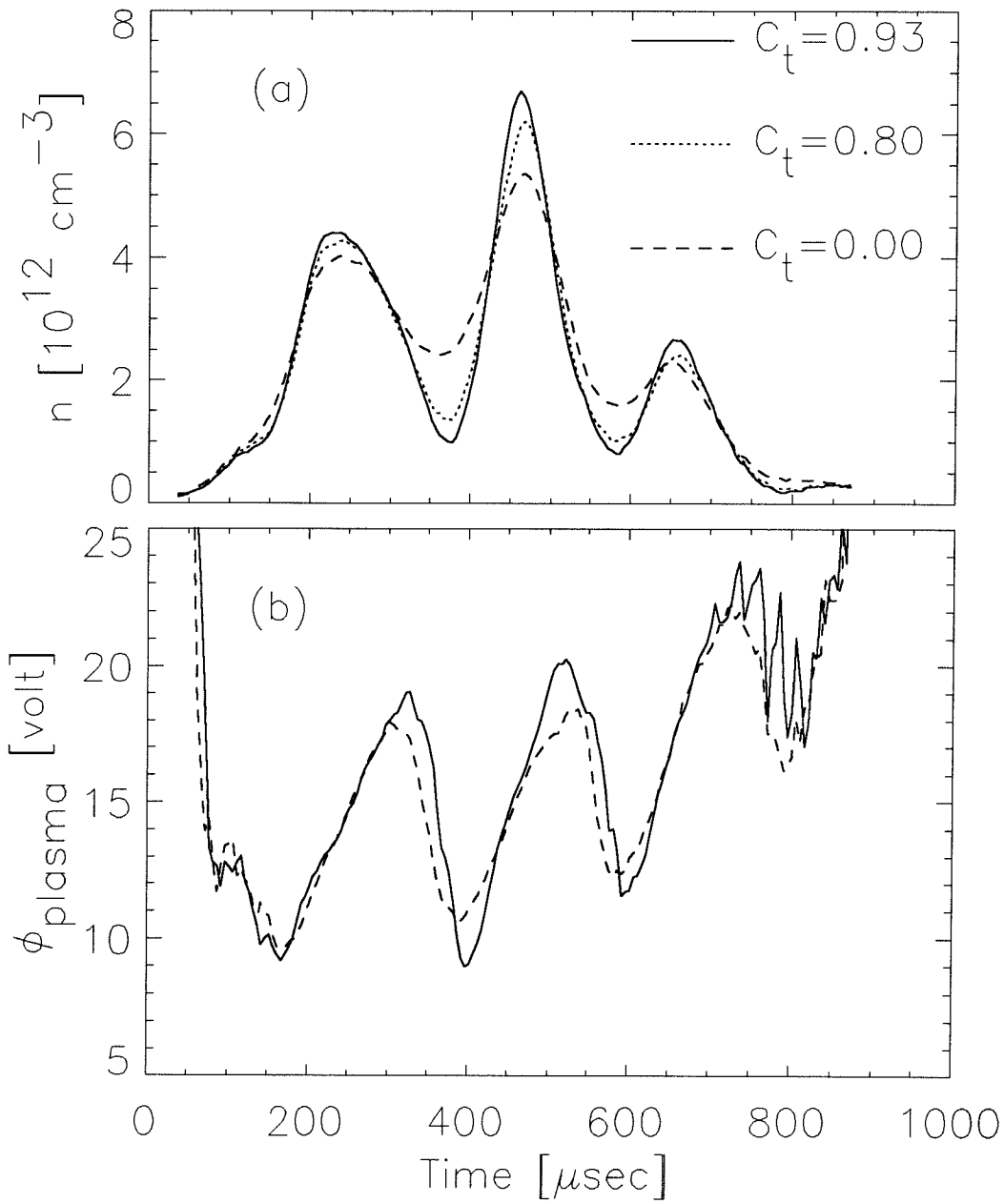

Figure 3.7: (a) Ion density and (b) plasma potential obtained from Langmuir probe measurements. The measurement was repeated using a range of C_t, to examine the effect of smearing due to wave phase jitter. $C_t = 0$ corresponds to indiscriminate averaging over all shots. For clarity, the ϕ_p plot shows only two values of C_t.

Bibliography

[1] W.H. Press *et al.*, *Numerical Recipes in Fortran* (Cambridge University Press, New York, 1992).

Chapter 4 Ion Temperature Measurements in 3 Velocity Dimensions

4.1 Introduction

Hamiltonian stochasticity in plasmas has been extensively studied in recent years. In particular, nonlinear interactions between plasma particles and intense waves provide a valuable testbed for our understanding of nonlinear dynamics and anomalous particle transport. Many experimental tests have been conducted: Doveil observed stochastic electron heating by standing Gould-Trivelpiece waves [1]; Skiff, Anderegg, and Tran determined the threshold for stochastic ion heating by a neutralized ion Bernstein wave [2]; the breakdown of Hamiltonian conservation laws [3] and exponential divergence of ion orbits [4] have also been observed in the presence of large-amplitude waves. All of these experiments were conducted in low-density, collisionless plasmas, where stochasticity could be examined without the interference of collisional transport, i.e., these experiments had $\omega\tau \gg 1$, where ω was the exciting wave frequency and τ, the collision period for the species of interest.

As discussed in Chapter 2, stochastic ion heating has also been observed in Caltech's Encore tokamak [5], [6]. Like Refs. [1]-[4], previous work in Encore focused solely on ion stochasticity and neglected consideration of collisional effects. However, in the course of this thesis work, it became evident that collisions may be important in the drift wave heating cycle. Therefore, a measurement of the ion-ion collision rate *during stochastic ion motion* became desirable. Although the ion-ion collision frequency, ν_{ii}, could be estimated from measurements of n and T_i, together with the Spitzer formula $\nu_{ii} \sim nT_i^{-3/2}$ [7], it was unclear *a priori* whether the classical Spitzer result, based on small-angle Coulomb scattering, was valid during stochastic heating, because collisional theory has not been experimentally tested when particle dynamics

are chaotic. In short, it was unknown how stochasticity would affect collisions. Conversely, because stochastic heating in collisional plasmas has scarcely been examined, it was unclear how collisions would affect the stochasticity. Thus a direct measurement of ν_{ii} was in order. To determine ν_{ii}, we measured ion distribution functions both perpendicular to ($\perp$) and along ($\parallel$) the toroidal magnetic field $\mathbf{B}$. Since stochastic heating is expected to act only perpendicular to $\mathbf{B}$ (c.f. Section 2.2.2), ion heating along $\mathbf{B}$ should be effected by collisions only. Therefore, measurements of the parallel heating rate $dT_{i\parallel}/dt$ reveal information about ν_{ii}.

This chapter is organized as follows. Section 4.2 presents the measured distribution functions $f(\mathbf{v},t)$ and thus $T_i(t)$. As expected, $T_{i\perp}$ heats rapidly, on time-scales characteristic of stochasticity. $T_{i\parallel}$ appears to heat classically, with ion-ion collisions equilibrating ion energy between the $\perp$ and $\parallel$ directions. Fast ion *cooling* is also observed, with the heating and cooling occurring cyclically, in synchronism with the drift wave oscillations. Section 4.3 quantitatively compares the observed heating of $T_{i\parallel}$ with a Fokker-Planck collisional model. It is shown that (i) the observed ν_{ii} fluctuates strongly with the wave, resulting in a plasma which oscillates between being collisional and being collisionless, and (ii) the observed $dT_{i\parallel}/dt$ agrees with collisional theory defined in an instantaneous sense. Section 4.4 discusses possible ion energy-loss mechanisms which could account for the observed periodic ion cooling. Conclusions are discussed in Section 4.5.

4.2 Experimental Data

Figure 4.1 shows our experimental arrangement designed to measure simultaneously two velocity components of $f(\mathbf{v})$. The dye laser beam was split near its output aperture, and the two beams were directed through the same plasma volume at right angles to each other, thereby probing two orthogonal components of $f(\mathbf{v})$.

The use of a long (85 m) optical fiber to deliver Beam 2 to the plasma introduced a 300 nanosecond time separation between the two beams. Thus the 10-ns fluorescence signals induced by the two beams were also separated by 300 ns and were measured

with independently-gated boxcar channels. Since 300 ns was negligible compared to the drift wave period τ_{wave}=230 μsec, the two beams sampled orthogonal chords in velocity space at essentially the same wave phase. The evolution of $f(\mathbf{v})$ in the wave was then determined by varying the laser trigger time and sampling $f(\mathbf{v}, t)$ in 10-μsec intervals. The fiber was then reoriented and the procedure repeated to interrogate the third velocity component.

4.2.1 Heating Perpendicular to B

Figure 4.2(a) plots the measured time evolution of two components of the perpendicular ion temperature $T_{\perp r}$ and $T_{\perp\theta}$, in the presence of large-amplitude drift waves. (T with no species subscript is understood to refer to ions.) Ion density $n(t)$, measured simultaneously by Langmuir probe, is shown in Fig. 4.2(b) for comparison. These measurements were performed 4 cm from the tokamak wall, where the drift wave amplitude was largest. Here the space potential fluctuation was $\tilde{\phi}_p = 6$ volt, giving $\alpha = 2.3$, well above the stochastic heating threshold of McChesney, Stern and Bellan [5]. Very strong ion temperature fluctuations, coherent with the drift wave, are evident in the figure. There is a large phase delay ($\approx 130°$) between the n and T fluctuations, and we find that this phase relationship is inconsistent with what would follow from an adiabatic ion equation of state, namely $Tn^{1-\gamma} = const$, where γ is the ratio of ion specific heat at constant pressure to that at constant volume. Thus the ion temperature fluctuations are non-adiabatic and cannot be explained by standard theories which close the chain of dynamical equations by an ideal state equation. At all wave phases, however, we observe that $T_{\perp r}(t)$ and $T_{\perp\theta}(t)$ are equal, within experimental error. The isotropic nature of the heating in this plane is characteristic of stochasticity (c.f. Ch. 2.2.2).

Also characteristic of stochastic dynamics is the extremely fast heating rate observed here, $\dot{T}_\perp \approx 0.1$ eV/μsec. Such a heating rate is 2.5× faster than that reported by McChesney *et al.* and is commensurate with our value of α, also 2-3× higher [8]. Following McChesney *et al.*, we now show that the ion heating is much

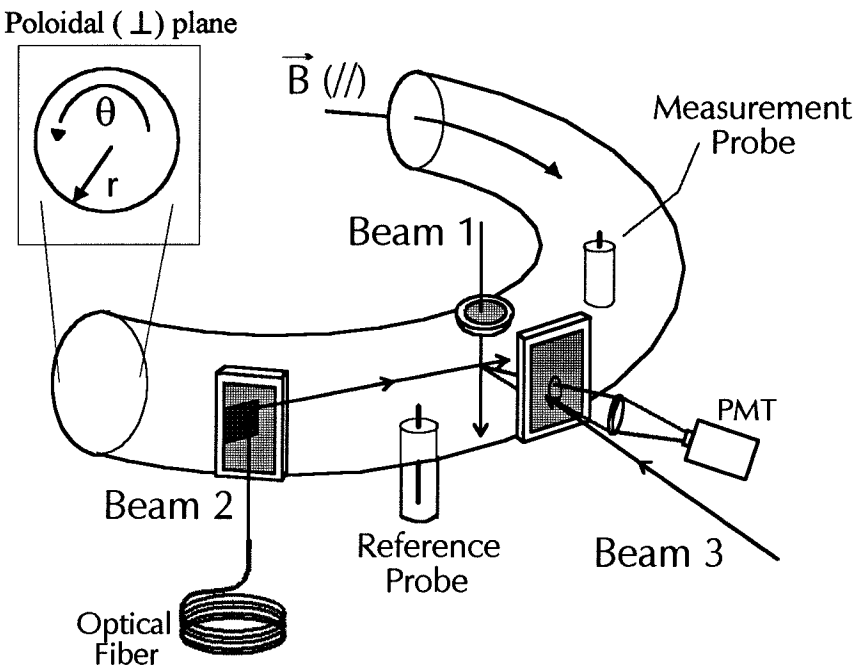

Figure 4.1: Schematic of experimental setup. The magnetic field direction is labeled $\parallel$. The poloidal and minor-radial directions, respectively labeled $\perp$ r and $\perp$ θ in the text, are shown in the inset. The "Reference" Langmuir probe provided phase reference (c.f. Ch. 3), and the "Measurement" probe determined density and plasma potential.

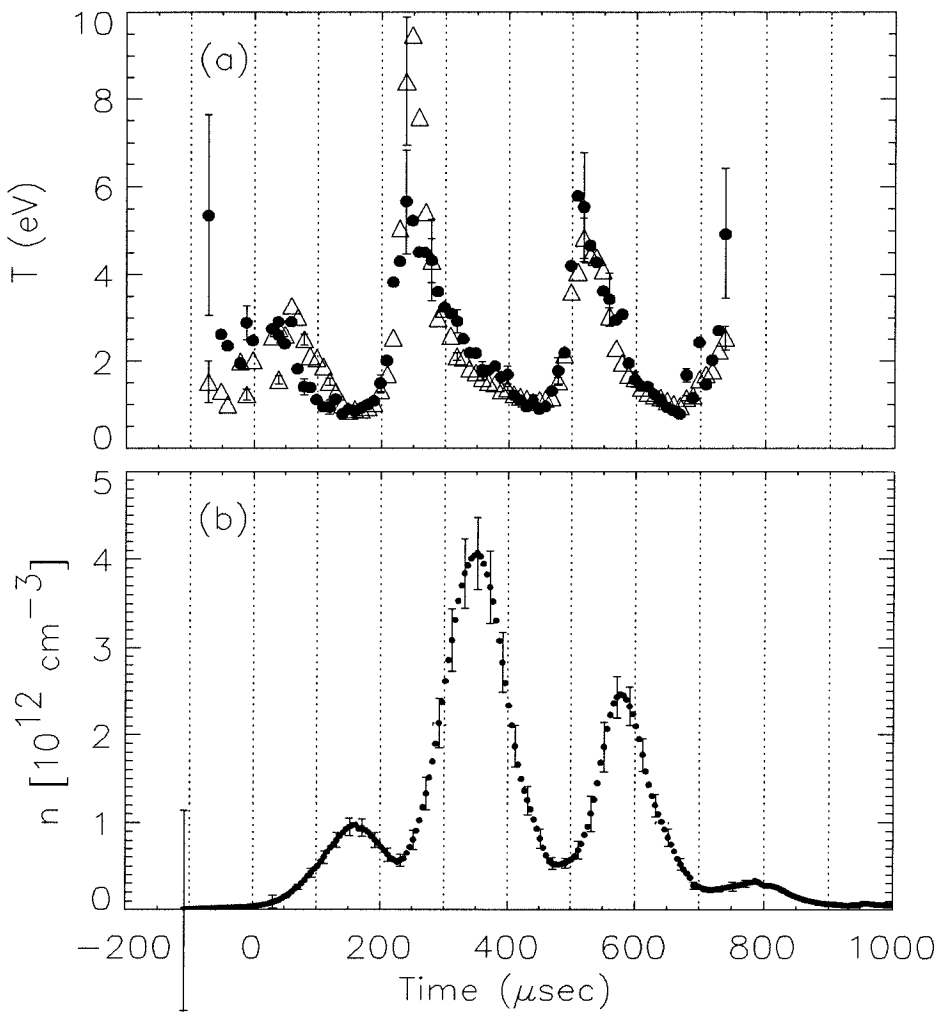

Figure 4.2: (a) LIF-measured ion temperatures: $T_{\perp\theta}$ ($\triangle$), $T_{\perp r}$ ($\bullet$). (b) Ion density measured by Langmuir probe. The probe was located 18° toroidally downstream from the LIF location, and probe data were adjusted to account for the wave phase delay in traversing this distance.

faster than can be explained by classical mechanisms, such as equilibration with the hot electron background or direct acceleration by the toroidal electric field.

Electrons are rapidly heated by the Ohmic heating field and therefore seemingly offer a rich supply of energy for ions. However, the collisional exchange of energy between electrons and the massive ions is slow. The ion-electron energy exchange time is given by [9] $\tau_{ie}^E = 3.1 \times 10^8 \mu T_e^{3/2}/n\Lambda_{ie}$, with μ the ion mass in AMU and Λ_{ie} is the Coulomb logarithm. Evaluating τ_{ie}^E for typical Encore parameters ($T_e \sim 7$ eV, $n \sim 2 \times 10^{12}$ cm^{-3}) we find $\tau_{ie} \gtrsim 2.1$ msec, or about 10 times the wave period. The ion heating rate due to collisions with hot electrons is then $\dot{T} = (T_e - T)/\tau_{ie}^E \lesssim 0.003$ eV/μsec, accounting for only 3% of the observed ion heating.

Direct ion acceleration by the OH electric field, followed by randomizing collisions with electrons, also can give ion heating. In a uniform electric field E, ions acquire a drift velocity $u_d = qE\tau_{ei}/m$. Collisions with electrons then thermalize the energy at the rate $\dot{T} \approx m_i u_d^2/2\tau_{ei} = q^2E^2\tau_{ei}/2m_i$. For the OH toroidal field in Encore, $E_\| \sim V_{loop}/2\pi R \approx 8$ V m^{-1}, this gives only $\dot{T} \leq 10^{-4}$ eV/μsec, a negligible heating rate. Thus the observed perpendicular ion heating cannot be explained by classical mechanisms.

4.2.2 Heating Parallel to B

Measurements of $T_\|$, the ion temperature *along* the magnetic field, are shown in Fig. 4.3. For comparison, $T_\perp = (T_{\perp r} + T_{\perp\theta})/2$ is also plotted, using the same $T_\perp$ data as in Fig. 4.2(a). $T_\|$ also heats rapidly, at a peak rate of $\dot{T}_\| \approx 0.035$ eV/μsec. While this rate is a factor of 3 lower than $\dot{T}_\perp$, it is still 10 times greater than can be explained by heating due to the hot electron background and 100 times greater than direct heating by the OH electric field, as shown above. Furthermore, recall that direct heating by the *wave* electric field should be confined to the $\perp$ plane, both because the wave is polarized with $k_\perp/k_\| \gg 1$ and because ion dynamics are not stochastic along **B**.

The parallel heating is believed due to inter-ion collisions relaxing the ion $\perp$-to-$\|$ temperature anisotropy. This deduction is supported by two prominent features seen

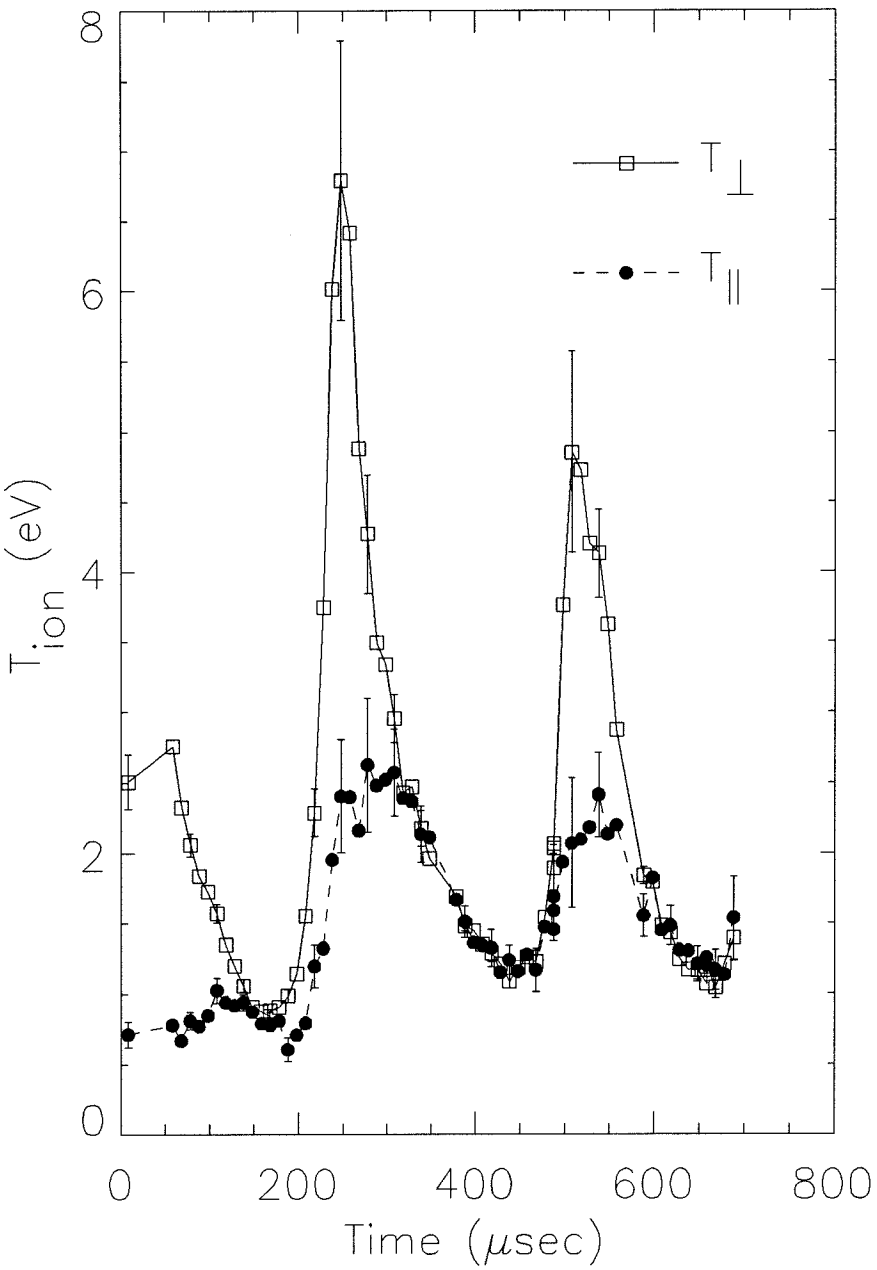

Figure 4.3: Measured ion temperatures $T_\perp(\square)$ and $T_\parallel(\bullet)$. The inferred peak heating rates are $\dot{T}_\perp \approx 0.1$ eV/μsec and $\dot{T}_\parallel \approx 0.03$ eV/μsec.

in Fig. 4.3: (i) The $T_\perp - T_\parallel$ anisotropy is most pronounced in the first 100 μsec of the discharge. This anisotropy is consistent with the low density and hence low ion-ion collision rate at these early times. For $n \lesssim 5 \times 10^{11}$ cm^{-3} the ion-ion collision time is $\tau_{ii} > 100$ μsec, and little collisonal transfer of energy $T_\perp \rightarrow T_\parallel$ can occur. Note that the large $T_\perp$ indicates that stochastic heating is strong at these early times, and it also contributes to the low collision rate, since $\tau_{ii} \sim T^{3/2}$. (ii) Although the parallel heating is coherent with the perpendicular heating, there is a significant phase delay between the two. This delay contrasts sharply with the case of $T_{\perp r}$ and $T_{\perp\theta}$, which appear to heat simultaneously. Clearly the wave is not heating $T_\parallel$ directly, but rather wave energy is transferred to $T_\parallel$ after a delay suggestive of a collision time. An order-of-magnitude estimate using the mean discharge conditions $T = 3.5$ eV and $n = 2 \times 10^{12}$ cm^{-3} gives $\tau_{ii} \approx 100$ μsec, comparable to the wave period, indicating that collisions are significant.

We now develop a quantitative model for the evolution of $T_\parallel$. It is assumed that the parallel ion heating is described by

$$\dot{T}_\parallel(t) = \left(\dot{T}_\parallel\right)_C + \left(\dot{T}_\parallel\right)_L , \tag{4.1}$$

where the term labeled C represents collisional equipartition of energy between the three degrees of ion freedom, and the term labeled L represents heat loss due to transport of hot ions out of the plasma. The loss term is motivated by the observation that the ions *cool* periodically (c.f. Fig. 4.3). This parallel cooling cannot be explained by mere exchange of energy among the three degrees of ion freedom because, as the figure reveals, $T_\perp$ and $T_\parallel$ decrease simultaneously. Section 4.4 presents evidence that the cooling is caused by loss of confinement of hot ions. For the moment, we simply note that the loss term must be small compared to the collisional term *during the heating* phase of the wave, i.e., when $\dot{T}_\parallel > 0$; if it were not, then $T_\parallel$ could not rise so rapidly during the heating cycle. Thus we neglect the loss term and assume that the parallel *heating* is attributable to collisions only:

$$\dot{T}_{\parallel}(t) \simeq \left(\dot{T}_{\parallel}\right)_C . \tag{4.2}$$

This equation is understood to hold only when $\dot{T}_{\parallel} > 0$.

It was initially hoped that the time delay between the perpendicular and parallel heating cycles would yield a direct measurement of τ_{ii}. An attempt was made to fit the observed $T_{\parallel}$ heating to the equation $\dot{T}_{\parallel}(t) = \left(T_{\perp} - T_{\parallel}\right)/\tau_{ii}$, where τ_{ii} was a time-independent fitting parameter. That this attempt failed is not surprising because the ion density and temperature fluctuate strongly with the wave, and $\tau_{ii} \sim T^{3/2}/n$. A self-consistent treatment which accounts for the dependence of τ_{ii} on T and n, follows.

4.3 Collisions and Fokker-Planck Theory

Collisions in a fully ionized plasma are described by Fokker-Planck (FP) theory [10], which assumes that particle transport is governed by the cumulative effect of numerous glancing collisions. This assumption is generally considered valid in a plasma, where the Coulomb potential is shielded at distances greater than the microscopic Debye length λ_D. The cumulative effect of small-angle scattering is more important than individual binary collisions by the factor $\nu_m/\nu_1 \approx 8\Lambda$. Here ν_m is the rate at which an r.m.s. scattering angle of 90° accumulates through many glancing collisions, and ν_1 the frequency of 90° scatterings in single binary-Coulomb events. For most plasmas, including Encore, the Coulomb $\Lambda \sim \mathcal{O}(10)$, and the condition $\nu_m/\nu_1 \gg 1$ holds. Note that the use of unmagnetized transport theory is justified when the ratio of ion Larmour radius to Debye length is large [11]. In Encore, $r_{Li}/\lambda_{Di} \approx 4000$ and the unmagnetized theory may be applied.

The Landau form [12] of the Fokker-Planck transport equation is

$$\left(\frac{\partial f^a(\mathbf{v},t)}{\partial t}\right)_C = \Gamma \frac{\partial}{\partial v_j} \int d^3\mathbf{v}' \frac{u^2\delta_{jk} - u_j u_{jk}}{u^3} \left(\frac{\partial f^a(\mathbf{v})}{\partial v_k}\frac{f^b(\mathbf{v}')}{m_a} - \frac{\partial f^b(\mathbf{v}')}{\partial v'_k}\frac{f^a(\mathbf{v})}{m_b}\right), \tag{4.3}$$

where $\Gamma = 2\pi\Lambda_{ab}e_a^2e_b^2/m_a^2$, $\mathbf{u} = \mathbf{v} - \mathbf{v}'$, and the subscripts j and k run over the Cartesian coordinates x, y, z. This equation describes evolution of the distribution function of test particles a due to collisions with background particles b. Here we are interested in ion-ion collisions, $a = b = i$, and we omit the species label for clarity.

Kogan first used Eq. 4.3 to study the relaxation of plasma temperature anisotropies [13]. Following Kogan, we multiply Eq. 4.3 by $mv_\parallel^2/2$ and integrate with respect to $\mathbf{v}$ to obtain an equation for the evolution of the parallel ion temperature:

$$\left(\int d^3\mathbf{v}\frac{\partial f(\mathbf{v})}{\partial t}\frac{mv_\parallel^2}{2}\right)_C = \frac{\Gamma}{2}\int d^3\mathbf{v}\, v_\parallel^2 \int d^3\mathbf{v}'\frac{u^2\delta_{jk} - u_ju_{jk}}{u^3}\left(\frac{\partial f(\mathbf{v})}{\partial v_k}f(\mathbf{v}) - \frac{\partial f(\mathbf{v}')}{\partial v_k'}f^a(\mathbf{v})\right),$$

where the left-hand side is the time derivative of temperature,

$$\dot{T}_\parallel = \frac{\partial}{\partial t}\left[\frac{m}{2}\int d^3\mathbf{v}\, v_\parallel^2 f(\mathbf{v})\right].$$

The right-hand integral may be evaluated for the anisotropic Maxwellian distribution,

$$f(\mathbf{v}) = \left(\frac{m}{8\pi\kappa_B}\right)^{3/2}\frac{n}{T_\perp T_\parallel^{1/2}}\exp -\frac{m}{2\kappa_B}\left[\frac{\mathbf{v}_\perp^2}{T_\perp} + \frac{v_\parallel^2}{T_\parallel}\right]. \tag{4.4}$$

The integration is tedious but straightforward and is not given here. The result is

$$\left(\dot{T}_\parallel\right)_C = \frac{T_\perp - T_\parallel}{\tau_{ii}^E(t)}, \text{ where} \tag{4.5}$$

$$\tau_{ii}^E \equiv \frac{4m^{1/2}\epsilon_0^2(\pi\kappa_B T_\parallel)^{3/2}}{e^4 n\Lambda_{ii}}\left[\frac{A^2}{-3 + A^{-1/2}(A+3)\tan^{-1}(A^{1/2})}\right], \tag{4.6}$$

and $A \equiv T_\perp/T_\parallel - 1$ is a measure of the temperature anisotropy, assumed to be positive. For $A < 0$, the term $A^{-1/2}\tan^{-1}(A^{1/2})$ must be replaced by $(-A)^{-1/2}\tanh^{-1}(-A)^{1/2}$. In the limit $A \to 0$, the term in brackets evaluates to 15/4, and the energy exchange period reduces to $\tau_{ii}^E = 4/5$ of the classical Spitzer period.

Anisotropic temperature relaxations (ATR) have been observed in pure electron plasmas by Hyatt, Driscoll, and Malmberg [14], and in the strongly magnetized regime by Beck, Fajans, and Malmberg [15]. ATR have also been observed in a pure Magnesium ion plasma with $\lambda_D > r_L$ [16]. All of those experiments were conducted in quiescent, Penning-trapped plasmas with densities below 10^9 cm^{-3}. ('Quiescent' plasmas refer to plasmas containing little or no wave activity. Fluctuations of less than 5% were reported in Refs. [14]-[16].)

Most plasmas of interest, however, are not quiescent, and the equipartitioning of anisotropic particle energy in plasmas with significant wave activity has not previously been examined. We now compare the Fokker Planck predictions with our ion heating data, measured when the drift wave amplitude was far above the threshold for stochastic heating.

It is instructive to begin by plotting τ_{ii}^E, calculated from Eq. 4.6 using the measured n, $T_\perp$, and $T_\parallel$. Figure 4.4 displays τ_{ii}^E normalized to the drift wave period τ_{wave}. One sees that the collision period fluctuates strongly in time, resulting from the nearly 180° phase shift between local ion density and temperature (c.f. Fig. 4.2). The amplitude of these fluctuations clearly demonstrates that the wave is strongly perturbing the underlying kinetic properties of the plasma: the wave transforms the plasma from essentially *collisionless* ($\tau_{ii}^E \gtrsim \tau_{wave}$) to *highly collisional* ($\tau_{ii}^E \ll \tau_{wave}$) on time scales smaller than a wave period. To this author's knowledge, such oscillations in collisionality have not been previously observed.

Next, Eqs. 4.5 and 4.6 are combined to yield a single equation for the evolution of $T_\parallel(t)$. This equation is solved numerically using the measured $T_\perp(t)$ and $n(t)$ shown in Fig. 4.2 as inputs. Figure 4.5 shows the result of the calculation for three wave heating cycles. The Fokker Planck prediction for $T_\parallel$ is plotted as the solid curve in each heating cycle. The dashed curves indicate the prediction's uncertainty, owing primarily to the shot-to-shot fluctuations in the drift wave phase. The circles are the measured data. Overall, the amplitude and phase of the predicted $T_\parallel(t)$ agree well with the data[1], indicating that the dominant mechanism driving the $\perp \rightarrow \parallel$ energy

[1]The relatively poor agreement between theory and experiment in the first heating cycle ($t \leq 100$

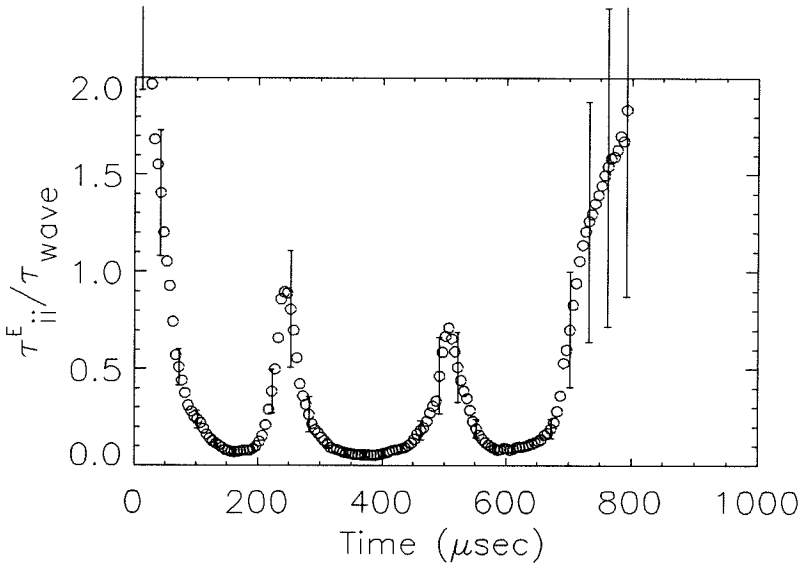

Figure 4.4: Ion-ion collision period, according to Eq. 4.6. τ_{ii}^E is normalized to the wave period $\tau_{wave} \approx 230$ μsec.

transport is indeed Fokker-Planck-type collisions. For comparison, Fig. 4.5 also shows a calculation of $T_\parallel(t)$ obtained from the time-averaged value of τ_{ii}^E (dotted curves). Here the agreement is markedly worse, underscoring that the instantaneous character of τ_{ii}^E must be taken into account.

4.4 Ion Cooling

A glance at Fig. 4.3 reveals that the ions *cool* periodically. For example, in the time range $t = 250 \rightarrow 400$ μsec, the ions lose energy at a rate of $\dot{T} \simeq -0.035$ eV/μsec. This cooling cannot be due to ions returning energy to the drift wave, since stochastic heating is true irreversible heating [18]. Nor can collisions with electrons explain the cooling rate: as noted in Section 4.2, the exchange of energy between ions and electrons is a factor of 10 too slow, and moreover, the electrons are relatively hot. Collisions with cold neutrals can cool ions, but the density of neutrals, assuming only

usec) probably results from overestimation of ion density by the Langmuir probe: Analysis of the probe data using the method of Laframboise [17] indicates that $n(t \leq 100$ μsec) is overestimated by about 20% relative to $n(t \gtrsim 100$ μsec).

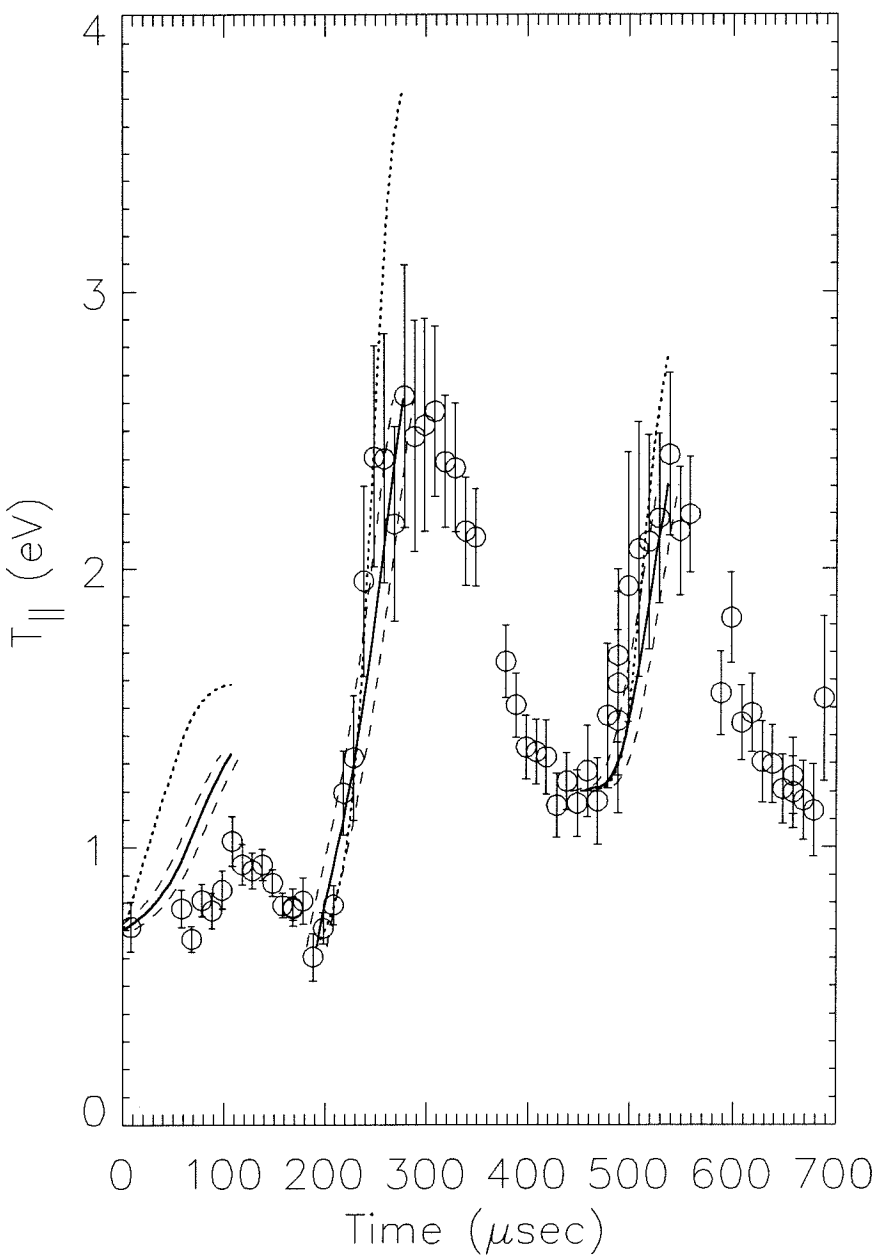

Figure 4.5: $T_{\|}$: Fokker-Planck prediction (solid curve), measured data (circles), and prediction using average collision time (dotted curve). Dashed curves show FP prediction uncertainty due primarily to wave phase jitter.

90% ionization, is at least two orders of magnitude too low to explain the observed cooling rate. Finally, radiation cannot directly sap ion kinetic energy.

Transport of energetic ions out of the plasma can produce ion cooling. Ions which reach the cold chamber wall are expected to recombine and eventually recycle as cold atoms [19]. This would cause simultaneous cooling along all three velocity dimensions, in agreement with the data. Assuming that an ion loses all its kinetic energy upon striking the wall, the ion cooling rate can be estimated by integrating over trajectories which reach the wall. Such a calculation is difficult for conditions in Encore, where the stochastic orbits cannot be represented analytically. However, lower and upper bounds for the loss rate can be predicted by considering orbits in the two limiting cases below:

(1) The classical limit of non-stochastic, magnetized orbits. In this case ion motion consists of rapid cyclotron motion about the magnetic field lines, together with steady drift along magnetic field lines. The extent to which an ion can stray from a particular field line is just the cyclotron radius $r = mv_\perp/qB$, where $v_\perp$ is the thermal velocity orthogonal to $\mathbf{B}$. For motion in a tokamak, the situation is complicated by the field curvature, gradient, etc. In this case, the classical distance an ion can stray from a field line turns out to be determined by the relatively weak poloidal (θ) component of the magnetic field, rather than the strong toroidal component. An upper bound for this distance is $r_\theta = mv_\parallel/qB_\theta$ [20], where $v_\parallel$ is the ion velocity in the toroidal direction. Thus, ions within a distance $d \lesssim r_\theta$ of the wall have reasonable probability of escaping confinement. The velocity condition for escape is then $v_\parallel \gtrsim \Omega_\theta d$, where $\Omega_\theta = qB_\theta/m$. The rate at which these ions carry energy to the wall is obtained by integrating over the velocity distribution $f(\mathbf{v})$:

$$\left(\dot{T}\right)_L \approx \frac{\Omega_\theta}{2\pi} \int_{|v_\parallel|>\Omega_\theta d} \frac{m\mathbf{v}^2}{2} f(\mathbf{v})\, d^3\mathbf{v}, \tag{4.7}$$

where it is assumed that the time for all ions to escape is roughly the Larmour gyration period $2\pi/\Omega_\theta$. For $f(\mathbf{v})$ an anisotropic Maxwellian (c.f. Eq. 4.4), the integral evaluates to

$$\left(\dot{T}\right)_L = \frac{\Omega_\theta}{2\pi}\left\{T_\parallel\left[\frac{2}{\pi^{1/2}}ae^{-a^2} + erfc(a)\right] + T_\perp erfc(a)\right\}, \tag{4.8}$$

where $a = \Omega_\theta d/(2\kappa_B T_\parallel/m)^{1/2}$ and $erfc(\ )$ is the complimentary error function. Equation 4.8 is an expression for the ion power transfer to the wall. For Encore parameters ($B_\theta = 30$ Gauss, $d = 4$ cm), Eq. 4.8 predicts a peak heat loss rate of $\dot{T} \approx -0.007$ eV/μsec, about a factor of 5 lower than what is observed.

(2) The strongly stochastic limit, in which the wave electric force dominates over magnetic forces. In this limit the ions are treated as having straight-line orbits toward the wall. This model is unrealistic, of course, but gives an absoluteupper bound on the cooling rate due to stochastic orbits. An ion reaches the wall in time t if $v_{wall} \geq d/t$ where v_{wall} is the velocity toward the wall and d is again the ion's distance from the wall. Assuming all the ions are initially located together and integrating over a Maxwellian yields a predicted peak loss rate of $\dot{T} \approx -0.15$ eV/μsec, about a factor 5 higher than the cooling rate observed.

Thus the measured cooling rate lies between the classical and the strongly stochastic limits for heat loss due to ion transport. Moreover, measurements show that the cooling is strongest near the chamber wall, as would be expected for cooling by ion loss. Figure 4.6 plots the measured ion temperatures at several locations in the plasma.

One sees that both the heating and cooling are much more extreme near the plasma edge, $r/a \rightarrow 1$. For example, near the center of the machine ($r/a = 0.24$), T_i rises in the first 100 μsec to a 'pedestal' value of about 1.8 eV and executes small oscillations ($\sim$ 30%) about this pedestal. However, near the plasma edge, where the heating is clearly stronger, T_i oscillates from a peak of nearly 10 eV to *below 1 eV*, significantly colder than at the plasma center. Ion heating is strongest at the edge because the density gradient, and hence drift wave amplitude, are peaked there; that the *cooling* is strongest near the edge suggests particle loss. The loss argument is further corroborated by the spatial dependence of the ion density fluctuations. Figure 4.7 compares the amplitude of density fluctuations seen at varying minor

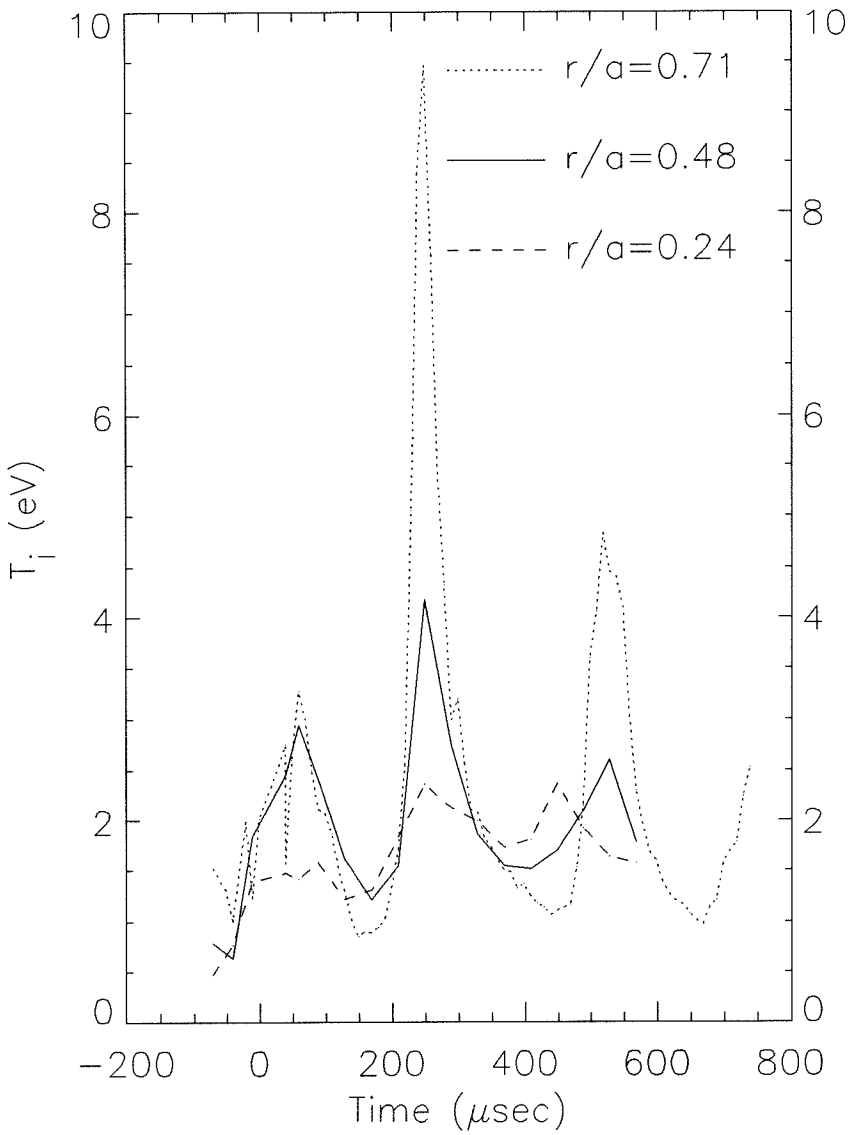

Figure 4.6: Variation of ion temperature T with minor radius. Radii are normalized to the machine radius $a = 13$ cm. Near the machine center ($r/a = .24$), T executes small oscillations ($\sim$ 30%) about a pedestal of 1.8 eV. Near the edge, T oscillates from above 5 eV to below 1 eV each cycle.

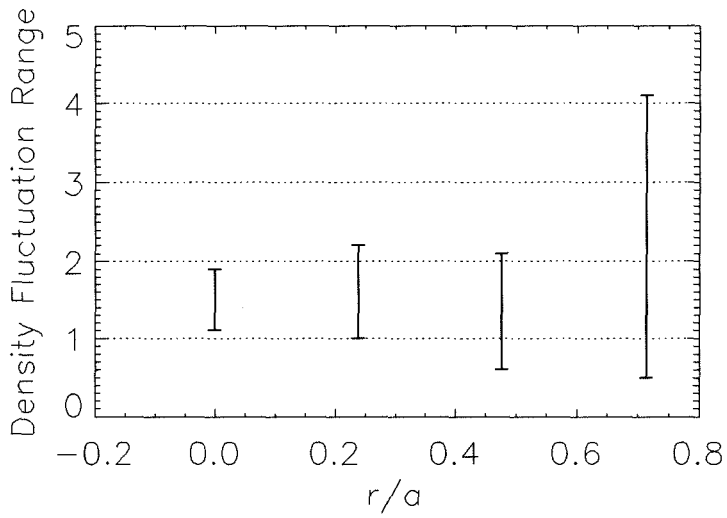

Figure 4.7: Ion density fluctuation range, as a function of minor radius. The bars extend from the 'pedestal' density (lower end) to peak instantaneous density (upper end).

radii. Again it is apparent that at the center the density fluctuations are only 25% of the equilibrium $\langle n \rangle = 1.5 \times 10^{12} cm^{-3}$, whereas near the edge the density alternately soars far above (4×10^{12}) and far below (0.5×10^{12}) this equilibrium value. Thus, ion cooling by orbit loss is consistent with both the measured cooling rate and the observed spatial dependence of the temperature and density fluctuations.

4.5 Summary and Concluding Thoughts

Several new aspects of stochastic ion heating by drift waves have been observed for the first time. Strong temperature oscillations near the plasma edge enabled detailed examination of the means by which energy is distributed among three degrees of ion freedom. The stochasticity was shown explicitly to heat ions isotropically in the plane normal to B, while ion-ion collisions were shown to be responsible for heating ions along B.The rate at which the ion temperature anisotropy relaxed agreed well with Fokker Planck theory, with one unexpected caveat: that the ion-ion collision period

fluctuated severely with the wave, transforming the plasma from weakly collisional to highly collisional during each wave cycle. Thus the instantaneous character of the collision rate must be emphasized when considering wave heating.

Some comments about the general applicability of this result are in order. First, consider the ion adiabatic equation of state $PV^\gamma = const$, where P is the ion kinetic pressure, T is of course the ion temperature, and γ is the ratio of specific heat at constant pressure to that at constant volume. As is well-known, γ is related to the dimensionality D of the system by $\gamma = 1 + 2/D$. In terms of T and density n, the state equation is $Tn^{1-\gamma} = const$. For a three-dimensional system ($D = 3$) this gives $Tn^{-2/3} = const$, or

$$T^{3/2}/n = const. \tag{4.9}$$

This conserved quantity has almost exactly the same dependence on T and n as does the ion-ion collision period τ_{ii} for isotropic ions (c.f. Eq. 4.6 with $A = 0$); the dependence of τ_{ii} on n and T through Λ is logarithmic and therefore very weak by comparison. This functional similarity appears to be a mathematical coincidence, since for τ_{ii} the $T^{3/2}$ arises through the v^{-4} fall-off in the Coulomb scattering cross section, whereas the state equation is derived assuming an ideal non-interacting gas. Nevertheless, this functional similarity carries the following implication: Any plasma process which is non-adiabatic, i.e. does not satisfy Eq. 4.9, *must* have a fluctuating collision rate. In such cases the oft-used assumptions about plasma collisionality – that a process is either highly collisional or ideally collisionless – must be questioned.

Second, the importance of ion losses in the heating and cooling process might lead one to wonder whether the phenomena observed here are unique to Encore: after all, each plasma device is unique and therefore particle orbits and losses might vary significantly from machine to machine. To answer this question, consider the maximum ion velocities attainable in stochastically heated plasmas. McChesney *et al.* give the following expression for this maximum velocity [8]

$$\frac{v_{\max}}{\Omega/k_\perp} \simeq \alpha + 2.3.$$

Here as usual Ω_i is the ion cyclotron frequency, $k_\perp$ is the wave number perpendicular to $\mathbf{B}$, and $\alpha = m_i k_\perp^2 \tilde{\phi}/qB^2$ is the normalized wave amplitude. The work of Drake and Lee shows a similar scaling law [18]. It must be emphasized that $v_{\max}$ is the half-width of the stochastic region of phase space (c.f. Poincaré plots of Chapter 2) and therefore this high velocity is accessible to ions in the bulk of the distribution. As noted in section 4.4, ions are well-confined by the magnetic field only if their separation d from the wall satisfies $d \gtrsim v/\Omega$. Inserting $v \approx v_{\max}$ into this expression yields $d \gtrsim (\alpha + 2.3)/k_\perp$. Finally, noting that $k_\perp = m_\perp/a$ where $m_\perp$ is the wave perpendicular mode number and a is the machine minor radius, yields the confinement criterion

$$\frac{d}{a} \gtrsim \frac{\alpha + 2.3}{m_\perp}. \tag{4.10}$$

For an $m_\perp = 2$ mode, for example, the condition for confining stochastically heated ions is then $d/a \gtrsim \alpha/2 + 1$. This indicates that ions must be located more than one machine radius away from the wall to be reasonably well confined at the onset ($\alpha \approx 1$) of stochasticity! The confinement criterion 4.10 cannot be satisfied by any mode with $m_\perp \lesssim 4$, implying that strong ion losses similar to those in Encore would be expected in any machine with low mode-number waves and stochastic dynamics.

Chapter 5 continues the discussion of ion behavior in the drift waves, focusing on the fate of ions which are lost to the wall.

Bibliography

[1] F. Doveil, "Stochastic plasma heating by a large-amplitude standing wave," *Phys. Rev. Lett.*, **46**, 532 (1981).

[2] F. Skiff, F. Anderegg, and M.Q. Tran, "Stochastic particle acceleration in an electrostatic wave," *Phys. Rev. Lett.*, **58**, 1430 (1987).

[3] F. Skiff *et al.*, "Conservation laws and transport in Hamiltonian chaos," *Phys. Rev. Lett.*, **61**, 2034 (1988).

[4] A. Fasoli *et al.*, "Dynamical chaos of plasma ions in electrostatic waves," *Phys. Rev. Lett.*, **70**, 303 (1993).

[5] J.M. McChesney, R.A. Stern, and P.M. Bellan, "Observations of fast stochastic ion heating by drift waves," *Phys. Rev. Lett.*, **59**, 1436 (1987).

[6] A.D. Bailey III, R.A. Stern, and P.M. Bellan, "Measurement of coherent drift-wave ion-fluid velocity field when ion dynamics are stochastic," *Phys. Rev. Lett.*, **71**, 3123 (1993).

[7] L. Spitzer Jr., *Physics of Fully Ionized Gases*, (John Wiley and Sons, New York, 1962).

[8] J.M. McChesney, P.M. Bellan, and R.A. Stern "Observation of fast stochastic ion heating by drift waves," *Phys. Fluids B* **3**, 3370 (1991).

[9] J.D. Huba, *NRL Plasma Formulary*, (NRL Publication 6790–94-265, Washington, DC, 1994), pp. 33-34.

[10] See, for example, T.J.M. Boyd and J.J. Sanderson, *Plasma Dynamics*, (Barnes and Noble, New York, 1969).

[11] D. Montgomery, L. Turner, and G. Joyce, "Fokker-Planck equation for a plasma in a magnetic field," Phys. Fluids **17**, 954 (1974).

[12] L.D. Landau, *Physik. Z. Sowjetunion* **10**, 154 (1936).

[13] V.I. Kogan, "The rate of equalization of the temperatures of charged particles in a plasma," in *Plasma Physics and the Problem of Controlled Thermonuclear Reactions Vol. 1*, edited by M.A. Leontovich (Pergamon Press, New York, 1961).

[14] A.W. Hyatt, C. F. Driscoll, and J. H. Malmberg, "Measurement of anisotropic temperature relaxation rate in a pure electron plasma," *Phys. Rev. Lett.* **59**, 2975 (1987).

[15] B. R. Beck, J. Fajans, and J. H. Malmberg, "Measurement of collisional anisotropic temperature relaxation in a strongly magnetized pure electron plasma," *Phys. Rev. Lett.* **68**, 317 (1992).

[16] F. Anderegg *et al.,* "Test particle transport due to long range interactions," *Phys. Rev. Lett.,* **78**, 2128 (1997).

[17] J.G. LaFramboise, "Theory of spherical and cylindrical Langmuir probes in a collisionless, Maxwellian plasma at rest," *UTIAS Report 100* (1966).

[18] J.F. Drake and T.T. Lee, "Irreversibility and transport in the lower hybrid drift instability," *Phys. Fluids* **24**, 1115 (1981).

[19] J.N. Brooks, "Analysis of noble gas recycling at a fusion plasma divertor," *Phys. Plasmas* **3**, 2286 (1996).

[20] J.A. Wessen, *Tokamaks*, (Oxford University Press, Oxford, 1987) p. 75.

Chapter 5 Observations of Convective Ion Recycling

5.1 Introduction

In plasma physics, the term "recycling" refers to the return of particles to the central plasma after interaction with the confining chamber wall. Recycling has long been recognized as an important aspect of tokamak plasma dynamics. Although the details of the connection between bulk plasma dynamics and the plasma-wall interaction is not thoroughly understood, it is clear that interaction with the wall transforms hot plasma particles into cold ones, through equilibration or inelastic reflection, and possibly also generates cold impurities, for example, by sputtering. When these cold particles return to the plasma bulk, they perturb the local temperature and density. There is, for instance, considerable evidence that control of both majority-ion and impurity recycling is a key factor in shaping tokamak plasma density profiles to achieve high-confinement regimes of operation such as the so-called "H-mode." [1]-[3]

This chapter presents direct experimental observations of cold argon ion recycling in Encore. Emphasis is on the return of recycled particles to the central plasma, rather than on the wall-interaction itself. The LIF diagnostic allows detailed space- and time-resolved measurements of ion velocity distribution functions near the chamber wall: these show cyclic convection of cold particles from the wall toward the plasma bulk. The convecting ions have density comparable to that of the background plasma, indicating that recycling is a significant refuelling mechanism. Simultaneous with this influx of recycled particles, the background ion distribution accumulates a cold Maxwellian 'bump' corresponding to the recycled ions. The bump eventually relaxes into the background distribution, as ions are again stochastically heated and lost in the drift wave cycle. Section 5.2 presents the experimental evidence for ion re-

cycling. Section 5.3 discusses possible alternative mechanisms to explain the observed distribution functions. Section 5.4 summarizes and presents concluding thoughts.

5.2 Experimental Data

As noted in chapter 2, the LIF-measured ion velocity distributions $f(\mathbf{v})$ could usually be closely fitted by Maxwellian curves. Figure 5.1(a) shows a dramatic exception to this rule. The figure plots $f(v_\theta)$ measured 4 cm from the chamber wall at a time when the local density was at a minimum; for reference, this sampling time is indicated by the triangle in the density plot of Fig. 5.1(b). The distribution is clearly non-Maxwellian, with an anomalous concentration of ions near $v_\theta = 0$. For comparison, Fig. 5.1(c) shows the same component $f(v_\theta)$ measured at the same spatial location, but sampled when the drift wave density was at a maximum (c.f. part (d) of the figure for sampling time). The distribution in 5.1(c) has an excellent fit to a Maxwellian, in sharp contrast with the distribution in Fig. 5.1(a). The experimental procedure and apparatus used to measure these two distributions were identical in every regard except for the time at which the laser was triggered, proving that the observed non-Maxwellian features cannot be artifacts of the measurement technique.

Such non-Maxwellian ion distributions were found only within about 4-5 cm of the chamber wall. Moreover, they were found to occur regularly and only at the drift wave phase of minimum ion density. This is illustrated in Fig. 5.2(a), which shows how the non-Maxwellian character of the LIF-measured velocity distributions depends on the drift wave phase. This non-Maxwellian character, labeled "Fit Dev." in the plot, is obtained by χ^2-fitting the measured $f(\mathbf{v})$ to a Maxwellian curve, calculating the average deviation between the fit and the data, and normalizing the deviation to the Maxwellian amplitude. This fit deviation thus represents the fraction of 'non-Maxwellian ions' in a given distribution. Figure 5.2(b) shows the ion density $n(t)$, measured at the same location. It is clear that non-Maxwellian distributions occur regularly at the wave phase of minimum density. Low ion density implies long ion-ion collision times (c.f. Section 4.4), and therefore at these wave phases one expects

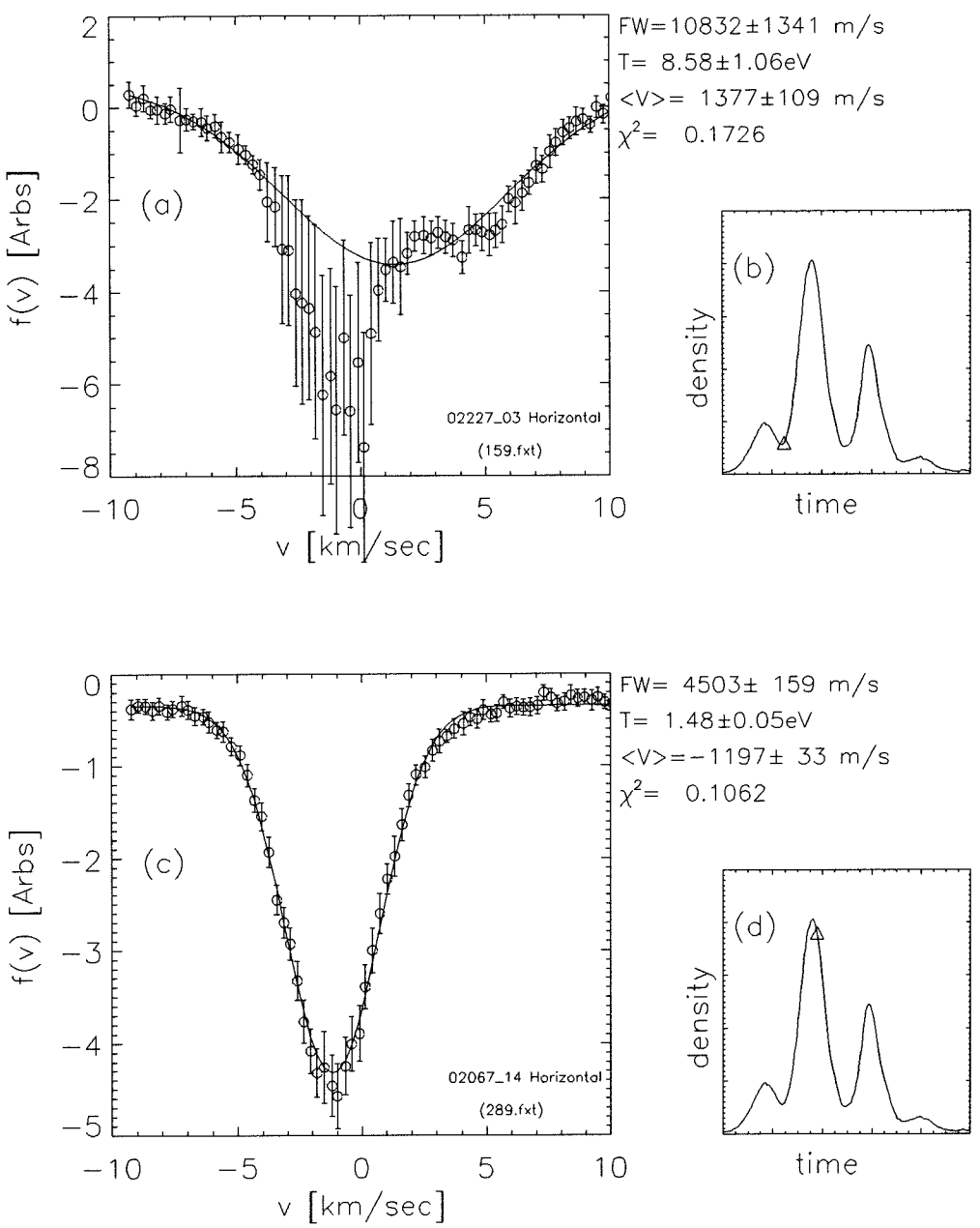

Figure 5.1: Shape of poloidal component of velocity distribution, $f(v_\theta)$, near plasma edge when (a) density was local minimum, and (c) density was local maximum. Solid curves show best-fit Maxwellians, and the fitted temperature T and flow velocity $\langle v \rangle$ are given. Measurement times (Δ) are shown at the right, in (b) and (d) respectively.

relatively slow relaxation of any non-Maxwellian features of $f(\mathbf{v})$. This argument implies that locally non-Maxwellian distribution functions can exist at these wave phases, but does not explain the *origin* of non-Maxwellian features.

Insight regarding this origin is given in Figure 5.2(c), which plots the time dependence of $u_r = \int v_r f(v_r)\, dv_r$, the ion fluid velocity along the minor radial direction (experimentally obtained from the Doppler shift in the ion LIF spectrum). These measurements were performed 4 cm from the chamber wall, with the laser oriented such that $u_r < 0$ indicates ion flow directed inward from the nearby wall, through the diagnosed volume, and toward the plasma center. (See Fig. 5.3 for a sketch of the geometry.) As can be seen, the phases having significant ion flux directed inward from the wall are followed closely ($\Delta t \approx 30 - 50$ μsec) by phases of non-Maxwellian distribution functions. The observed delay time of $\Delta t \approx 40$ μsec is consistent with the time required for an ion to traverse 4 cm at typical measured fluid velocities $u_r \approx -1$ km/sec. Thus the observed non-Maxwellian distributions correlate with an influx of ions from the edge. Bailey *et al.* showed that fluid motion in the Encore drift waves had the same flow pattern as predicted by $\mathbf{E} \times \mathbf{B}$ drift theory but that the measured fluid speed was about an order of magnitude lower than expected, the discrepancy being attributed to finite Larmour radius effects [4]. The measured u_r here is consistent with a similarly reduced $\mathbf{E} \times \mathbf{B}$ flow.

At this point, it is instructive to consider again the microscopic processes by which ions interact with the wall. Ions may, for example, recombine or undergo charge-exchange collisions; they may adsorb to or be absorbed by the wall; and they may reflect or sputter impurities and wall material. These microscopic processes are complicated but have been studied, and Refs. [1] and [5] give good reviews. The general result is that in most of these interactions, ions cool dramatically. In particular, adsorption and subsequent thermal desorption have been identified as a dominant recycling mechanism for argon [6]. Thus, ions recycling from the edge are expected to be very cold ($\sim 1/40$ eV), having cooled through equilibration with the chamber wall.

Noting that the distribution in Fig. 5.1(a) appears to be bimodal, we perform a

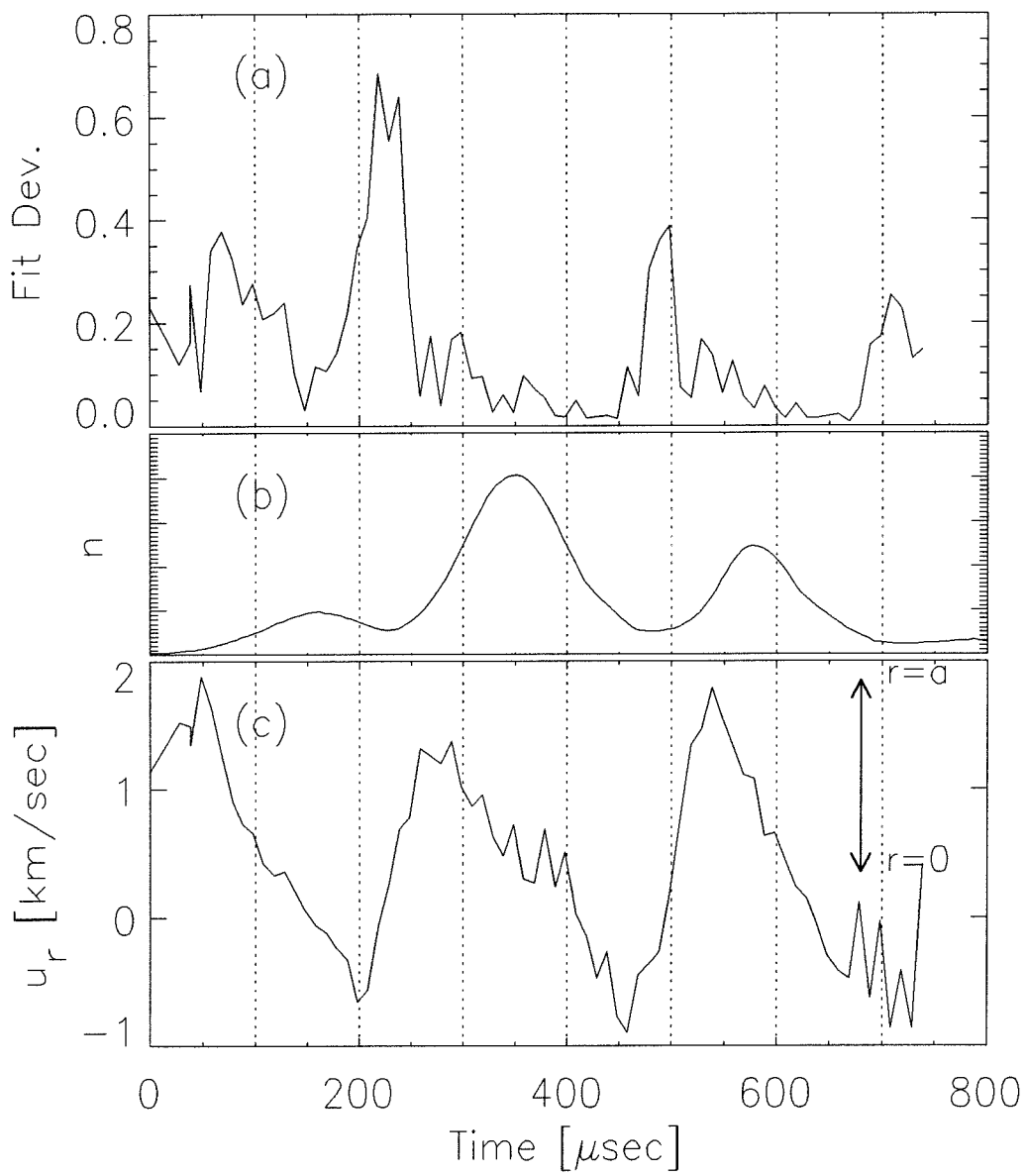

Figure 5.2: (a) Deviation of measured ion distribution functions from Maxwellian curves. (b) Density. (c) Ion fluid velocity u_r along minor radius. Positive velocities represent flow directed toward plasma edge ($r = a$). Density data were given in Chapter 4, and are reproduced here for phase comparison only.

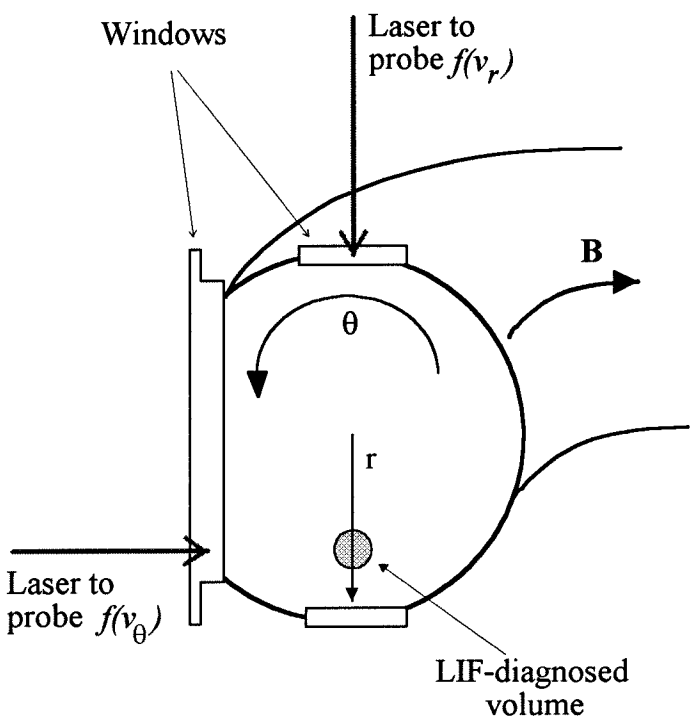

Figure 5.3: Geometry for recycling discussion. The LIF-diagnosed volume is located 4 cm from the plasma edge, at $r/a = 0.7$. The wave rotates in the $-\hat{\theta}$ direction.

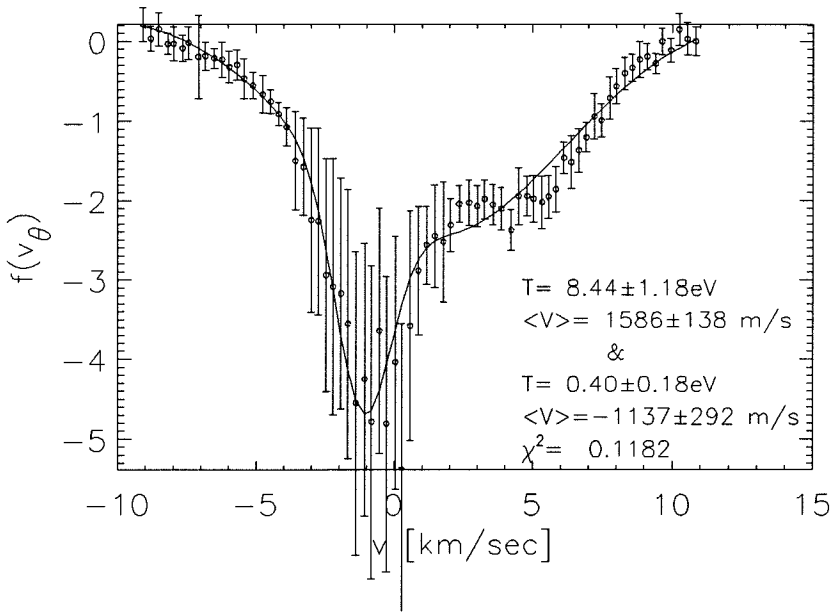

Figure 5.4: χ^2 fit of $f(v_\theta)$ to sum of two Maxwellians. Fitted temperatures are 8.4 and 0.4 eV, respectively.

χ^2-fit of $f(v_\theta)$ to the sum of two Mawellians with independent temperatures, amplitudes, and fluid velocities. The result of the fit is shown in Fig. 5.4. The fit is clearly much better than the single-Maxwellian fit shown in Fig. 5.1(a). The distribution apparently consists of a very cold (0.4 eV) plasma superposed atop a very hot (8.4 eV) one, as would be expected for recycling of cold particles. The fitting procedure also reveals the relative numbers of cold and hot ions. For this distribution, the recycled density was found to be roughly equal to the background density. This density ratio varied somewhat, from dataset to dataset, but was typically found to be in the range $n_{cold}/n_{hot} \approx 0.5 - 1.0$. Thus the cold ions account for a significant fraction of the total plasma density at $r/a = 0.7$.

Incidentally, the distribution in Fig. 5.1(a) provokes the question of what temperature *means* in the context of non-Maxwellian distributions. This question is answered by noting that the distribution in Fig. 5.1(a) is unquestionably hotter than that in Fig. 5.1(c), in the sense that it is much broader.

Brooks has modeled the plasma-wall interaction in the divertor region of the pro-

posed ITER tokamak [6], considering argon impurities impinging upon a beryllium wall in a very dense (10^{21} cm^{-3}) plasma. He found that impinging 7-eV argon ions recycle primarily by adsorption, followed by thermal desorption at 0.17 eV. Because the modeled plasma density is much higher than that in Encore, and because interaction with the aluminum wall of Encore may be very different than with Be, comparison with Brooks' results can be only qualitative. Nevertheless, the similarity between the recycled ion energies found in Brooks' model and in the present measurements is noteworthy. Thus the temperature of the inward-convecting ions is consistent with the energies expected for recycled particles.

Equilibration between the hot local plasma and the cold recycled ions would be expected to generate some local ion cooling. To check this expectation, the measured ion temperature T is plotted in Fig. 5.5(a). Comparison of $T(t)$ with the time dependence of the fit deviations, repeated in 5.5(b) for convenience, suggests that the onset of ion cooling correlates with the arrival of the non-Maxwellian ions: note, for example, the decrease in T starting at $t_{cool} \simeq 250\,\mu$sec and the prominent peak in the fit deviations at $t_{FD} \simeq 230$ μsec. The delay time $t_{cool} - t_{ci} \simeq 20$ μsec is roughly comparable to the time required for a cold beam to equilibrate with the background plasma. This occurs by a two-step process: the beam isotropizes on a fast time scale due to transverse diffusion in velocity space and equilibrates with the background plasma on a slower timescale. The transverse diffusion time is given by Trubnikov [7] and in the limit of a slow beam ($mv_{beam}^2/2 \ll T_{plasma}$) may be written approximately as

$$\tau_{ii}^{\perp} = 7.1 \times 10^6 \frac{\mu^{1/2} T_{bkg}^{1/2} \epsilon}{n \Lambda_{ii}}. \tag{5.1}$$

where μ is the ion mass in proton units, $\epsilon = mv_{beam}^2/2$ is the directed beam energy, T_{bkg} is the background plasma temperature, and energies are in eV. Assuming roughly equal beam and background plasma densities [c.f. Fig. 5.2], we estimate, at the time of peak cold ion flux ($T_{bkg} = 1.5$ eV, $n_{bkg} = 0.4 \times 10^{12}$ cm^{-3}, $v_{beam} = 0.8$ km/sec, $\Lambda_{ii} \approx 7$), $\tau_{ii}^{\perp} \approx 3$ μ sec. The temperature equilibration between the resulting cold

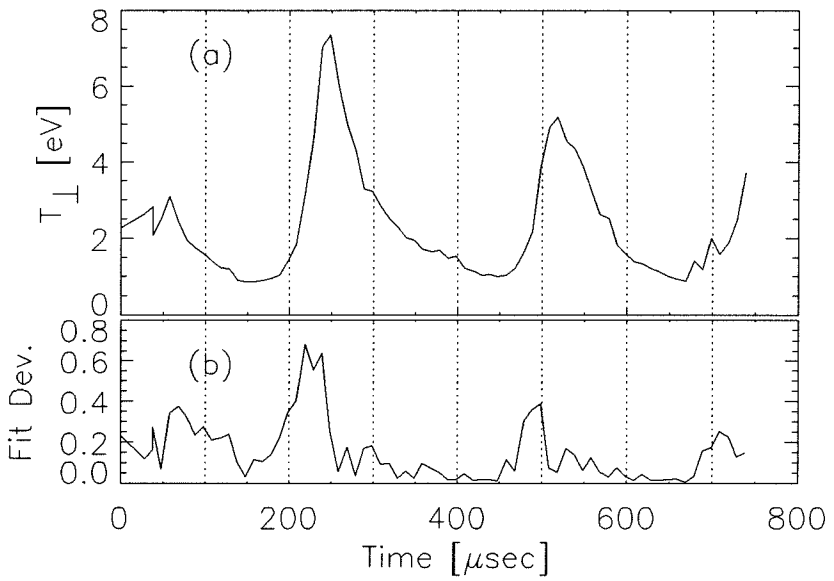

Figure 5.5: (a) $T_\perp(t)$ and (b) non-Maxwellian character of $f(v_\theta)$. Both curves pertain to plasma 4 cm from the chamber wall.

Maxwellized beam and the hot background plasma occurs on a timescale [3]

$$\begin{aligned} \tau_{ii}^{T} &= 2.5 \times 10^{6} \frac{\mu^{1/2}}{n\Lambda_{ii}} (T_{cold} + T_{bkg})^{3/2} \\ &\approx 14\ \mu\text{sec}. \end{aligned}$$

Hence $\tau \approx \tau_{ii}^{\perp} + \tau_{ii}^{T} \approx 17\ \mu$sec is the predicted beam-plasma equilibration time.

The equilibration between the hot and cold ion components can be seen directly in the time evolution of the distribution function. Figure 5.6 shows the evolution of $f(v_\theta, t)$ over a 200-μsecond time interval centered on a density minimum. Each frame is a snapshot of $f(v_\theta, t)$ at fixed time t. The frames are 10 μsec apart, and the instantaneous temperature inferred from the best-fit (single) Maxwellian is given in the lower right corner of each frame. For reference, the wave phases corresponding to these sampling times are shown by the discrete diamonds on the fluid velocity plot of Fig. 5.7. As can be seen, the distribution begins to show significantly non-

Maxwellian features in frame (d), when the fluid velocity directed inward from the wall is $u_r \approx -400$ m/s; this time corresponds to the arrival of the first cold ions. The cold ion population evidently builds over the next 30-40 μsec, as the inward fluid velocity peaks around $u_r \approx -800$ m/s and begins to reverse. The cold prominence on $f(v_\theta)$ then remains visible for the next several frames, relaxing finally by about frame (m). The non-Maxwellian features visible in frames (n) and (o) are clearly much more subtle than those in, e.g., frame (g) and are probably insignificant in light of experimental uncertainties. One other interesting feature of Fig. 5.6 is that the background temperature continues to rise in spite of the arrival of cold ions: in frames (e)-(j) the temperature rises from 1.3 to 9.4 eV although the presence of cold recycled ions is clear. This again reflects the low ion collision rate, which is in fact *decreasing* during the heating cycle, and also indicates that the stochastic heating is fast enough to overcome the cooling due to recycled ions. The final equilibration of the cold ions with the background plasma is no doubt influenced by stochastic heating, ion orbit loss, edge recycling, and collisions. The self-consistent interplay between all of these mechanisms is very complicated and no quantitative analysis is given here.

Finally, the spatial dependence of the non-Maxwellian distributions was determined by repeating the LIF measurements to obtain $f(v_\theta)$ over a range of distances from the chamber wall. At each position, the time evolution of $f(\mathbf{v})$ was sampled in 40 μsec intervals, and the fit deviation was computed for the most non-Maxwellian distributions seen. The relative deviations are compared by position in Fig. 5.8. The figure shows that strongly non-Maxwellian distributions were found only near the plasma edge: the relative population of cold ions decreases by about an order of magnitude with every 3 centimeters of retreat from the wall. Such localization would be expected for phenomena involving recycling, because recycled ions which penetrate the plasma core would be expected to heat stochastically in transit and arrive finally as hot ions indistinguishable from the hot background plasma. Measurements in the region nearer to the plasma edge, i.e., $r/a \geq 0.7$, probably would have shed considerable additional light on the recycling processes. Regrettably, however, optical access for the LIF was limited to $r/a \leq 0.7$.

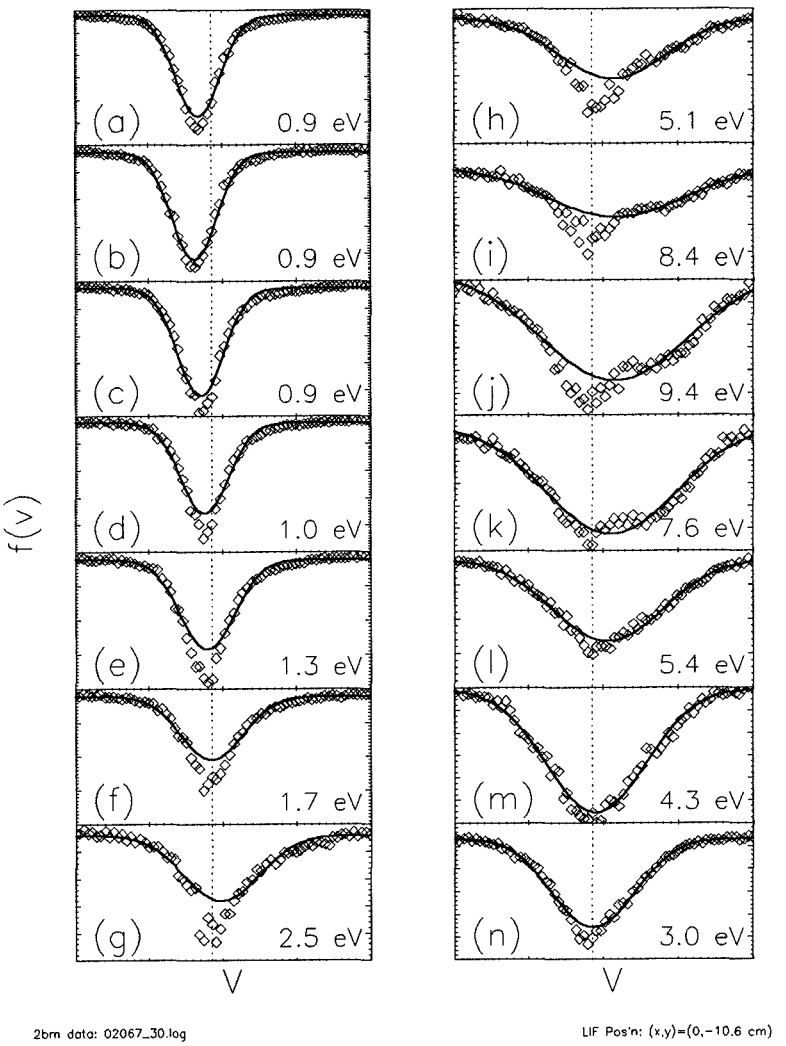

Figure 5.6: Time evolution of non-Maxwellian ion distributions. Time interval is 10 μsec per frame, advancing first down the left column (a-g), then down the right column (h-n), and continuing on the next page. Discrete points are data, and solid curves are best-fit single Maxwellians. The dashed vertical lines indicate $v = 0$.

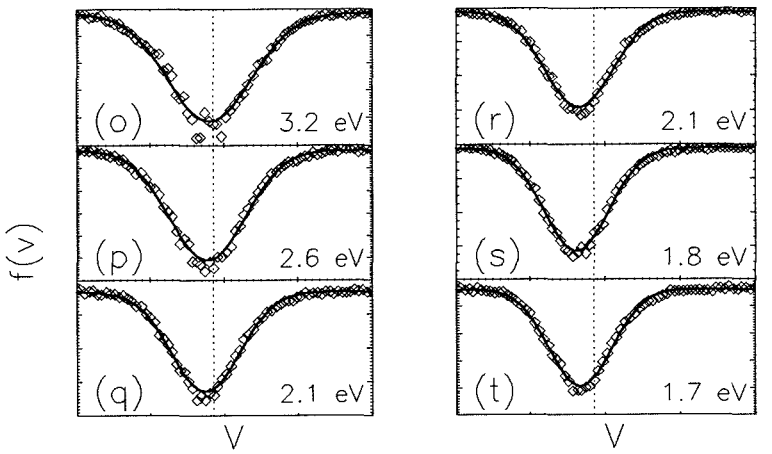

Figure 5.6: (continued)

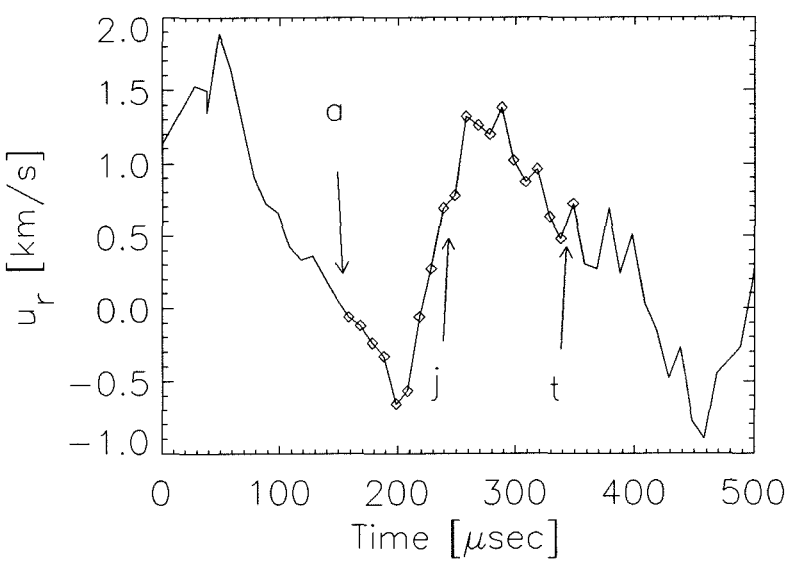

Figure 5.7: Plot of measured radial fluid velocity u_r near density minimum. The discrete points indicate the sampling times for data shown Fig. 5.6. $u_r < 0$ indicates flow from wall to center.

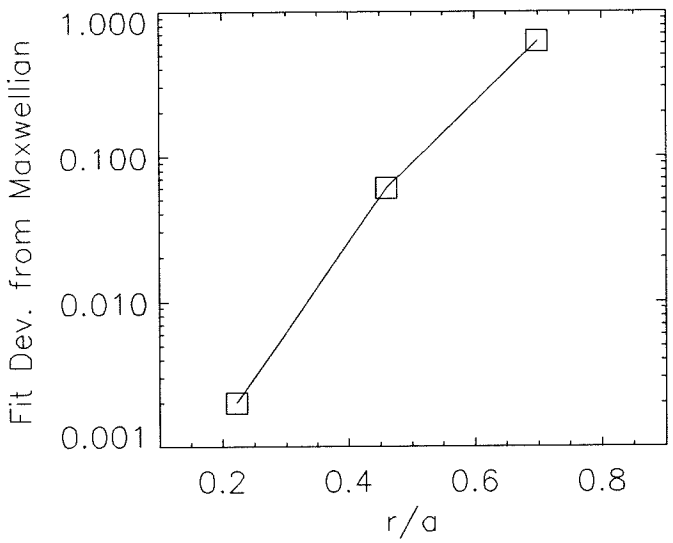

Figure 5.8: Deviation of measured $f(v)$ from best-fit Maxwellian, at varying minor radial position.

5.3 Alternative Possibilities

The observations discussed above strongly suggest that the drift wave periodically convects cold recycled ions into the central plasma. One expects that these ions desorbed from the wall as cold neutrals before re-entering the plasma and being ionized [6]. However, the ionization mean free path ℓ in Encore appears to be much longer than the 4 cm between the wall and the LIF-diagnosed volume. The mean free path is estimated from $\ell = 1/(n_t\sigma)$, where n_t is the density of targets t (electrons, ions, or other neutrals), and σ is the cross section for a particular ionization event. The cross sections for ionization by charge-exchange (ce) and by electron impact (ei) are [8]: and $\sigma_{ce} \approx 6 \times 10^{-15}$ cm^2 and $\sigma_{ei} \approx 2 \times 10^{-17}$ cm^2. For equal ion and electron densities $n_e = n_i = 10^{12}$ cm^{-3}, ionization is dominated by charge-exchange, giving $\ell \approx 1.7$ m. This length is larger than the torus dimensions, implying that neutrals pervade the vacuum chamber and raising the possibility that recycled particles are ionized *in situ*, rather than ionized at the wall before convecting inward. *In-situ* ionization, however, is completely inconsistent with the observed space dependence

of the cold particle density (c.f. Fig. 5.8). Currently this discrepancy is unresolved. It is likely that other ionization channels, e.g., photoionization or plasma sheath effects, can explain the observed high density of cold ions.

It is worthwhile also to give a brief discussion of other possible causes for the observed non-Maxwellian distributions. One such possibility arises from consideration of the Vlasov equation,

$$\left(\frac{\partial f(\mathbf{x},\mathbf{v},t)}{\partial t} + \mathbf{v}\cdot\nabla f + \frac{q}{m}(\mathbf{E}+\mathbf{v}\times\mathbf{B})\cdot\nabla_v f\right)_{orbit} = 0. \tag{5.2}$$

The Vlasov equation describes the collisionless evolution of the plasma distribution $f(\mathbf{x},\mathbf{v},t)$ in response to macroscopic electric and magnetic fields $\mathbf{E}$ and $\mathbf{B}$. The left-hand side is the convective derivative of f along a particle orbit. Since the solutions f must have total (convective) time derivative zero, one seeks solutions of the form $f = f(COM)$, where COM represents any combination of constants of the motion. For systems with time-independent Hamiltonians, for instance, the Maxwellian distribution

$$f_M(\mathbf{v}) = \exp - \left(\frac{mv_\parallel^2}{2T_\parallel} + \frac{m\mathbf{v}_\perp^2}{2T_\perp}\right)$$

is a valid solution of Eq. 5.2 because particle kinetic energy along ($\parallel$) and perpendicular to ($\perp$) the magnetic field are each conserved. For an inhomogeneous plasma, Eq. 5.2 constrains the form of the spatial part of f. For example, functions of the form $f(\mathbf{x},\mathbf{v}) \propto (1-x/L)\times f_M(\mathbf{v})$ might be proposed to model a plasma with density gradient in the $-\hat{x}$ direction. This function, though, does not satisfy Eq. 5.2 because x is not a conserved quantity; rather, for a particle executing Larmour gyration in a uniform magnetic field $\mathbf{B} = B\hat{z}$, the canonical momentum $v_y + qB\,x/m$ is conserved and leads to a distribution of the form [9]

$$f(\mathbf{x},\mathbf{v}) = \left[1 - \left(\frac{x}{L} + \frac{mv_y}{qLB}\right) + O\left(\frac{x}{L} + \frac{mv_y}{qLB}\right)^2\right] \times f_M(\mathbf{v}). \tag{5.3}$$

This distribution approximately satisfies the Vlasov equation, and the functional

velocity dependence $f(v_y) \propto \left[1 - \varepsilon_1 v_y + \varepsilon_2 v_y^2 + g(x)\right] \exp(-v_y^2)$ can produce non-Maxwellian features qualitatively similar to those observed in Fig. 5.1(a). However the Vlasov argument does not apply here, for the following reasons:

(1) The time-dependent drift wave electric field breaks geometric symmetry in the plane perpendicular to **B**. Thus there are no canonical constants of the motion in this plane, as the stochastic orbits imply.

(2) Even if an 'accidental' constant of the motion existed, it could not explain non-Maxwellian features in more than one velocity dimension: note that Eq. 5.3 gives non-Maxwellian functional dependence on only v_y. In contrast, the experimentally observed distributions were non-Maxwellian along all three velocity components, as would be expected for an injection of cold thermalized ions into a hot, separately-thermalized background population.

(3) Comparison of the LIF-measured $f(v)$ with the predictions of Vlasov theory are unjustified here because the LIF measurements diagnose a fixed spatial volume from which hot particles are lost, as described in Chapter 4, and into which new, recycled particles flow.

Another possibility, suggested by the skewed appearance of the distribution in Fig. 5.1(a), is that the strong wave electric field causes the distribution function to 'topple over.' This has been predicted for the case of ions in very strong electric fields [10]. However, the strong-**E** prediction is not directly applicable to the case of a magnetized plasma. Furthermore, if the electric field were creating such toppling, one would expect the skewed character of $f(v)$ to oscillate with the oscillatory **E** field. No such oscillation was ever observed.

5.4 Summary and Conclusions

In summary, this chapter presents direct evidence that cold ions ($T \approx 0.4$ eV) from the plasma edge are periodically convected by the drift wave back into the hot bulk plasma ($T \approx 1 - 9\,\mathrm{eV}$). The influx of recycled ions manifests itself as a cold bump on the otherwise broad background plasma velocity distribution and is easily visible

because the low local ion-ion collision rate prevents the cold and hot distributions from equilibrating. The cold bump relaxes into the background plasma distribution as the hottest background ions are lost and the distribution cools. Recycling alone does not measurably cool the background plasma because the collisional equilibration rate is very low, and stochastic heating due to the drift waves outpaces the cooling. However, the high recycled-particle density ($n_{recycled}/n_{background} \sim 1$) indicates that recycled particles compensate significantly for the drift wave orbit losses mentioned in Chapter 4. In Chapter 4 it was argued that ions in large-amplitude, low-mode-number drift waves *cannot* be well-confined, so that edge effects must be important in stochastically heated plasmas. Thus, in light of the observed cyclic nature of the ion heating, cooling, and recycling, it may be speculated that the 4-step process of heat/loss/cool/recycle is a self-consistent limit cycle for the wave-induced ion density and temperature fluctuations.

One final note, with regard to fusion: Measurements performed in argon plasmas may have limited applicability to hydrogen recycling but apply directly to the case of impurity recycling and its implications for plasma stability, as described in Section 5.1. They are also relevant to controlled impurity injection, which increasingly is being explored as a means to radiate plasma power evenly and reduce heat convection to tokamak walls [11]. Finally, these measurements demonstrate the power of the LIF technique to examine particle recycling in detail. McChesney has proposed the use of LIF to diagnose highly-ionized impurity flow in divertors [12], but this work has not yet been funded beyond the early proof-of-principle stage and has not yet been attempted in a fusion plasma [13].

Bibliography

[1] P.C. Stangeby and G.M. McCracken, "Plasma boundary phenomena in tokamaks," *Nucl. Fusion* **30**, 1271 (1990).

[2] R.J. Taylor *et al.*, "*H*-mode behavior induced by cross-field currents in a tokamak," *Phys. Rev. Lett.*, **63**, 2365 (1989).

[3] K.C. Shaing and E.C. Crume Jr., "Bifurcation theory of poloidal rotation in tokamaks: a model for the *L-H* transition," *Phys. Rev. Lett.*, **63**, 2369 (1989).

[4] A.D. Bailey III, R.A. Stern, and P.M. Bellan, Phys. Rev. Lett. **71**, 3123 (1993).

[5] G.M. McCracken and P.E. Stott, "Tokamak plasma-surface interactions," *Nuc. Fusion* **19**, 889 (1979).

[6] J.N. Brooks, "Analysis of noble gas recycling at a fusion plasma divertor," *Phys. Plasmas* **3**, 2286 (1996).

[7] B.A. Trubnikov, "Particle nteractions in a fully ionized plasma," in *Reviews of Plasma Physics* Vol. 1, edited by M.A. Leontovich (Consultants Bureau, New York, 1965).

[8] S.C. Brown, *Basic Data of Plasma Physics*, 2d ed., rev. (The M.I.T. Press, Cambridge, MA, 1967).

[9] N.A. Krall and A.W. Trivelpiece, *Principles of Plasma Physics* (San Francisco Press, San Francisco, 1986) p. 420.

[10] G.H. Wannier, *Statistical Physics*, (John Wiley and Sons, New York, 1966) p. 464.

[11] A.M. Messiaen *et al.*, "Improved confinement with edge radiative cooling at high densities and high heating power in TEXTOR," *Nucl. Fusion* **34**, 825 (1994).

[12] J.M. McChesney, "A laser-induced fluorescence diagnostic for divertors," *Bull. Am. Phys. Soc.* **40**, 1793 (195).

[13] J.M. McChesney, private communication.

Chapter 6 Ion Transport and Conditional Velocity Distributions Measured by Optical Tagging

6.1 Introduction

Optical tagging, an extension of the basic laser-induced fluorescence (LIF) technique, allows direct observation of ion transport. Tagging was first proposed by Measures [1] and by Dimock [2] *et al.*, and first demonstrated experimentally by Stern, Hill, and Rynn [3]. In the intervening years, it has been used extensively to study ion phase space trajectories. Tagging has enabled driect observations of classical diffusive transport [4], as well as anomalous transport due to Hamiltonian chaos [5], electrostatic turbulence [6], and novel long-range interactions [7].

This chapter presents results of optical tagging measurements in Encore. Two sets of tagging measurements were performed with two distinct goals. First, tagging was used to observe transport of hot ions in the very early stages of the discharge and drift wave formation. The presence of anomalously hot ions near the plasma edge at these very early times was found to be due to convection from the plasma center. Second, we attempted to test the prediction of Bailey *et al.* that ions in stochastic motion should have very exotic velocity distribution functions [8]. Tagging was used for this purpose because it was believed that an artifact of the standard LIF measurement technique could obscure sharp features of distribution functions, while tagging did not suffer from this pathology. The predicted non-Maxwellian features were never observed, and possible reasons for this are discussed.

Section 6.1 discusses the details of the tagging technique itself. Section 6.2 presents measurements of ion transport early in the Encore discharge. Section 6.3

discusses the prediction of Ref. [8] and presents associated measurements of conditional velocity distributions. Section 6.4 presents concluding thoughts.

6.2 Optical Tagging Methods

The optical tagging technique consists of illuminating the plasma with two successive laser beams, as shown in Fig. 6.1. At time $t = t_p$, a "pump" laser tuned to the resonant wavelength λ_{IE} excites transitions from I to E, depleting the population of I by an amount proportional to its absorption of λ_{IE}. The state E is not metastable and rapidly decays to many final states F, emitting fluorescence at the wavelengths λ_{EF}; the pump fluorescence is ignored. The state I repopulates due to collisions and other processes, with a characteristic refilling time τ_I. At a later time, $t = t_s$, the plasma is illuminated by a second ("search") laser, also tuned to λ_{IE}. At this point, the depletion of state I causes decreased absorptivity of the search beam and therefore decreased search fluorescence. In other words, the pump beam has 'tagged' a group of ions by changing their internal quantum states, and these tagged ions may subsequently be identified by their reduced absorptivity of a search laser. The two lasers may also be separated in space, so that reduced search fluorescence implies ion movement from pump beam location to search beam location. The tagged-state lifetime τ_i constrains the distance over which particle motion may be observed, since the pump-search delay time Δt must satisfy $\Delta t \ll \tau_I$ for the tagging effect to be appreciable.

The method described above is known as "dark tagging" because tagging by the pump laser reduces, or 'darkens,' the search fluorescence signal. In contrast, "bright tagging," uses a search laser tuned to excite a transition originating in one of the final states F. The population of F is *increased* by the pump laser action $I \rightarrow E \rightarrow F$, and therefore the corresponding search fluorescence will, in this case, be augmented.

Another key feature of the optical tagging method is that each laser interacts with only those ions with velocity $\mathbf{v}$ satisfying the Doppler condition $\mathbf{v} \cdot \hat{k} = c(1 - \lambda_L/\lambda_{IE})$, where λ_L is the probing laser wavelength, $\hat{k}$ is the direction of laser propagation, and

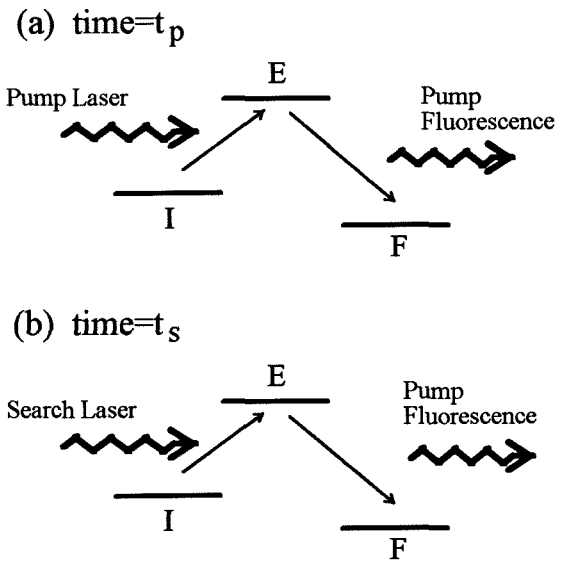

Figure 6.1: Schematic of energy levels used for optical dark tagging, showing (a) pump beam and (b) search beam interrogation and induced fluorescence.

c is light speed. (See Appendix A for details of the Doppler selection.) This means that each laser places a constraint on the velocity class of ions contributing to the tag signal. To see this more precisely, consider a pump laser pulse triggered at t_p and propagating in the x-direction, i.e., $\hat{k}_{pump} = \hat{x}$. The number n_{pumped} of absorbing ions is proportional to laser energy ρ_p and the density of ions satisfying $v_x = v_p^*$, where $v_p^* = c(1 - \lambda_{pump}/\lambda_{IE})$:

$$n_{pumped} \propto \rho_p f(\mathbf{v}, t_p)\delta(v_x - v_p^*).$$

Here the laser spectrum has been taken to be infinitely narrow, for simplicity. At time $t_s > t_p$ a search laser (wavelength λ_s) is fired in the direction $\hat{k}_s = \hat{y}$. This laser induces a fluorescence signal $\Lambda(\lambda_s)$ proportional to ρ_s and to the density of ions satisfying $v_y = v_s^*$ at time t_s. This latter density has been depleted by an amount proportional to n_{pumped}, i.e., $f(\mathbf{v}, t_s) \approx f(\mathbf{v}, t_p) - An_{pumped}\exp(-\Delta t/\tau_I)$. Thus the search fluorescence is

$$\begin{aligned}\Lambda_s(v_s) &\propto \rho_s\delta(v_y - v_s^*)f(\mathbf{v},t_s) \\ &\propto \rho_s\delta(v_y - v_s^*)f(\mathbf{v},t_p)\left[1 - A\rho_p f(\mathbf{v},t_p)\delta(v_x - v_p^*)\exp(-\Delta t/\tau_I)\right].\end{aligned}$$

Here we have assumed that the evolution of $f(v)$ over the time interval Δt is due only to the optical pumping and refilling. The exponential term accounts for this refilling, and A is a velocity-independent factor depending on the transition probabilities for the states I, E, F, etc.

Furthermore, if the pump laser trigger is chopped so that it fires on alternate search-laser shots, we can define the tag signal $\Xi(\lambda_s,\ \lambda_p, \Delta t)$ as the modulation in search fluorescence due to firing of the pump:

$$\begin{aligned}\Xi(\lambda_s, \lambda_p, \Delta t) &= [\Lambda_s(v_s^*)]_{pump\ fired} - [\Lambda_s(v_s^*)]_{pump\ did\ not\ fire} \\ &\propto -\rho_s\rho_p f(\mathbf{v},t_p)\delta(v_x - v_p^*)\delta(v_y - v_s^*)e^{-\Delta t/\tau_I}. \qquad (6.1)\end{aligned}$$

Note that performing two orthogonal velocity selections in rapid succession ($\Delta t \ll \tau_I$) allows measurement of a *conditional* velocity distribution by, for example, fixing λ_p while scanning λ_s across the Doppler spectrum. In this case,

$$\frac{\Xi(\lambda_s; \lambda_p = const)}{\rho_s\rho_p} \propto f(v_s^*; v_p^* = const). \qquad (6.2)$$

It should be emphasized that this case differs substantially from single-beam LIF measurements, which integrate $f(\mathbf{v})$ over velocity components orthogonal to $\mathbf{k}_{laser}$.

6.2.1 Lifetime Measurements

As a first test of the tagging method, a simple measurement of tagged-state lifetimes was performed. Two separate YAG-pumped dye laser beams illuminated the plasma, and the LIF viewing optics were focused on the beams' intersection volume, roughly 4

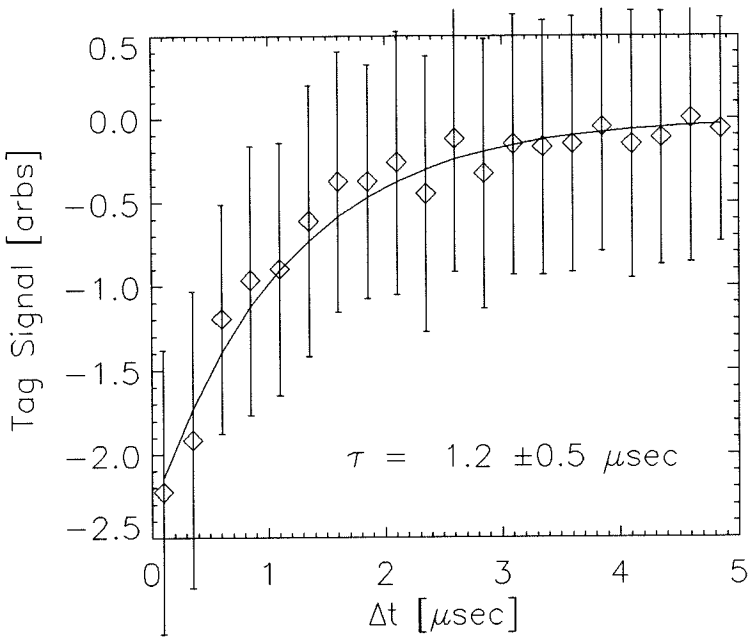

Figure 6.2: Measured tag signal as function of pump-search delay Δt. Negative-going signal corresponds to stronger (dark) tagging signal. Solid curve is exponential fit, and fitted tag-state lifetime is $\tau = 1.2$ μsec.

cm inward from the chamber wall. Both beams were tuned to the center of the Ar II resonance at 611 nm. A computer-controlled shutter reduced the pump repetition rate to 1/2 that of the search beam. The YAG Q-switches were independently triggered, allowing the pump-search delay Δt to be varied. Figure 6.2 shows a typical measured tag signal as a function of Δt. These data were obtained when the discharge density was above 2×10^{12} cm^{-3}, and the tag lifetime was found to be short, about 1 μsec.

By varying the timing of the pump and search lasers together, it was possible to determine the tagged-state lifetime as a function of time in the discharge. Using the method described above, it was found that τ_I varied from more than 5 μsec, at times very early in the discharge, to as little as 1 μsec during the bulk of the discharge. The 1-μsec lower limit was attributable to the high Encore plasma density ($> 10^{12}$ cm^{-3}), the I quantum state refilling quickly via electron–ion collisions. This short τ_I, combined with typical ion fluid velocities (2×10^3 m/s), meant that ion transport could be observed over only a few millimeters during the bulk of the discharge. In contrast,

the 5-μsec tag lifetime early in the discharge would allow transport observations over at least a centimeter. Moreover, the τ_I measurement at these very early times probably did not reflect the true tag lifetime, but rather was a measure of the transit time for tagged ions to leave the laser-pumped volume. The next section discusses transport measurements very early in the discharge.

6.3 Transport Early in the Drift Wave

Tagging was used to investigate the presence of anomalously hot ions near the chamber edge at times very early in the discharge. The existence of anomalously hot ions is indicated in Figure 6.3, which plots the LIF-measured ion temperature and Langmuir-probe-measured ion density at the position $r/a = 0.7$. These data were given in Chapter 4 and are repeated here for convenience. Note particularly the temperature and density during the first 140 μsec of the discharge (times labeled $-100 \rightarrow 40$ μsec, and hashed in the plot). As can be seen, ions as hot as $T_\perp = 2\,\mathrm{eV}$ exist at these times, when the ion density is barely detectable by the Langmuir probe; the density here is $n \leq 3 \times 10^{10}$ cm^{-3}, roughly two orders of magnitude below the mean value during the bulk of the discharge. Ion temperatures along the magnetic field were also measured at these early times, and were found to be very low, viz. $T_\parallel < 0.4$ eV. This anisotropy indicates that the ion heating mechanism is drift wave-induced stochasticity, as discussed in Chapter 4. However, the very low ion density suggests intuitively that the drift wave amplitude should be negligible at these early times. After all, the wave is comprised of collective ion motions, and at these times, very few atoms have yet ionized. Unfortunately, direct measurement of the electric field for $t < 40$ μsec was impossible because the Langmuir probe signal was too noisy to allow deduction of the plasma potential.

However, probe measurements indicated that, for $t < 40$ μsec, the density was typically much higher near the center of the machine than at the edge. For example, the density at $r/a = 0.13$ was more than 10 times higher than at $r/a = 0.7$. Thus it was possible that in the early stages of the discharge the drift wave amplitude

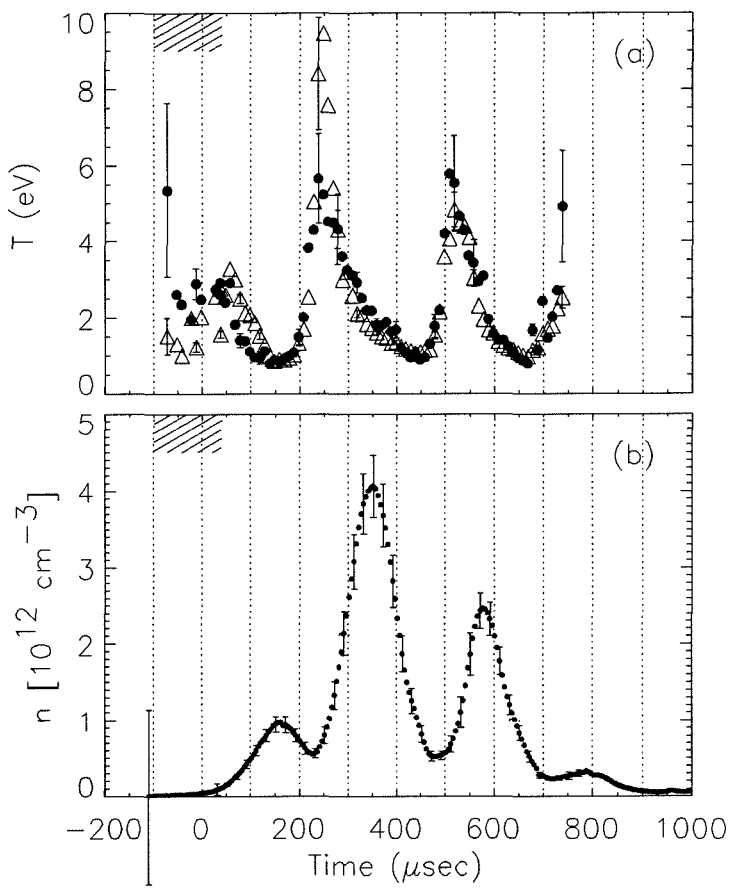

Figure 6.3: (a) LIF-measured ion temperatures perpendicular to **B**: $T_{\perp r}(\bullet)$ and $T_{\perp\theta}(\triangle)$. (b) Ion density measured by Langmuir probe. These measurements were performed at $r/a = 0.7$. The time interval discussed in the text is shown hashed.

was significant in the central plasma long before it was significant on the periphery. Therefore, the hot edge ions might be the result of stochastic heating near the plasma center followed by convection to the edge.

To verify this hypothesis, a tagging experiment was designed to detect radial transport of ions. The pump and search laser wavelengths were each held fixed at the center of the ion Doppler spectrum, and the beams were directed along chords separated vertically by 1-3 cm, as shown in Fig. 6.4. Of the two beams, the search beam was located nearer the plasma edge, so that detection of tagged ions at the search location would indicate outward radial motion. The pump-search delay Δt was scanned to monitor the arrival of tagged ions at the search location. Figure 6.5 shows examples of (dark) tagging signals for beams separated by 1.25 and 2.5 cm. The curves essentially trace the density of tagged ions at the search beam location. Figure 6.5(a) shows that the fastest tagged ions enter the search volume within 1-2 μsec, and the arrival of tagged particles peaks at about 4 μsec. Given the 1.25 cm beam separation, this time-of-flight corresponds to a mean ion velocity of $v = 2.9$ km/s, as indicated in the figure. The data in part (b) were obtained by doubling the beams' spatial separation without changing the plasma conditions. In this case the tagged ions arrive after a delay about twice as long, and the two time-of-flight measurements agree to within 10%; they are also reasonably consistent with radial fluid velocities measured by single-beam LIF.

The above transport measurements were made at $t = 40$ μsec, and similar results were found throughout the first 140 μsec of the discharge, indicating a steady flux of ions toward the chamber wall during this interval. Also, the tag and pump beam locations were exchanged and the measurements repeated to look for *inward* radial flow. No such inward flow was detected. Thus ions appear to convect preferentially outward in the early moments of the discharge.

Finally, the velocity distribution of outward-convecting ions was measured. Ions were tagged at $r/a = 0.59$ and were searched for 1.3 cm radially outward from this location. The search laser was triggered 4 μsec after the pump laser, in order to coincide with peak tagged-ion arrival at the search location (c.f. Fig. 6.5). The

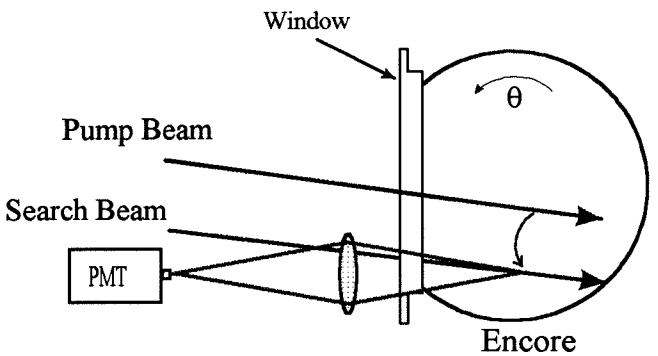

Figure 6.4: Geometry of setup to measure ion radial transport by optical tagging. A possible ion trajectory from pump beam to search beam is sketched.

search beam energy was kept low to ensure linear absorption, and its wavelength was scanned across the Doppler spectrum. The resulting measured absorption spectra are shown in Fig. 6.6. Part (a) of the figure shows the raw search fluorescence signals with the pump on and pump off. Trace (b) shows the ion profile obtained exclusively when the pump laser was off. This corresponds to the standard velocity distribution $f_{1L}(v)$ measured by 1-laser LIF. Trace (c) shows the ion profile measured when the pump laser was on. This is the distribution f_{static} of static ions, i.e., those ions which have *not* recently convected from the plasma center. Finally, trace (d) shows the difference between the pump-on and pump-off profiles. This is the distribution $f_{convect}$ of *only* those ions which have recently convected from near the plasma center. Maxwellian fits to these traces give the following temperatures (in wavelength units): $T_{convect} = 15.0$, $T_{1L} = 14.0$, $T_{static} = 13.8$. The outward- convecting ions thus account for the hottest part of the distribution, proving that the edge-ion population consists of warm particles convecting from the plasma center, together with relatively cool 'local' particles.

Two final things should be mentioned about the data in 6.6. First, although the scatter in trace (d) is significant, the temperature ordering noted above was experimentally reproducible. Second, the relatively poor Maxwellian fits in traces (b)

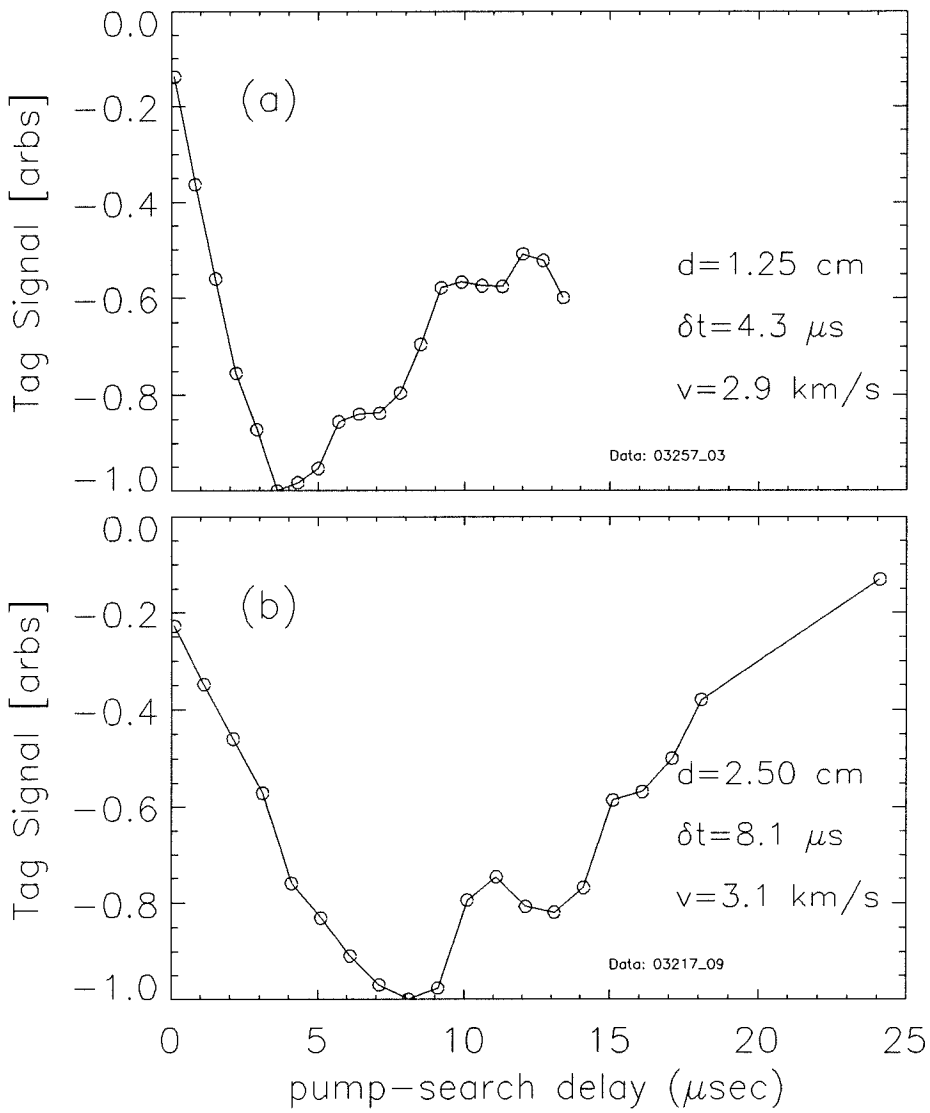

Figure 6.5: Time dependence of reduction in search beam fluorescence due to pumping, when pump beam was (a) 1.25 cm, and (b) 2.5 cm above search beam. Negative-going signal corresponds to more tagged ions. Curves have been smoothed and normalized to peak values. Annotations: d = pump-seach beam separation, δt = inferred time of flight, v = inferred transport speed.

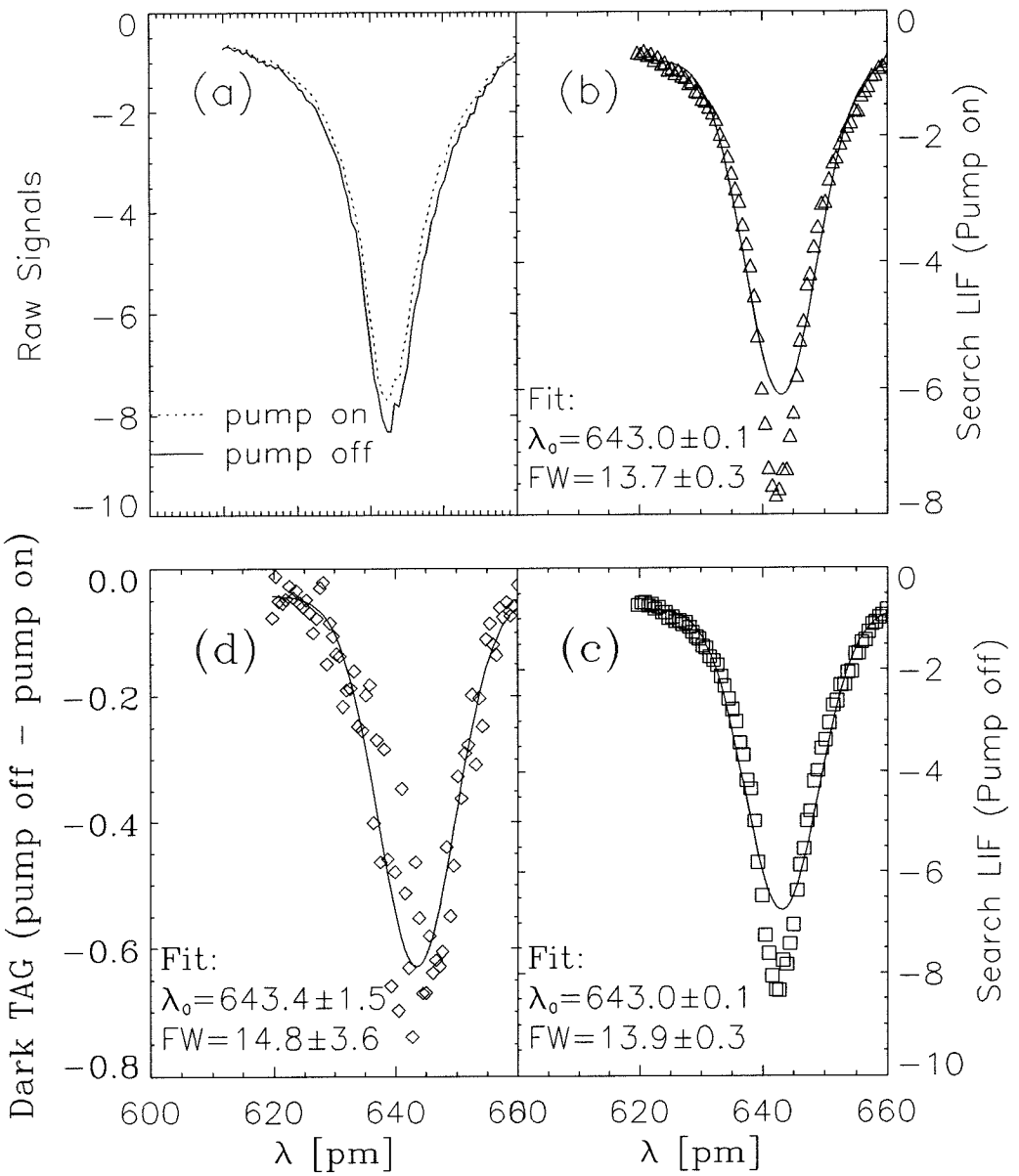

Figure 6.6: (a) Raw search laser signal with pump beam on (dashed) and off (solid). Also shown are Maxwellian fits to (b) search signal with pump on, (c) search signal with pump off, and (d) modulation in search signal due to pump laser. The last plot is the distribution of tagged ions only.

and (c) are consistent with the low ion density for times $t < 40$ μsec, not only because thermalizing collisions are infrequent, but also because the gas is still breaking down, producing a steady influx of cold, newly ionized particles.

6.4 Conditional Velocity Distributions

Bailey, Bellan, and Stern [8] have pointed out a novel interpretation of the Poincaré section plots discussed in Chapter 2. For discussion purposes, one such section is reproduced in Fig. 6.7. Recall that a Poincaré section is a representation of orbits satisfying the ion equation of motion, namely

$$m\frac{d\mathbf{v}}{dt} = q\left[\mathbf{E}(\mathbf{x},t) + \mathbf{v}\times\mathbf{B}(\mathbf{x},t)\right]. \tag{6.3}$$

Therefore, each curve in Fig. 6.7 identifies the trajectory followed by a single particle with a particular, unique initial condition. However, the trajectories are also solutions of the collisionless Vlasov equation

$$\left[\frac{\partial f(\mathbf{x},\mathbf{v},t)}{\partial t} + \mathbf{v}\cdot\frac{\partial f}{\partial \mathbf{x}} + q\left(\mathbf{E}+\mathbf{v}\times\mathbf{B}\right)\cdot\frac{\partial f}{\partial \mathbf{v}}\right]_{orbit} = 0, \tag{6.4}$$

which states simply that in the absence of collisions and particle sources and sinks, the number density f of particles along an orbit must remain constant. This means that orbits satisfying Eq. 6.3 must be curves of constant f, i.e., each distinct curve in the Poincaré section is an equipotential curve of the distribution function. Thus the Poincaré section shown in Fig. 6.7 directly displays the level curves of $f(v_x, t; v_y = 0)$. Thus, in order to reconstruct the distribution function consistent with the Encore drift-wave dynamics, one needs only to identify the *values* of these equipotential curves. Such an identification would establish a direct connection between the microscopic particle orbits and macroscopic parameters such as density, fluid velocity, and temperature, through the velocity moments of f.

The difficulty, of course, lies in determining these equipotential values. Bailey, Bellan, and Stern suggested an intuitive way to assign values to the level sets for the

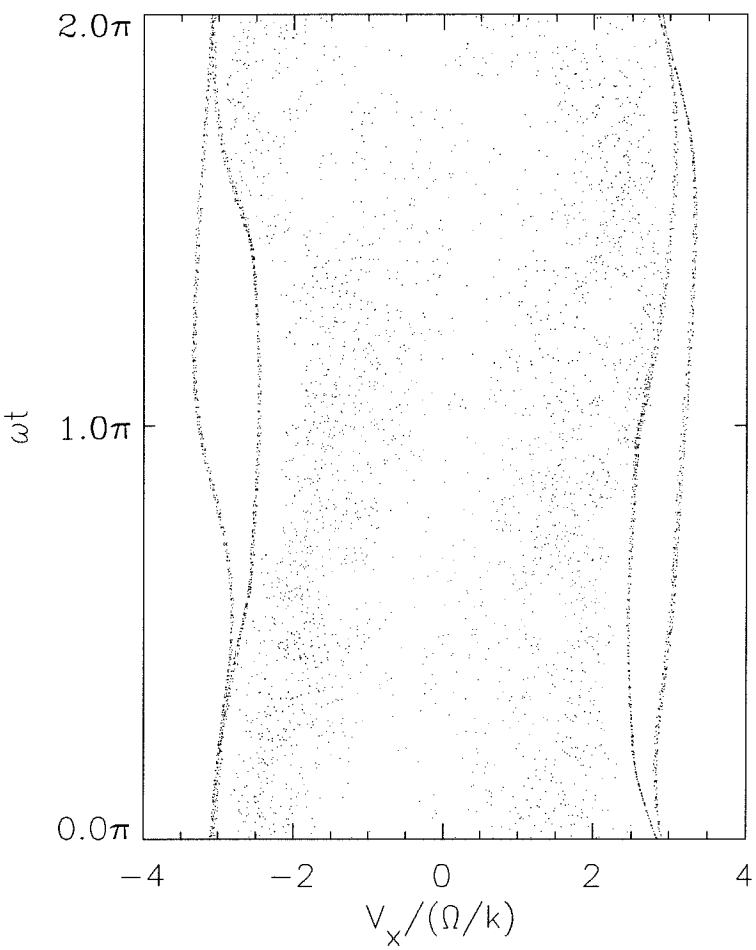

Figure 6.7: Poincaré section for ions in large-amplitude drift wave. The section shown is the plane $v_y = 0$.

case of stochastic dynamics. They noted that all the areas of the stochastic region S in Fig. 6.7 appear to be uniformly visited by orbits with initial conditions in S. Heuristically, this suggests that the distribution function is uniform over S, i.e., $f = const.$ Alternatively, one might imagine that each orbit in S carries a distinct level-value associated with its particular initial condition. In this case, f is infinitely discontinuous in S, since distinct level curves are infinitely intertwined. However, any *measurement* of f in this region must integrate over a finite phase-space volume determined by the measurement resolution. Since any such phase-space volume contains all possible level-set values, the averaging will yield an experimentally determined distribution which is constant over S. For orbits outside S, the level values of f must decrease monotonically with increasing v, because the distribution moments $\int v^m f(v)\, dv$ must be finite for all m. Furthermore, Fig. 6.7 indicates that orbits outside S are relatively unperturbed by the stochastic dynamics, reinforcing the expectation that f be classical (Maxwellian-like) in this range.

These arguments led Bailey *et al.* to predict *plateaued* velocity distributions when ion dynamics are stochastic [8]. For large-amplitude drift waves propagating normal to $\mathbf{B} = B\hat{z}$, ion dynamics are stochastic in the $v_x - v_y$ plane, suggesting a distribution of the form

$$f_{plateau}(v_x, v_y) = \begin{cases} \exp -(v_x^2 + v_y^2) & if \quad x^2 + y^2 > a^2 \\ \exp -(a^2) & if \quad x^2 + y^2 \leq a^2 \end{cases}, \tag{6.5a}$$

where a is the width of the stochastic region in velocity space. This distribution is plotted in Fig. 6.8. Distributions which, like Eq. 6.5a, are flatter than Maxwellian are know as "platykurtic." Distributions more sharply peaked than Maxwellian are termed "leptokurtic."

Plateaued distributions might be expected in Encore plasmas because ion motion in the drift waves is stochastic. However, no such platykurtic distributions have ever been observed during LIF measurements in Encore. One possible reason for this is that a one-laser LIF measurement performs velocity selection on only a single ion velocity component, integrating over velocity components orthogonal to the beam

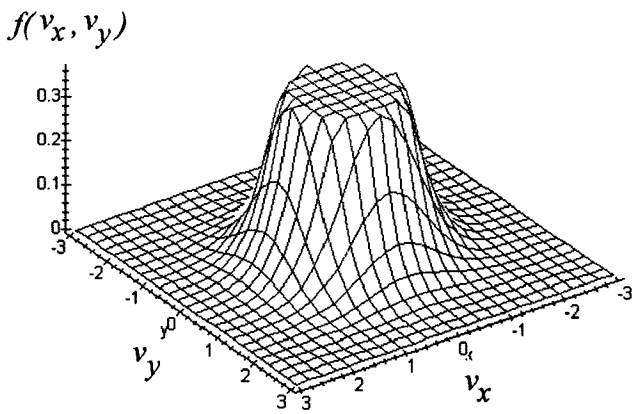

Figure 6.8: Example of plateaued velocity distribution.

(c.f. Appendix A). For laser propagation along $\hat{x}$, the LIF-measured one-dimensional velocity distribution is a marginal cut of $f(v_x, v_y)$:

$$F(v_x) = \int dv_y \, f(v_x, v_y). \tag{6.6}$$

Such integration would smooth over any sharp features in $f(\mathbf{v})$ and in particular would obscure the corners and round the flat region of $f_{plateau}$, making it difficult to distinguish from a Maxwellian profile. This can be seen by explicitly evaluating the integral in Eq. 6.6 for the distribution 6.5a. The integration is straightforward and yields

$$F_{plateau}(v_x) = N \times \begin{cases} \sqrt{\pi} e^{-v_x^2} & if \quad |v_x| > a \\ \sqrt{\pi} e^{-v_x^2} \left(1 - \operatorname{erf} \sqrt{a^2 - v_x^2}\right) + e^{-a^2} \sqrt{a^2 - v_x^2} & if \quad |v_x| \leq a \end{cases}, \tag{6.7}$$

where $N = \exp(-a^2) / [\pi (1 + a^2)]$ is a normalization constant. Figure 6.9 compares three normalized, one-dimensional velocity distributions: a marginal cut of a 2-D Maxwellian, a marginal cut of a plateau (Eq. 6.7), and a conditional cut of a 2D plateau. Comparison of curves (b) and (c) shows that the marginal integration indeed

smooths the plateau.

As described in Section 6.2, optical tagging is capable of measuring directly the conditional velocity function $f_{plateau}(v_x; v_y = 0)$. This would prevent the smoothing artifacts inherent in 1-laser LIF, and moreover the conditional distribution so measured could then be compared directly to the level curves shown in Fig. 6.7. We used optical tagging to search for platykurtic distribution functions in stochastically heated Encore plasmas. Two orthogonal dye-laser beams were directed across the plasma at right angles to each other, as shown in Fig. 6.10 The plasma volume diagnosed was at the intersection of the two beams and the viewing optics field, and located near the plasma edge, where the drift wave amplitude was maximum. The pump laser was optimized for narrow-band lasing in order to tag only those ions with $v_r = 0$. With the pump wavelength held constant, the search wavelength was scanned to determine the v_θ-dependence of the tagged ion distribution, i.e., $f(v_\theta; v_r = 0)$. A sample data set is displayed in Fig. 6.11. The conditional distribution, curve (d) is evidently very narrow and *more sharply peaked* than its best-fit Maxwellian. The data in Fig. 6.11 were representative of most measured conditional distributions in Encore. No platykurtic distributions were ever found by optical tagging. Rather, the observed distributions always were well-fit by Maxwellians or were leptokurtic[1]. The use of the tagging method rules out the possibility that the measured $f(\mathbf{v})$ was artificially smoothed or deformed by the LIF technique.

One explanation for our failure to find the platykurtic distributions predicted by Ref. [8] may be that Encore ions were much more collisional than was previously believed. This discovery was discussed in Chapter 4, where the measured collision rate was shown to rise periodically to values far above the drift wave frequency. Recall that the flattening argument was based on collisionless Vlasov theory and therefore cannot be applied to a highly collisional plasma. To investigate the possible effect of collisions on the conditional distributions, tagging measurements were performed very early in the Encore discharge, while the density was only 1% of that during the

[1]Leptokurtic distributions were consistent with cold ion recycling (c.f. Chapter 5) or with a flux of newly-ionized particles during the discharge initiation (c.f. Section 6.3).

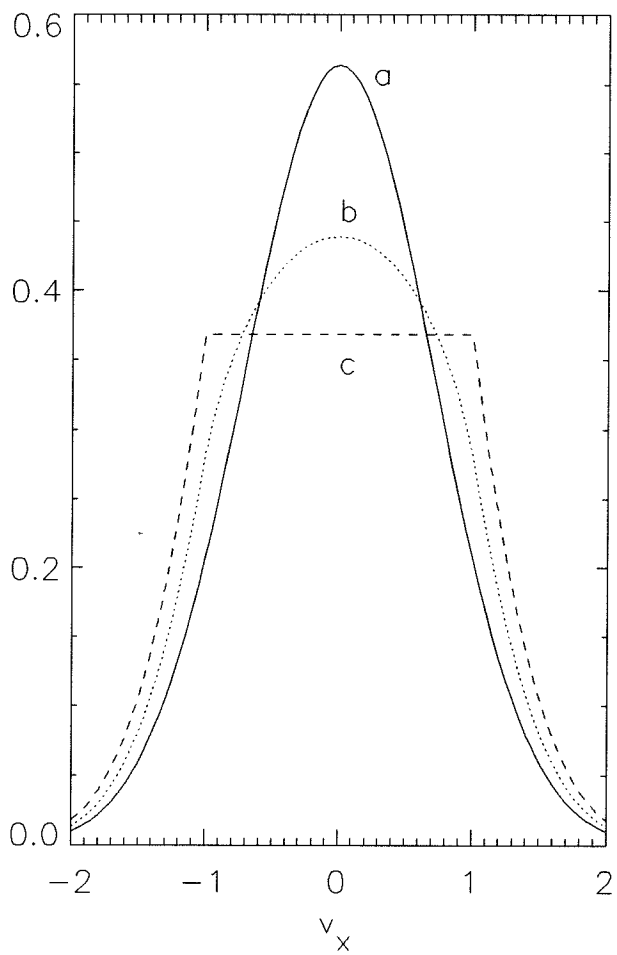

Figure 6.9: 1-dimensional velocity distributions corresponding to (a) marginal cut of 2D Maxwellian, (b) marginal cut of 2D plateau, and (c) conditional cut of 2D-Plateau, through $v_y = 0$. All are normalized to unit area.

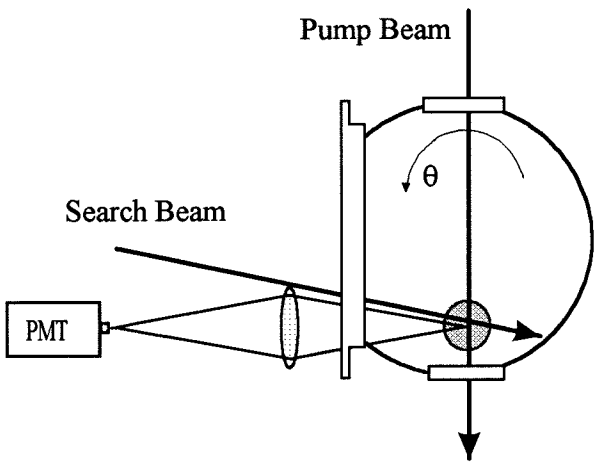

Figure 6.10: Geometry of setup for conditional tagging measurement. The diagnosed plasma volume is shaded.

discharge bulk. At these times, however, the plasma breakdown was just initiating, and the influx of newly-ionized cold particles made $f(\mathbf{v})$ strongly leptokurtic. Thus, while no flattened distributions were ever discovered in Encore, the possibility of their existence in a truly collisionless stochastically heated plasma cannot be entirely ruled out.

6.5 Conclusion

Optical tagging was used to follow ion motion early in the discharge, when the plasma density was very low. Tagging enabled direct observation of ion motion over radial distances of up to 3 cm. It was shown that relatively hot ions convect from the plasma center to the plasma edge and that this explains the anomalously hot, non-Maxwellian distributions seen at the edge in this early stage of the discharge. These measurements also demonstrate the utility of the tagging technique at these early times. Since the ion temperature at these times is high ($\gtrsim$ 2 ev), the stochastic heating mechanism is evidently active. These times, therefore, offer both the low plasma density conducive to the tagging method (i.e., a long tag lifetime) and the

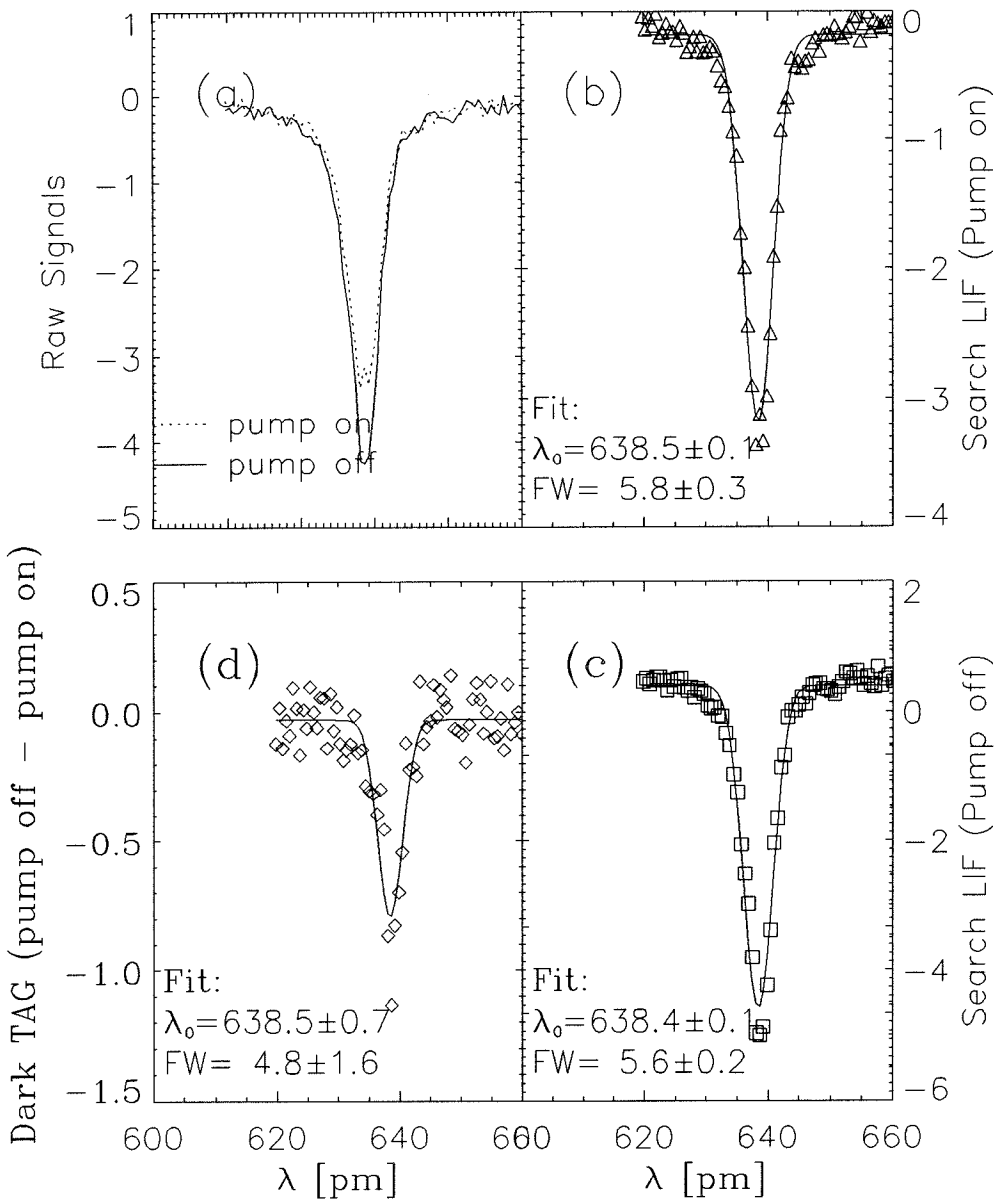

Figure 6.11: Conditional velocity distribution measured by optical tagging. (a) Raw search flourescence signals with pump on and off. Maxwellian fits are shown for (b) pump-on signal, (c) pump-off signal, and (d) difference signal. The last is the true conditional velocity distribution $f(v_\theta; v_r = 0)$.

fascinating subject of dynamical stochasticity to which to apply the method. One promising possibility is to use a narrowly focused pump laser and a *planar* search laser, and to image the poloidal cross section using a planar detector array. This would offer, for example, the first direct observation of ion diffusion in two spatial dimensions.

Tagging was also used to measure conditional cuts of ion two-dimensional velocity distributions, as distinct from marginal cuts of the distributions. This was thought necessary to avoid measurement artifacts (resulting from the marginal integration) which would obscure sharp non-Maxwellian features in the distribution. The plateaued distribution functions predicted by Bailey *et al.* for ions in stochastic motion were never observed.

Bibliography

[1] R.M. Measures, J. Appl. Phys., **39**, 5232 (1986).

[2] D. Dimock, E. Hinnov, and L.C. Johnson, Phys. Fluids **12**, 1730 (1969).

[3] R.A. Stern, D.N. Hill, and N. Rynn, "Direct ion-transport measurement by optical tagging," *Phys. Lett. A* **93**, 127 (1983).

[4] J. Bowles, R. McWilliams, and N. Rynn, "Direct measurement of velocity-space transport in a fully ionized plasma," *Phys. Rev. Lett. 68*, 1144 (1992); A. Fasoli *et al,*. "Cross-field diffusion quenching by neutral gas injection in a magnetized plasma," *Phys. Rev. Lett.* **68**, 2925 (1992).

[5] F. Skiff *et al.*, "Conservation laws and transport in Hamiltonian chaos," *Phys. Rev. Lett.* **61**, 2034 (1988); A. Fasoli *et al.*, "Dynamical chaos of plasma ions in electrostatic waves," *Phys. Rev. Lett.* **70**, 303 (1993).

[6] R. McWilliams, M.K. Okubo, and N.S. Wolf, "The transport of ions in a turbulent plasma," *Phys. Fluids B* **2**, 523 (1990).

[7] F. Anderegg *et al.,* "Test particle transport due to long range interactions," *Phys. Rev. Lett.*, **78**, 2128 (1997).

[8] A.D. Bailey III, P.M. Bellan, and R.A. Stern, "Poincaré maps define topography of Vlasov distribution functions consistent with stochastic dynamics," *Phys. Plasmas* **2**, 1 (1995).

Chapter 7 Conclusion

Experimental physics is a continuous pursuit towards understanding the fundamental natural phenomena of our world. It is an iterative pursuit, with each successive experiment building upon the existing body of knowledge to probe increasingly complex physics. The study of stochastic phenomena in plasmas has certainly proceeded along these lines. The first measurements of stochastic electron heating used electrostatic energy analyzers and could not resolve the time-dependent details of the heated particle distribution functions [1]. Later experiments employed more powerful laser-induced fluorescence (LIF) methods [2] to obtain the distribution functions of stochastically heated ions [3], and to probe stochastic dynamics in more detail, directly observing the breakdown of Hamiltonian conservation laws with the onset of chaos [4], and demonstrating the exponential spreading of stochastic orbits in phase space [5]. These experiments were conducted in linear plasmas with stochasticity being the only important heat transport mechanism. The experiments of McChesney *et al.* [6] extended the LIF method to majority ions in toroidal plasmas and observed stochastic heating in that important geometry. The work of Bailey gave insight into the regions of validity of standard plasma fluid theory when ion dynamics are stochastic [7]. The last two experiments also concerned only one dominant heat transport mechanism, and did not examine heating in multiple velocity dimensions.

The measurements presented in this thesis build on the works mentioned above by extending LIF methods to three velocity dimensions, providing a more complete picture of ion dynamical processes associated with stochastic heating; in particular, new observations reveal that collisions and non-local effects, such as orbit loss and recycling, play essential roles. Ions are rapidly and stochastically heated in the plane normal to $\mathbf{B}$, and collisions redistribute the 'stochastic energy' among the three degrees of ion freedom. The anisotropic ion temperature relaxes in accordance with Fokker-Planck theory, with a highly time-dependent collision rate due to the fluctu-

ating plasma density and temperature. Stochastically heated ions are then lost from the plasma when their orbit radii become comparable to the machine dimensions. Such orbit loss results in bulk cooling and density loss. Finally, recycled ions convect inward from the plasma edge and repopulate the depleted plasma.

There can be little doubt that future applications of the LIF method will shed still further light on these rich plasma dynamical phenomena.

Bibliography

[1] F. Doveil, "Stochastic plasma heating by a large-amplitude standing wave," *Phys. Rev. Lett.* **46**, 532 (1981).

[2] R.A. Stern and J.A. Johnson III, "Plasma ion diagnostics using resonant fluorescence," *Phys. Rev. Lett.* **34**, 1548, (1975).

[3] F. Skiff, F. Anderegg, and M.Q. Tran, "Stochastic particle acceleration in an electrostatic wave," *Phys. Rev. Lett.* **58**, 1430 (1987).

[4] F. Skiff et al., "Conservation laws and transport in Hamiltonian chaos," *Phys. Rev. Lett.* **61**, 2034 (1988).

[5] A. Fasoli *et al.*, "Dynamical chaos of plasma ions in electrostatic waves," *Phys. Rev. Lett.* **70**, 303 (1993).

[6] J.M. McChesney, P.M. Bellan and R.A. Stern, "Observations of fast stochastic ion heating by drift waves," *Phys. Rev. Lett.* **59,** 1436 (1987).

[7] A.D. Bailey III, R.A. Stern, and P.M. Bellan, "Measurement of coherent drift-wave ion-fluid velocity field when ion dynamics are stochastic," *Phys. Rev. Lett.* **71**, 3123 (1993).

Appendix A Line-Broadening Mechanisms

A.1 Doppler Broadening

If the ion absorption line is primarily Doppler broadened, then the ion velocity distribution $f(\mathbf{v},t)$ can obtained as follows. For a single ion with resonant frequency ν_{IE}, the (semiclassical) probability per unit time of absorbing radiation in the frequency range $(\nu',\ \nu'+d\nu')$ is [1]

$$dP\,(\nu;\nu_{IE}) = \frac{A_{IE}c^3\rho(\nu)g(\nu;\nu_{IE})}{8\pi h\nu^3}\,d\nu, \tag{A.1}$$

where A_{IE} is the Einstein A coefficient for the transition $I \rightarrow E$, $\rho(\nu)$ is the spectral energy density ($\mathrm{J{\cdot}m^{-3}{\cdot}s}$) of the radiation field, and $g(\nu,\nu_{IE})$ is the natural lineshape of the transition,

$$g(\nu;\nu_{IE}) = \frac{A_{IE}}{\pi[(\nu-\nu_{IE})^2+A_{IE}^2]}.$$

For an ion moving with velocity $\mathbf{v}$, the resonant frequency in the laboratory frame is related to that in the ion rest frame by the Doppler shift formula

$$\nu_{IE}^{lab\ frame} \approx \nu_{IE}^{ion\ frame}\,(1+\mathbf{v}\cdot\hat{k}/c) \equiv \nu_{IE}^{*}.$$

The Doppler-induced spread in ion velocities is then roughly $\Delta\nu_D \approx (v_{th}/c)\nu_{IE}$, where v_{th} is the ion thermal speed. Accounting for these Doppler shifts, the absorption rate for an ensemble of ions with distribution $f(\mathbf{v},t)$ is

$$\dot{N}_{IE}(\nu_L) = \frac{A_{IE}c^3}{8\pi h}\int_{-\infty}^{\infty} d^3\mathbf{v}\int_{-\infty}^{\infty} d\nu\ f(\mathbf{v},t)\nu^{-3}\rho(\nu)g(\nu;\nu_{IE}^{*}). \tag{A.2}$$

This unwieldy expression may be simplified by noting first that the natural lineshape is very narrow compared to the Doppler width, i.e., $A_{IE} \ll \Delta\nu_D$. For example, $A_{IE} \sim 20$ MHz for typical Ar II transitions used in this work (c.f. Table 2.1), whereas the Doppler spread of Ar ions at room temperature is 845 MHz. Thus $g(v, v^*_{IE})$ can be approximated as $g(\nu, \nu^*_{IE}) = \delta[\nu - \nu_{IE}(1 + v_\parallel/c)]$, where $v_\parallel = \mathbf{v} \cdot \hat{k}$ and $\delta[\ ]$ is the Dirac delta function. Using this approximation the integral over $v_\parallel$ yields

$$\dot{N}_{IE}(\nu_L) = \frac{A_{IE}c^4}{8\pi h\nu_{IE}} \int_{-\infty}^{\infty} d\nu\, \nu^{-3}\rho(\nu) \int_{-\infty}^{\infty} d^2\mathbf{v}_\perp f\left[\mathbf{v}_\perp, c\left(\frac{\nu - \nu_{IE}}{\nu_{IE}}\right)\right]. \tag{A.3}$$

Treating the narrow laser linewidth as $\rho(\nu) = \rho(\nu)\delta(\nu - \nu_L)$, where ν_L is the laser center frequency, simplifies the intergal over ν, leaving

$$\dot{N}_{IE}(\nu_L) = \frac{A_{IE}c^4}{8\pi h\nu_{IE}\nu_L^3}\rho(\nu_L) \int_{-\infty}^{\infty} d^2\mathbf{v}_\perp f\left[\mathbf{v}_\perp, c\left(\frac{\nu_{IE} - \nu_L}{\nu_L}\right)\right]. \tag{A.4}$$

Note that this integral is a *marginal* cut of the distribution, i.e., the laser performs no velocity selection in the directions perpendicular to **k**. Equation (A.4) is easily evaluated for a *separable* distribution of ion velocities, $f(\mathbf{v}_\perp, v_\parallel) = f_\perp(\mathbf{v}_\perp) f_\parallel(v_\parallel)$, giving

$$\dot{N}_{IE}(\nu_L) = \frac{A_{IE}c^4}{8\pi h\nu_{IE}\nu_L^3}\rho(\nu_L)\, f_\parallel\left[v_\parallel = c\left(\frac{\nu_{IE} - \nu_L}{\nu_L}\right)\right]. \tag{A.5}$$

The fluorescence signal $\Lambda(\lambda_L)$ (induced fluorescence photons/input laser photon) is then seen to be[1]

$$\Lambda(\nu_L) \propto \frac{A_{EF}\dot{N}_{IE}(\nu_L)}{\nu_{IE}^3\rho(\nu_L)} \propto f_\parallel\left[v_\parallel = c\left(\frac{\nu_{IE} - \nu_L}{\nu_L}\right)\right].$$

For a Maxwellian velocity distribution $f(v_\parallel) = (\pi v_{th}^2)^{-3/2} \exp[-(v_\parallel - u_\parallel)/v_{th}]^2$, the LIF spectrum is a Gaussian. In wavelength units, we have finally

[1]Here we are making the approximation that $\nu_c^{-3} \approx \nu_{IE}^{-3}$. This is accurate to 1 part in 10^4 for a typical laser scan range of 50 pm.

$$\Lambda(\lambda_L) \propto \exp - \left[\frac{c}{v_{th\|}\lambda_{IE}} (\lambda_L - \lambda_{IE}) - \frac{u_\|}{v_{th\|}} \right]^2, \tag{A.6}$$

where $v_{th\|}$, $u_\|$ are the ion thermal and fluid velocity components along $\mathbf{k}$. The ion temperature and fluid velocity are then readily obtained from the width $\Delta\lambda$ (FWHM) and peak wavelength, λ_{peak}, of the measured LIF spectrum:

$$\begin{aligned} u_\| &= c(\lambda_{peak}/\lambda_{IE} - 1) \\ T_i \text{ [eV]} &= 1.7 \times 10^8 \mu (\Delta\lambda/\lambda_{IE})^2, \end{aligned} \tag{A.7}$$

where μ is the ion mass in amu.

Scanning λ_L across the resonance at λ_{IE} measures one component of the velocity distribution. Multiple beams can be used to probe multiple components simultaneously, and these marginal cuts can be used to reconstruct the entire distribution tomographically, if desired [2].

A.2 Power Broadening

The approximation that the laser line width $\Delta\lambda_L$ is infintesimally small (compared to the ion Doppler width $\Delta\lambda_D$) is not always valid; specifically, when the power in the wings of the laser spectrum is sufficient to saturate the transition $I \longrightarrow E$, the measured absorption spectrum is artificially "broadened."

To see this, consider a situation in which the laser center wavelength λ_L is detuned from the absorption peak λ_{peak}, so that the two distributions overlap only in the wings. This situation is represented in Fig. A.1. If the laser power in the spectral range $\delta\lambda$ is sufficient to saturate the ion absorption in that region, even when the laser is so detuned, then tuning the laser closer to λ_0, the center of $\delta\lambda$, does not result in more transitions from $\delta\lambda$. Thus, the absorption measured by scanning λ_L across the resonance is relatively strong even when $\lambda_L \ll \lambda_{peak}$ and $\lambda_L \gg \lambda_{peak}$: the inferred spectrum is anomolously broad.

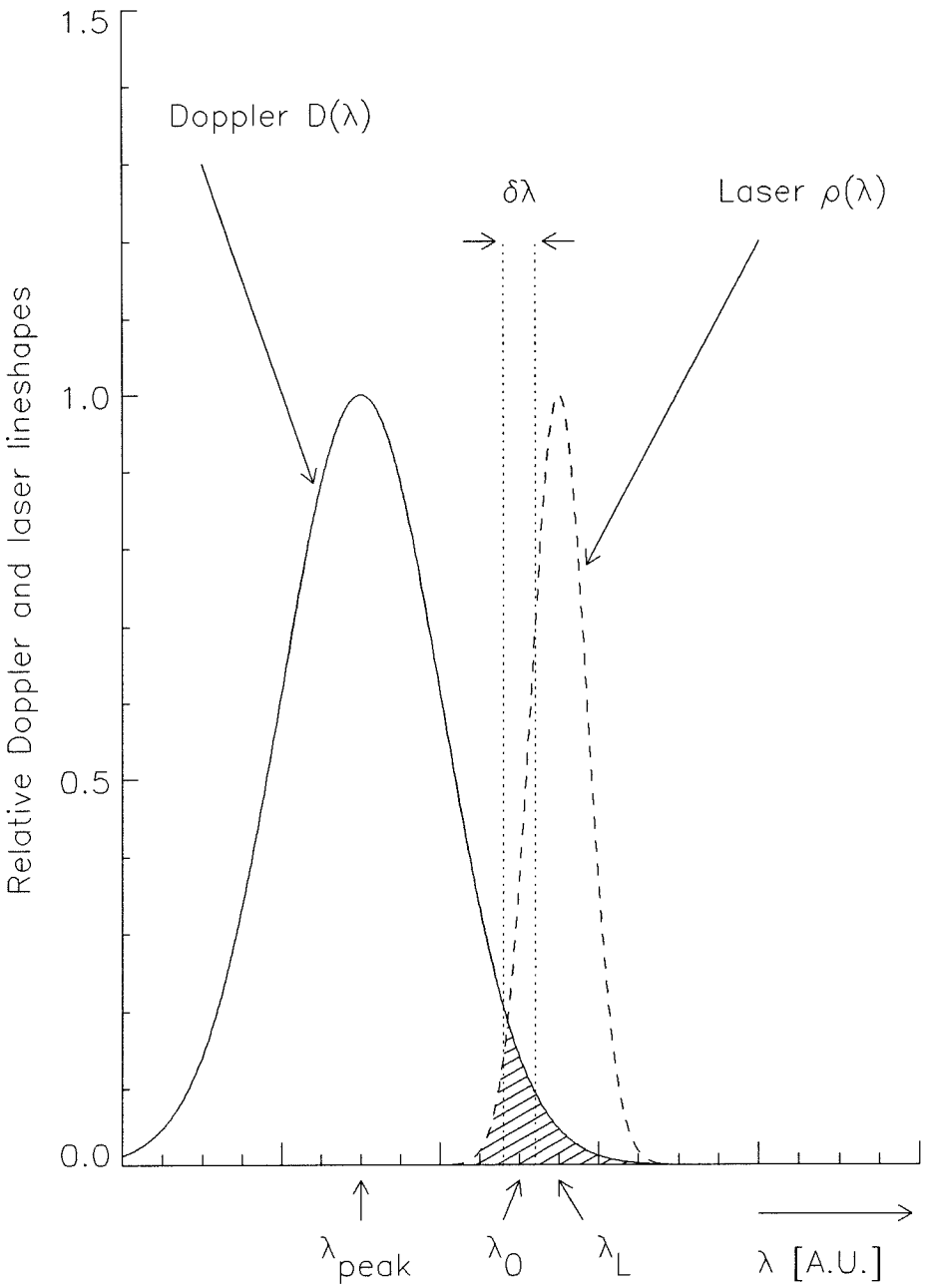

Figure A.1: Sketch of Doppler-broadened ion absorption lineshape (solid) and laser spectral intensity (dashed). These are centered on λ_{peak} and λ_L, respectively. The region of overlap is hashed.

Goeckner and Goree have studied power-broadening in the context of LIF in ArII plasmas [3], [4]. They found that for the transition $3d^2G_{9/2} \rightarrow 4p^2F_{7/2}$, power broadening is significant at laser spectral intensities $\rho \geq 8.3 \times 10^{-11}$ Joule·s·m^{-3}. Their plasma conditions were $T_i = 0.028$ eV and $n = 10^{15}$ m^{-3}. In Encore plasmas, the power broadening threshold was experimentally determined to be $\rho_{threshold} \approx 10^{-11}$ Joule·s·m^{-3}. This threshold was measured by iteratively increasing ρ until the measured T_i began to increase. The discrepancy between the threshold reported here and that of Goeckner and Goree may be due to the very different plasma conditions considered. Our experimentally determined $\rho_{threshold}$ agreed with results of numerical modeling of the 3-level system ($3d^2G_{9/2}$, $4p^2F_{7/2}$, $4s^2D_{5/2}$) under Encore conditions [5]. The experimental data and modeling results are shown together in Fig. (A.2), which plots the dependence of the peak LIF signal on the probing laser pulse energy. The 'knee' at which the LIF signal begins to saturate is clearly visible.

A.3 Zeeman Broadening

The Encore toroidal magnetic field induces a small Zeeman splitting in the energy levels used for LIF work. These splittings manifest as line broadening, since the wavelength shift between the lines is small compared to the probing laser bandwidth. The magnitude of the Zeeman-induced splitting is given by

$$(\Delta\lambda)_Z \approx 10^{-9}\lambda^2 B, \tag{A.8}$$

where λ is expressed in Angstroms and B in kilogauss. For $B = 300$ Gauss, the $3d^2G_{9/2} \rightarrow 4p^2F_{7/2}$ transition acquires a Zeeman breadth of about 1 picometer. This breadth is narrower than the laser resolution and was negligible compared to the typical measured Doppler widths of 6-20 pm. Therefore, no effort was made to deconvolve Zeeman broadening from the measured distributions.

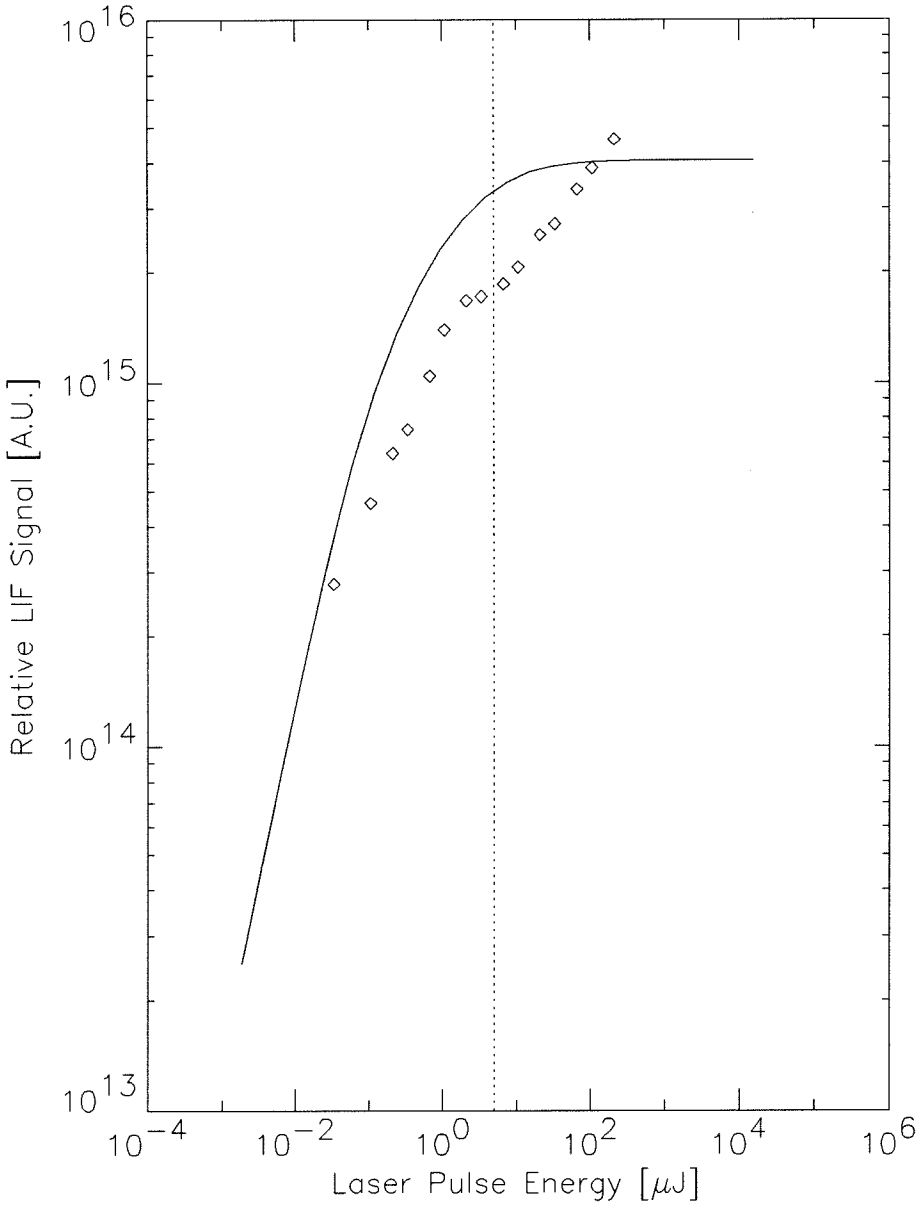

Figure A.2: Peak relative LIF signal for the transtion $3d^2G_{9/2} \rightarrow 4p^2F_{7/2}$. The discrete points are experimental data, and the solid line is the result of a simulation. The dashed line corresponds to a spectral energy density $\rho = 1.5 \times 10^{-11}$ J·s·m^{-3}.

Bibliography

[1] A. Yariv, *Optical Electronics* (CBS College Publishing, New York, 1985).

[2] R. Koslover and R. McWilliams, "Measurement of multidimensional ion velocity distribution by optical tomography," *Rev. Sci. Instrum.*, **57**, 2441 (1986).

[3] M.J. Goeckner and J. Goree, "Laser-induced fluorescence measurement of plasma ion temperatures: Corrections for power saturation," *J. Vac. Sci. Technol. A* **7**, 977 (1989).

[4] M.J. Goeckner, J. Goree, and T.E. Sheridan, "Saturation broadening of laser-induced fluorescence from plasma ions," *Rev. Sci. Instrum.*, **64**, 996 (1993).

[5] J.M. McChesney, "A laser-induced fluorescence diagnostic for divertors," Final Report, DOE Grant No. DE-FG03-92ER54150.